The Pennsylvania State University

The Graduate School

ESTIMATION AND REDUCTION OF TEMPORAL MAGNETIC FIELD FLUCTUATIONS IN POWERED MAGNETS USING INDUCTIVE AND NMR FEEDBACK CONTROL

A Dissertation in

Electrical Engineering

by

Brian F. Thomson

Submitted in Partial Fulfillment

of the Requirements

for the Degree of

Doctor of Philosophy

December 2013

The dissertation of Brian F. Thomson was reviewed and approved* by the following:

Jeffrey L. Schiano

Associate Professor of Electrical Engineering

Dissertation Adviser, Chair of Committee

Constantino M. Lagoa

Professor of Electrical Engineering

W. Kennneth Jenkins

Professor of Electrical Engineering

Patrick M. Lenahan

Distinguished Professor of Engineering Science and Mechanics

Kultegin Aydin

Professor of Electrical Engineering

Department Head of Electrical Engineering

*Signatures are on file in the Graduate School.

Abstract

Powered magnets provide high magnetic fields that promise to significantly improve nuclear magnetic resonance spectroscopy (NMR). Higher fields increase NMR chemical shift resolution and signal-to-noise ratio (SNR) while decreasing quadrupolar line broadening in solids. High resolution NMR is typically performed using superconducting magnets, which are currently limited to 24 Tesla. Powered magnets can provide continuous fields up to 45 Tesla, significantly larger than that achievable by superconducting magnets. This will dramatically expand opportunities in the areas of material science, chemistry, and biology. However, temporal magnetic field fluctuations due to both the power supply and cooling water system currently render these magnets unsuitable for high resolution NMR.

The focus of this dissertation is to design, synthesize, and verify a feedback control system that reduces temporal field fluctuations so that powered magnets can be used for high resolution NMR. Earlier studies have shown that feedback control using inductive measurements significantly reduces higher frequency field fluctuations associated with power supply ripple, but are limited in their ability to reduce lower frequency field fluctuations associated with variations in the cooling water system. Conversely, feedback control using NMR measurements are more conducive to reducing lower frequency field fluctuations and less successful at higher frequencies. Feedback control systems which use NMR measurements are often referred to as field-frequency locks (FFLs). Earlier studies have shown that FFLs can estimate and reduce lower frequency field

fluctuations in superconducting magnets, but have limited ability to do the same in powered magnets. This dissertation investigates why such FFLs are limited in powered magnets, and demonstrates some alternative methods for estimating lower frequency field fluctuations using NMR measurements in powered magnets. A digital sampled-data feedback control design using field fluctuation estimates from NMR measurements is combined with feedback control using inductive measurements, forming a cascade feedback control design that reduces both lower and higher frequency field fluctuations. This approach is experimentally verified in a powered magnet operating at 25 Tesla.

Table of Contents

List of Figures

List of Tables

Acknowledgments

There are so many to thank in the process of obtaining a Ph.D. degree. First, I would like to thank my adviser Dr. Jeffrey Schiano, who gave me the opportunity to pursue my dream of a Ph.D. degree. I have learned so much under his guidance and I appreciate the long hours he spent helping me achieve this degree. I would like to thank Dr. William Brey at the National High Magnetic Field Lab for his supervision on this project which was crucial to keeping us focused on our goals. Kiran Shetty was also instrumental in this research project, as he spent many long hours and late nights helping us develop our system experimentally. I am forever indebted to him for this help. I would like to thank Ben McPheron for his assistance in this research work. His dedication to the project was extremely useful in developing this research work to meet our goals. My additional committee members, Dr. Contantino Lagoa, Dr. Kenneth Jenkins, and Dr. Patrick Lenahan were very valuable in providing feedback on this research project. I appreciate their effort and time spent reviewing this research work.

I would also like to thank my friends and family who have supported me throughout this process. My friends always showed that they cared about me, and I am very lucky to have such great friendships in my life. My family was incredibly supportive throughout this process. They always believed in me even in difficult times. My sisters Deborah and Jennifer are so special to me. They always supported me no matter the circumstances. They often told me they are proud of me not just as a student, but as a person. This is one of the greatest compliments I could receive. My brother Daniel was extremely supportive in this process. He often gave me confidence by encouraging me, believing that I could achieve this dream of mine. I truly love my

sisters and brother and cannot say in words how much I appreciate their support. My girlfriend Leila, who lived out this experience vicariously through me. They always say that behind any great accomplishment of a man there is a great women. Well that couldn't be more true in this case. We spent so much time discussing my pursuit of this degree, and she was always willing to listen and give advice. I love her so much for that support.

Lastly, I would like to parents Francis and Roberta to whom I owe my life. Their support throughout my entire college experience was unquestioned. They always told me I could achieve my goals, and it seems they were always available to me when I needed them most. My father, who attended my Ph.D. defense, told me many times that he was proud of me. He was was always optimistic about my endeavors and supported my decisions. My mother, who was a teacher for more than 30 years, always gave me great advice. She made time to talk to me, and shared her wisdom with me on countless occasions. Someday I hope to be half as good a teacher as her. There are no other parents I would rather have, and I am so thankful to have them in my life.

Chapter 1

Temporal Field Fluctuations in Powered Magnets

Magnetic field strength is considered high if it challenges the strength and current carrying capacity of the materials comprising the magnet [1]. Powered magnets provide high magnetic fields that promise to significantly improve nuclear magnetic resonance spectroscopy (NMR). This will dramatically expand opportunities in the areas of material science, chemistry, and biology. However, temporal magnetic field fluctuations due to both the power supply and cooling water system currently render these magnets unsuitable for high resolution NMR [2]. The focus of this dissertation is to design, synthesize, and verify a feedback control system that reduces temporal field fluctuations so that powered magnets can be used for high resolution NMR.

1.1 High Field Powered Magnets

The physical phenomenon known as nuclear magnetic resonance (NMR) was first described by Bloch [3] and Purcell [4] in 1946. Since then NMR spectroscopy has become a very important tool in studying the areas of materials science, chemistry, and biology. It provides information

about structure of atoms or molecules in a sample and is the basis for magnetic resonance imaging (MRI).

In NMR spectroscopy, a large magnetic field B_0 polarizes the magnetic moments of the nuclei within the atoms or molecules. Increasing B_0 greatly improves several aspects of NMR spectroscopy. The signal-to-noise ratio (SNR) has been estimated to increase as $B_0^{7/4}$ for nuclei with spin 1/2 where skin loss is dominated by the receiver coil [6]. Increasing magnetic field strength from 24 to 36 Tesla (T) will approximately double SNR under these conditions.

In addition to improving SNR, it is well known that higher field strengths improve NMR chemical shift resolution. This resolution increases linearly with B_0 for hydrogen nuclei [5], and improves roughly as B_0^N for N-dimensional NMR experiments [1]. When considering quadrupolar nuclei in solids, higher field strengths reduce line broadening which improves chemical shift resolution. This was demonstrated for fields up to 40 T where the resolution improved as B_0^2 for a specific sample containing quadrupolar nuclei [7]. Reducing quadrupolar line broadening allows for new opportunities to study scientifically and commercially important ceramics with metals comprised of quadrupolar nuclei. Furthermore, high field increases the effect of intermolecular multiple-quantum coherences (iMQCs), which can be used for improving NMR chemical shift resolution [9, 10] and MRI image contrast [11]. These improvements justify the current effort to achieve larger B_0 field strengths.

Typical NMR experiments use a superconducting magnet to generate B_0 because these magnets produce nearly constant fields over a long period of time. When these magnets are commissioned, an external power supply generates current through the superconducting coil. Once the field has reached its desired value, a superconducting shunt is placed across the coil and the power supply is removed. As long as the magnetic coils are cooled, the coil current, and hence magnetic field remain nearly constant. As a result, these magnets have produced favorable field conditions for NMR spectroscopy to this point.

While superconducting magnets produce a nearly constant magnetic field, the physical prop-

erties of the superconducting coil limit their maximum field strength B_0 to 24 Tesla [12, 13, 14]. In order to further improve NMR spectroscopy, larger field strengths may be employed. As an alternative to superconducting magnets, powered magnets use an external power supply to continuously source power to the coil. Powered magnets like resistive and hybrid (resistive and superconducting) magnets have demonstrated fields significantly larger than superconducting magnets up to 45 T [15].

Resistive magnets are comprised of normal-metal coils and are capable of achieving fields greater than 25 Tesla at the expense of significant power loss in the coil. Another technique for achieving high fields with reduced power costs are hybrid magnets, which consist of a resistive insert and a superconducting outsert. The superconducting coil is located outside the resistive coil so it does not experience the fields larger than the 24 Tesla limit. The magnetic field from both the resistive and superconducting coils superimpose to form a field larger than achievable by superconducting or resistive magnets alone.

The National High Magnetic Field Laboratory (NHMFL) is currently constructing a 36 T, 40 mm bore series-connected hybrid (SCH) magnet. While this magnet will not reach 45 T, it will have lower operating cost and the 40 mm diameter of the bore is appropriate for NMR. This work is intended for the SCH magnet, which is not yet completed. For this reason, the work shown in this dissertation was developed, tested, and verified using two different magnets.

A 7.1 T superconducting magnet shown in Figure 1.1 was used to develop this work in an environment where field strength is nearly constant. Using this magnet, artificial field fluctuations can be superimposed on the magnetic field using a current amplifier and disturbance coil, allowing one to test design performance in presence of known field fluctuations. The details of the amplifier and disturbance coil will be discussed in Section 2.2. A powered magnet developed with support of the Keck foundation [16] was used to develop and verify the work presented in this dissertation. The Keck magnet shown in Figure 1.2 has an adjustable field strength up to 25 T and a 52 mm diameter bore, which is appropriate for NMR.

Figure 1.1. Photograph of the 7.1 T superconducting magnet used to develop and test feedback compensators for reducing field fluctuations.

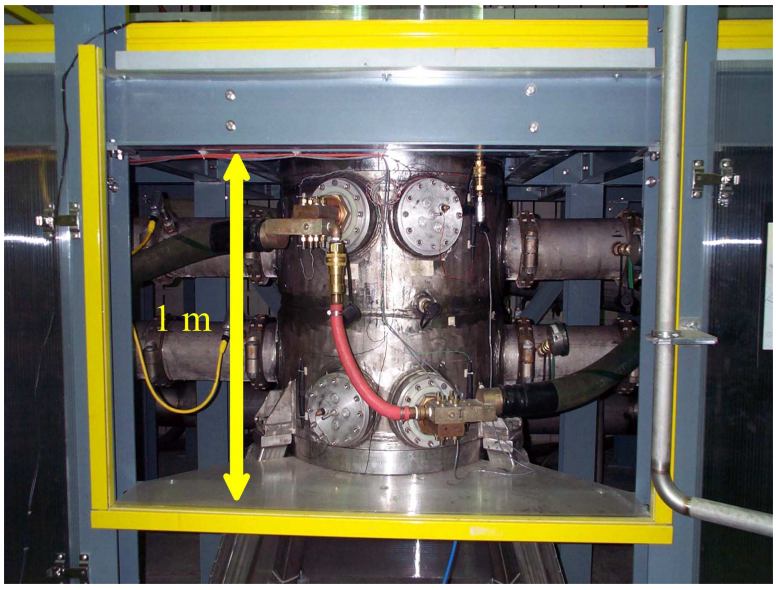

Figure 1.2. Photograph of the Keck powered magnet used to acquire experimental data which verifies the field fluctuation reduction provided by feedback compensation.

Although powered magnets overcome B_0 limitations of superconducting magnets, they present two significant engineering challenges. First, these magnets produce fields that are not spatially uniform. This spatial field inhomogeneity broadens the linewidth of the NMR spectra and reduces the SNR of the NMR signal [17]. In the time domain, this means the NMR signal decays faster in powered magnets which is undesirable for NMR spectroscopy. Second, the B_0 magnetic field in powered magnets has amplitude variations in time. These temporal field fluctuations distort both the amplitude and phase of consecutive NMR signals [18]. This limits the effectiveness of coherent signal averaging, which many NMR spectroscopy experiments require to improve SNR. More importantly, it becomes impossible to perform multidimensional NMR experiments.

To illustrate the effects of spatial field inhomogeneity and temporal field fluctuations on NMR, Figure 1.3 compares the NMR response obtained using identical experimental protocols in superconducting and powered magnets operating at 7.1 Tesla. In this example, the NMR signal is a spin echo generated by the application of two radio frequency (RF) pulses separated by one-half the time-to-echo (T_E). The spin echo occurs T_E seconds from the application of the first RF pulse. This basic pulse sequence is repeated 80 times, where the time between each sequence is chosen long enough for the NMR system to return to thermal equilibrium. Figure 1.3 (a) and (b) shows all 80 spin echoes acquired on each magnet for a T_E value of 5 ms.

In the superconducting magnet, the spatial field inhomogeneity and temporal magnetic field fluctuations are negligible over the duration of the experiment. The resulting spin echoes decay slowly and align in time with the same phase, as shown in Figure 1.3 (a). In stark contrast, the spin echoes acquired in the Keck powered magnet decay much faster and no longer align in time, as shown in Figure 1.3 (b). This is due to the presence of spatial field inhomogeneity and temporal field fluctuations in this powered magnet.

The spatial field inhomogeneity in powered magnets has been improved by two techniques known as shimming and sample spinning. Magnetic, or active shimming has been effective in improving spatial field inhomogeneity for superconducting magnets [19, 20]. This technique

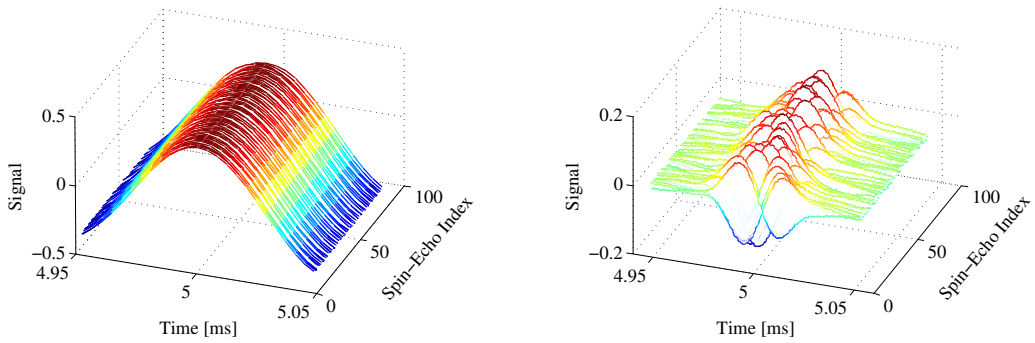

(a) (b)

Figure 1.3. Consecutive spin echo responses in a (a) 7.1 T superconducting magnet and the (b) Keck powered magnet operating at 7.1 T.

could, in principle, be applied to powered magnets. An alternative approach for shimming is using ferromagnetic, or passive shims to improve spatial field inhomogeneity in powered magnets [21, 22]. Additionally, the effects of spatial field inhomogeneity can be reduced by spinning the sample while it is placed inside the magnet [23, 24]. Further improvements on spatial field inhomogeneity are left to the magnet designers. Reducing temporal field fluctuations poses another challenging task and is the focus of this dissertation. The sources of these fluctuations are described next followed by a review of techniques for reducing them.

1.2 Sources of Temporal Field Fluctuations

Unlike superconducting magnets, powered magnets require continuous power sources with a coil made from normal-metals. Large currents are required to achieve high field strengths B_0, which means considerable power will be dissipated as heat in the self-resistance of the coils. Therefore, a water cooling system is necessary to regulate coil temperature and prevent thermal damage.

While powered magnets provide substantially larger magnetic fields than superconducting magnets, they introduce significant temporal field fluctuations. There are two primary sources of temporal field fluctuations in powered magnets. The first source is variations in the power supply current often described as power supply ripple. The second source is variations in flow

rate and temperature of cooling water.

Despite efforts to eradicate it, the power supply ripple has not been completely eliminated. Figure 1.4 shows the block diagram of one of the four 10 MW power supplies used at the NHMFL [25, 26]. Substation power at 12.38 kV is stepped down to 460 V rms using a step-down transformer. The voltage is converted from AC to DC by the rectifier assembly, which is comprised of thyristors whose firing angles determine the DC voltage level output of the rectifier. The combination of the firing angle controller and rectifier produce the DC voltage level output with a ripple [26]. A passive filter eliminates a portion of the ripple at the rectifier output. The remaining ripple is partially removed by a feedback loop consisting of an active filter, a magnetically coupled transducer that measures variation in current, and a digital controller. Despite these two stages of filters, power supply ripple still exist with harmonics of 60 Hz.

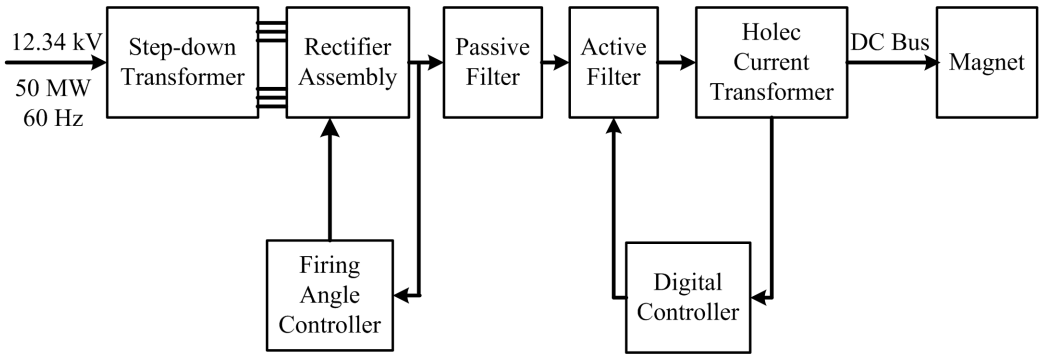

Figure 1.4. Block diagram of the power supply [27].

Magnetic field is directly proportional to current from the power supply and so the spectrum of field fluctuations contains the same harmonics as the power supply ripple. Figure 1.5 shows a series of magnitude spectra of the temporal field fluctuations observed in the Keck powered magnet operating at 7.1 T. This field was chosen over 25 T to reduce operating cost and to compare results to a 7.1 T superconducting magnet.

The four curves in Figure 1.5 represent separate magnitude spectra observations, each obtained using inductive field measurements, that span a two year period. The small magnitude

variations between the curves can be attributed to fact that multiple users present a varying load to the NHMFL power supply system. These magnitude spectra reveal components of power supply ripple located at harmonics of 60 Hz, and show that the amplitude of the 60 Hz component is about 0.16 Gauss rms [28]. Furthermore, from the standpoint of designing a feedback control system to reduce field fluctuations, it is important to note that the spectral location of the peaks remain fixed for each observation.

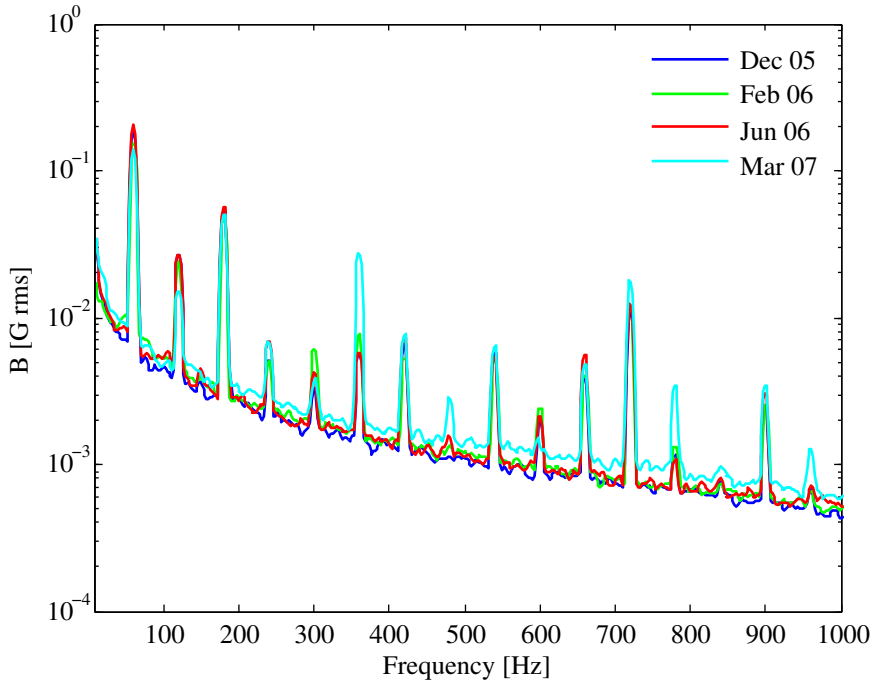

Figure 1.5. Magnitude spectra of the temporal magnetic field fluctuations in the Keck powered magnet operating at 7.1 T [28].

Based on analysis of the power supply system, the output of the rectifier assembly in Figure 1.4 should only contain harmonics above 1440 Hz. This suggests that the 60 Hz harmonics are being introduced in the feedback loop of the active filter, holec current transformer, and digital controller. If this is the case, one would not expect the amplitude of the 60 Hz harmonics to increase with magnetic field strength, as this is set by the DC current at the output of the rectifier assembly. To test this hypothesis, the amplitude of the 60 Hz, 120 Hz, and 180 Hz components

were measured as a function of magnetic field strength.

Figure 1.6 shows the measured amplitude of the 60 Hz, 120 Hz, and 180 Hz components for magnetic field strengths of 3 T, 9 T, 15 T, 21 T, and 25 T. The amplitudes of these components remain relatively constant as magnetic field strength increases from 3 T to 25 T. This supports the hypothesis that the 60 Hz harmonics do not arise from the power supply rectifier, rather they are introduced from the feedback loop of the active filter, holec current transformer, and digital controller. This observation may help guide future improvement in power supply design.

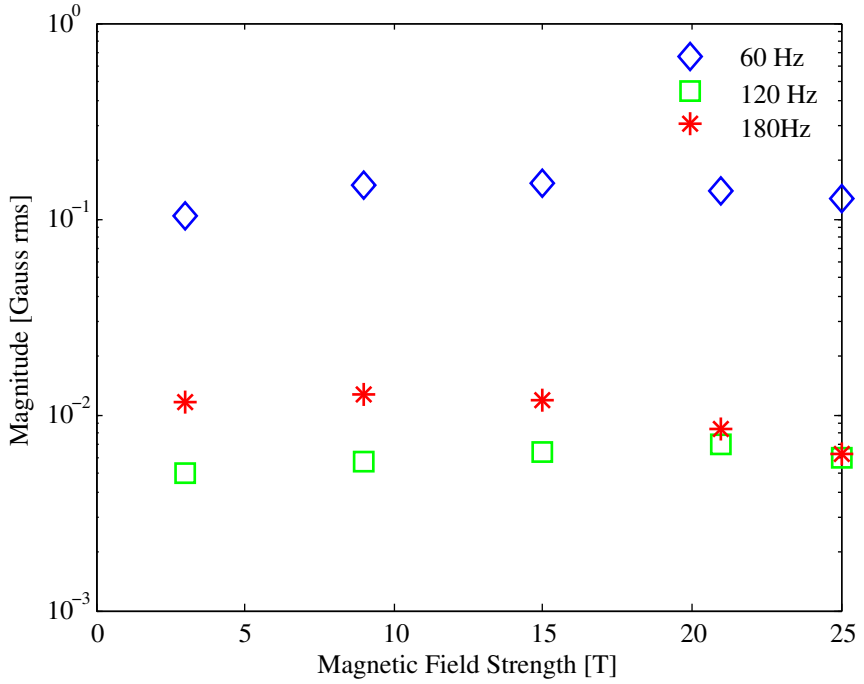

Figure 1.6. Magnitude spectra of 60 Hz harmonics for the Keck powered magnet operating at different magnetic field strengths.

While the amplitude of the 60 Hz component is much smaller than the magnetic field strength B_0, it will have a significant effect on NMR spectroscopy. For example, consider a NMR signal with a nominal 100 Hz linewidth. Section 3.3 demonstrates that a 60 Hz field fluctuation with an amplitude of 160 mG, which was measured experimentally, broadens the linewidth from 100 Hz to 190 Hz. The 60 Hz field fluctuation broadens the linewidth to a value greater than the

nominal 100 Hz, which is undesirable for NMR spectroscopy.

The second source of temporal field fluctuations comes from variations in flow rate and temperature of the cooling water. High field powered magnets are designed to be water cooled to remove the power dissipated in the coil. For example, full field operation of the Keck powered magnet requires 38.8 kA of current resulting in approximately a 490 V drop across the coil [2]. The magnet dissipates 19 MW (38.8 kA $\times$ 490 V) as heat in the self-resistance of the coil, which is contained in a volume of approximately 0.681 m^3. The heat per volume dissipated within the magnet is 28 W/cm^3. This is a considerable amount of heat per volume, and so the coil requires a water cooling system to maintain temperature. Variations in flow rate and temperature of the cooling water generated by the water cooling system leads to temporal field fluctuations.

Figure 1.7 shows a diagram of the coil and cooling water flow for a powered magnet [30]. The coil of these magnets are composed of copper plates, known as Bitter plates, separated by insulating layers. A series of holes in each plate allows cooling water to flow through the coil. The cooling water flows through the Keck powered magnet at approximately 7000 liters per minute. The water enters the magnet at 9 °C and is heated to 43 °C by the time it exits the magnet [2].

It is difficult to analytically predict the relationship between cooling water variations and temporal field fluctuations. However, even very small changes in cooling water temperature will have significant effects on the NMR signal. To illustrate this effect, consider the Larmor frequency

$$f_0 = \gamma B_0, \tag{1.1}$$

where γ is the gyromagnetic ratio and B_0 is the magnetic field strength. Suppose γ has a value of 42.576 MHz/T, which is the gyromagnetic ratio of hydrogen nuclei. If cooling water temperature changes by 0.1 °C, then experimental measurements have shown for a resistive magnet at 24 T that the B_0 field changes by 0.41 Gauss [31]. This corresponds to a shift in f_0 of 1.74 kHz, which is large compared to the desired 100 Hz linewidth. Even though cooling water changes

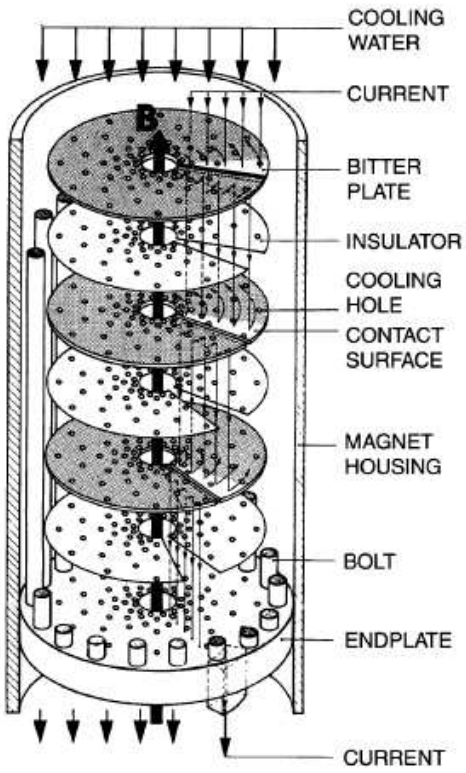

Figure 1.7. Diagram of the coil and cooling system [30].

by 0.1 °C, there is a significant impact on the NMR signal. For the Keck powered magnet at 25 T, recent measurements show 9 Gauss peak to peak field fluctuations over a period of two minutes primarily due to cooling water variations. These fluctuations shift the Larmor frequency of hydrogen nuclei by 38 kHz, well over the 100 Hz desired for NMR experiments.

Frequency shifts are typically reported by NMR spectroscopists in parts per million (ppm), which is expressed as

$$\frac{\delta f}{f_0} \times 10^6, \tag{1.2}$$

where f_0 is the Larmor frequency defined in equation 1.1 and δf is the shift in this frequency due to field changes. In the example above at 25 T, the 38 kHz shift in frequency is equivalent to 35.7 ppm and the 100 Hz linewidth is equivalent to 0.09 ppm. Because Larmor frequency is proportional to field, a 35.7 ppm shift in frequency corresponds to 35.7 ppm change in B_0. For

the reminder of this dissertation, frequency shifts may be reported in Hertz (Hz), Gauss (G), or parts per million (ppm).

In this section, two primary sources of temporal field fluctuations were discussed. The power supply ripple is the source of the higher frequency components such as 60 Hz harmonics in the spectrum of field fluctuations. Therefore temporal field fluctuations due to high frequency components of power supply ripple are often referred to as higher frequency fluctuations. The cooling water variations affect field fluctuations over a period of minutes [31]. Additionally, low frequency 1/f noise of the power supply ripple may also contribute to field fluctuations. The cooling water variations and 1/f noise of power supply ripple are the source of lower frequency components in the spectrum of field fluctuations. Therefore temporal field fluctuations due to cooling water variations and 1/f noise of the power supply ripple are often referred to as lower frequency fluctuations. Throughout this dissertation, temporal field fluctuations due to high frequency components of power supply ripple are referred to as higher frequency fluctuations. Conversely, temporal field fluctuations due to cooling water variations and 1/f noise of power supply ripple are referred to as lower frequency fluctuations.

Despite improvements to the power supply and cooling water system, these are still sources of significant temporal field fluctuations with peak to peak values as much as 9 Gauss. The goal of this dissertation is to present a method to further reduce field fluctuations from these sources in powered magnets. In this way, the higher field strengths of powered magnets can improve NMR spectroscopy without the disadvantages of temporal field fluctuations.

Several mitigation strategies are available for reducing temporal field fluctuations in magnets. Open-loop mitigation strategies reduce fluctuations without feedback control while closed-loop strategies reduce fluctuations with feedback control. Section 1.3 provides an overview of available open and closed-loop mitigation strategies. As the focus of this dissertation is utilizing feedback control to reduce fluctuations, the closed-loop strategies are discussed in more detail in Sections 1.4 and 1.5.

1.3 Mitigation Strategies

The open-loop mitigations strategies include passive suppression, post processing NMR signal data using an independent measurement of field fluctuations, and designing experiments intrinsically insensitive to field fluctuations. Passive suppression techniques surround the NMR sample with a shield consisting of highly conductive material [32, 33, 34]. Temporal magnetic field fluctuations induce eddy currents within the shield, which by Lenz's law, generate magnetic fields opposing the field fluctuations. Using this approach, Sigmund reported a 26 dB reduction of the 60 Hz component of the temporal field fluctuations [33].

Another open-loop strategy is to acquire NMR signal data and post process it using an independent measurement of field fluctuations. An appropriate deconvolution algorithm can be used to post process the NMR signal data using some measurement of the field fluctuations [35]. The measurement of field fluctuations may conveniently be derived from an inductive pickup coil placed close to the NMR sample [36, 37]. For experiments requiring a greater degree of correction than deconvolution, a technique know as HEteroNuclear PhasE Corrected (HENPEC) spectroscopy has been proposed [38]. Here the measurement of field fluctuations is derived from a NMR reference signal. In conjunction with sample spinning, HENPEC has produced linewidths of NMR spectra as small as 43 Hz (0.04 ppm) at 25 T.

A third open-loop strategy is to use a RF pulse sequence whose NMR response is insensitive to temporal field fluctuations. One such experiment, HOMOGENIZED-CPMG, allowed for high resolution NMR in the presence of both field inhomogeneity and temporal field fluctuations [9]. Using this technique, Lin *et al.* measured NMR spectra linewidths of about 0.02 ppm using a sample of water and acetone in the Keck powered magnet. Another experiment, described as ultrafast single-scan 2D, captured the entire dataset within 5-10 ms, which is much shorter than typical NMR experiments [2]. This removed the need to mitigate long term, or low frequency field fluctuations. NMR spectra with sub-ppm linewidths were observed in spite of the fast, or

high frequency fluctuations still present in the magnet. Related approaches have been proposed recently [39, 40, 41].

In an effort to further reduce temporal field fluctuations, this dissertation considers closed-loop mitigation strategies using feedback control. This technique requires a sensor, feedback compensator, and correction coil driven by a current amplifier. The sensor estimates temporal field fluctuations, which is coupled with a feedback compensator. The compensator generates a correction field using the amplifier and correction coil. The resulting frequency dependent reduction in field fluctuations is determined by the compensator design.

There are two types of sensors for feedback control studied in this dissertation. The first sensor uses a pickup coil in series with an integrating preamplifier to obtain inductive measurements of the field fluctuations. Recall that the magnitude spectra of field fluctuations in Figure 1.5 were determined using inductive measurements. For these measurements, a pickup coil is positioned near the NMR sample, and uses Faraday's law to provide an open circuit voltage that is proportional to the derivative of temporal field fluctuations. The integrating preamplifier then integrates the pickup coil voltage, providing an output voltage proportional to temporal field fluctuations. Section 1.4 provides a more detailed discussion of inductive sensors and feedback control using inductive measurements.

The second sensor measures the NMR signal, and estimates field fluctuations by observing changes in the NMR signal of a reference sample. The reference sample may be dissolved in the NMR sample of interest or it can be placed in a separate tube within the magnet. Comparing the spectral characteristics of each sensor, inductive measurements are well suited for estimating higher frequency fluctuations while NMR measurements are better for estimating lower frequency fluctuations. Section 1.5 provides a more detailed discussion of NMR sensors and feedback control using NMR measurements.

1.4 Feedback Control using Inductive Measurements

In the late 1950s, Primas and Gunthard first demonstrated feedback control using inductive measurements to reduce field fluctuations for a 0.6 T permanent magnet [42, 43]. It was observed that the surrounding stray fields and temperature variations of the magnetic material produced field fluctuations in the permanent magnet. These field fluctuations were sensed using inductive measurements, and fed back through an analog proportional compensator coupled with a correction coil, reducing fluctuations up to 0.16 Hz by as many as 70 dB. Ten years later, Gottlieb *et al.* described a similar approach to attenuate field fluctuations in a resistive magnet operating at 12.53 T [44]. An analog feedback compensator was again coupled to a correction coil using inductive measurements, reducing field fluctuations by 34 to 40 dB for frequencies up to 500 Hz. The inductive measurements for both these approaches limit compensation of lower frequency components because they have poor SNR at lower frequencies which will be discussed in subsection 1.4.2.

For the Keck powered magnet operating at 25 T, which was used to acquire experimental results for the work in this dissertation, substantial reduction of temporal field fluctuations was shown by Li *et al.* in 2011 [27, 28]. Here inductive measurements were fed back through a digital sampled-data compensator coupled to an amplifier and correction coil. This work had two advantages over earlier studies. First, the compensator design utilized a sampled-data compensator instead of an analog compensator. Analog compensators are implemented with analog electronics, which impedes complex compensator designs and modifications in practice. A sampled-data compensator enables complex compensator designs that can be rapidly implemented, tested, and modified. Second, the compensator design considered frequency response characteristics of the feedback control loop. Analyzing the control loop frequency response allows for improved compensator design and better reduction of field fluctuations.

Li's compensator design was developed to suppress field fluctuations with spectral characteristics shown in Figure 1.5. Reductions of field fluctuations was shown up to 1 kHz, and the 60 Hz component of the field fluctuations was reduced by as many as 64 dB. Subsection 1.4.1 discusses results obtained with this approach and subsection 1.4.2 discusses the limitations using Li's approach to reduce lower frequency fluctuations.

1.4.1 Model-Based Control Design

One of Li's significant contributions was using an identified model of the feedback control loop when designing the compensator. This model was identified from experimental measurements of the transfer function from the amplifier and correction coil to the inductive measurement output. Using this identified model provided significant improvement in compensator design, and hence fluctuation reduction, when compared to previous designs using inductive measurements.

Figure 1.8 shows the block diagram of the inductive feedback control system used by Li *et al.* The pickup coil is placed in series with the integrating preamplifer. The inductive measurement is observed at the output of the integrating preamplifier, whose voltage is proportional to temporal field fluctuations. An analog-to-digital converter (ADC) samples the inductive measurement and supplies these sampled-data measurements to the compensator. The compensator generates a sampled-data correction voltage that is converted to an analog correction voltage using a digital-to-analog converter (DAC). The ADC, compensator, and DAC allow the use of a sampled-data compensator which is one of Li's significant contributions. The analog correction voltage is converted to a correction field by the current amplifier and correction coil. The identified models of the pickup coil, integrating preamplifier, current amplifier, and correction coil used for this dissertation will be shown in Section 2.2.

The compensator in Figure 1.8 was defined as a phase-lead-lag internal model principle (PLL-IMP). The IMP component of this compensator reduces amplitudes of the most significant 60 Hz harmonics by applying high gain at these frequencies. Using the magnitude spectra in Figure 1.5,

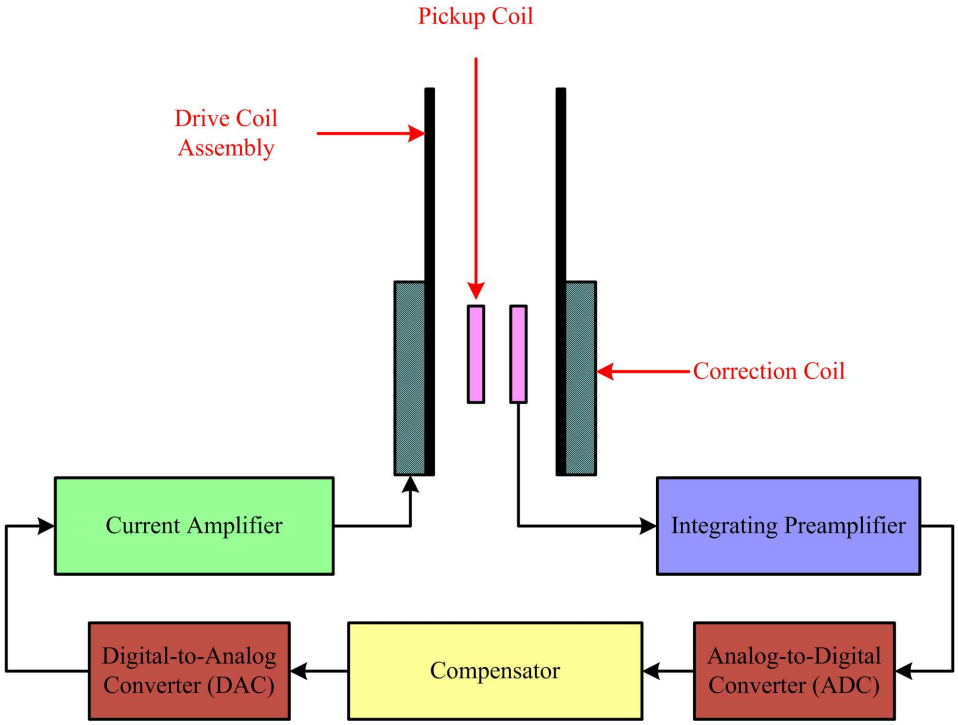

Figure 1.8. Block diagram of feedback system using induction measurements.

the 60, 120, 180, and 720 Hz freqeuncy components were identified as the most significant harmonics. The PLL component of the compensator shapes the frequency response of the feedback control loop to make the closed loop system stable. Additionally, this portion of the compensator has small gain at low frequencies so that a DC offset will not saturate the equipment.

The inductive feedback control system shown in Figure 1.8 was used to compare the performance of proportional and PLL-IMP compensators. Inductive measurements were used to determine the magnitude spectra of temporal field fluctuations for the cases with no compensation, proportional compensation, and PLL-IMP compensation. The gain of the proportional compensator was chosen as 1.6 while the DC gain of the PLL-IMP compensator was chosen as 6. These were the largest gains achievable for a stable closed-loop system, thereby achieving maximum reduction of field fluctuations for each design.

Figure 1.9 shows the magnitude spectra in Gauss rms for frequencies from 1 Hz to 1.6 kHz [27, 28]. The proportional compensator, which is independent of frequency, yields the same

magnitude spectra reduction for all frequencies. The PLL-IMP compensator yields significantly greater reduction in magnitude spectra at the 60, 120, 180, and 720 Hz frequency components. In addition, the baseline magnitude spectra is reduced more than the proportional compensator for frequencies below 800 Hz. These results are expected as the PLL-IMP was designed to reduce these harmonics and the baseline spectra in this way. A modified design of this PLL-IMP compensator will be presented in Section 6.2.

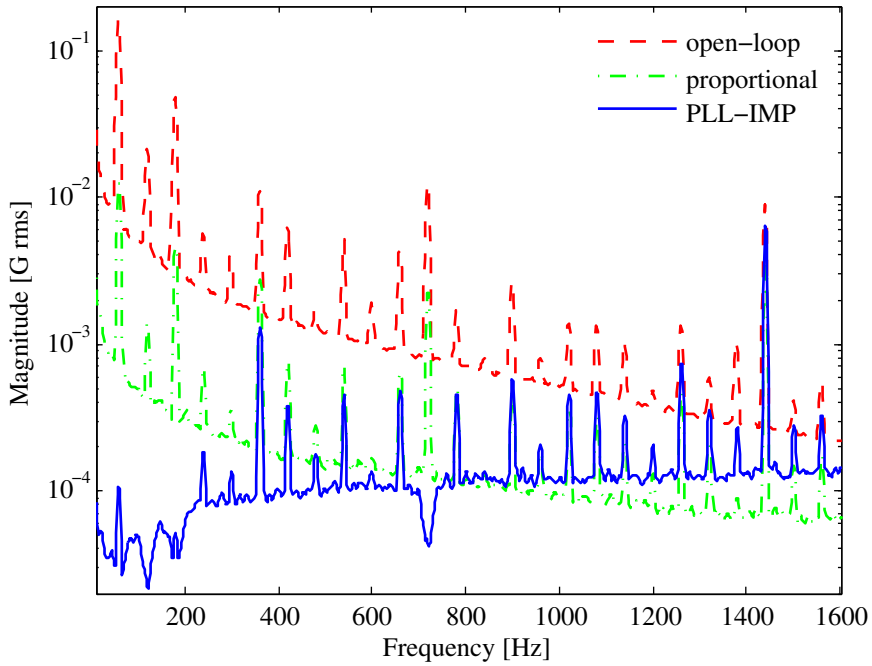

Figure 1.9. Magnitude spectra of the temporal magnetic field fluctuations in the Keck powered magnet operating at 7.1 T, with and without feedback compensation.

The ultimate objective of this study is to improve the quality of the NMR signal by reducing the amplitude of temporal field fluctuations. For this reason, NMR spin echoes as described in Section 1.1 were acquired while applying inductive feedback control. One hundred spin echoes were acquired with T_E of 7 ms in the Keck powered magnet operating at 7.1 T. The time between each spin echo pulse sequence is one second to allow the NMR system to relax to thermal equilibrium. Figure 1.10 shows every tenth spin echo acquired with (a) proportional and

(b) PLL-IMP compensation. Figure 1.10 is similar to Figure 1.3, except that the spin echoes are collapsed into one plane, and the time scale is shifted so that the spin echo is centered at zero seconds. For proportional compensation, there are still significant field fluctuation amplitudes present that affect the amplitude and phase of consecutive spin echoes. This is shown in Figure 1.10 (a) as multiple spin echoes are not aligned. For PLL-IMP compensation, the field fluctuations are significantly reduced and thus the amplitude and phase of consecutive spin echoes are similar. Figure 1.10 (b) shows that the spin echoes are now more aligned with a PLL-IMP compensator than a proportional compensator.

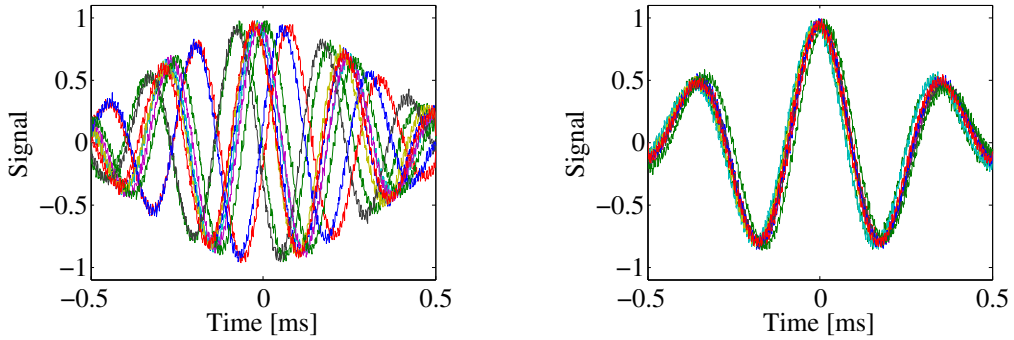

(a) (b)

Figure 1.10. Spin echo responses for a T_E value of 7 ms in the Keck powered magnet operating at 7.1 T using (a) proportional and (b) PLL-IMP flux regulation.

1.4.2 Limitations

The inductive feedback control system demonstrated by Li *et al.* is designed to reduce higher frequency fluctuations associated with power supple ripple. There are two factors that limit performance of inductive feedback control for lower frequencies. The first limitation is that inductive measurement SNR decreases with frequency due to 1/f noise and the fact that open-circuit pickup coil voltage is proportional to frequency. The second limitation results from challenges in implementing the integration operation at lower frequencies. Because of these limitations, the magnitude spectra in Figure 1.9 is only shown for frequencies above 1 Hz. This subsec-

tion discusses these limitations in greater detail. Further details of the integrating preamplifier instrumentation, identified models, and limitations are provided in Chapter 2.

It was mentioned previously that inductive measurements use a pickup coil to provide an open circuit voltage that is proportional to the derivative of temporal field fluctuations. This implies that the open circuit voltage has a linear dependence on frequency. In order to remove this linear dependence on frequency, the open circuit pickup coil voltage is integrated, providing an output proportional to the field fluctuation. The integration of the pickup coil voltage is realized with device described as the integrating preamplifier.

When implementing the integrating preamplifier, a pure integrator is undesirable as small DC offsets in analog instrumentation will saturate the integrator output. Instead, the transfer function of the integrating preamplifier is modeled as a low pass filter with a transfer function

$$H_{int}(j\omega) = \frac{K}{j\omega\tau + 1}, \tag{1.3}$$

where K is the DC gain and τ is the time constant, which was 3 seconds for the integrating preamplifier used by Li *et al.* For frequencies above $1/\tau$, the model in equation 1.3 behaves as an integrator with a -20 dB per decade slope. Conversely, for frequencies below $1/\tau$, the model has a constant gain K, and no longer behaves as an integrator.

Therefore inductive measurements do not provide an accurate estimate of field fluctuations with frequencies below $1/\tau$ because the integrating preamplifier no longer behaves as an integrator. The value of τ could be increased to achieve a smaller cutoff frequency by placing larger resistors or capacitors in the integrating circuit. Modifications to the integrating preamplifier to increase τ will be briefly discussed in Section 2.3.

In addition to the low pass filtering effects of the integrating preamplifier, inductive measurements are also limited by low frequency noise sources. For example, below a certain frequency, the integrating preamplifer suffers from 1/f noise. This noise reduces signal SNR for measure-

ments at these frequencies, making it difficult to estimate field fluctuations from the integrating preamplifier output. Other low frequency noise sources exist in inductive measurements, reducing the effectiveness of estimating lower frequency fluctuations from such measurements.

The following experiment was designed to demonstrate the low pass filtering affects and low frequency noise in inductive measurements. For this experiment, a current amplifier and disturbance coil was used to superimpose a low frequency disturbance field onto the 7.1 T field of the superconducting magnet. The disturbance field was chosen to change slowly over a 5 second period to imitate a lower frequency fluctuation. The applied disturbance field was estimated using inductive measurements obtained from the integrating preamplifer output.

Figure 1.11 illustrates the results of this experiment. The field fluctuation estimated from the inductive measurement has much more noise than the applied disturbance due to the aforementioned low frequency noise sources. In addition, the exponential shape of the estimate reveals the low pass filtering effect of the integrating preamplifer at lower frequencies. In the case of a low frequency disturbance field, the integrating preamplifier no longer behaves as an integrator, making the inductive estimate of the field fluctuation inaccurate. This effect is not surprising because τ is 3 seconds and the disturbance ramp occurs over 5 seconds. Reducing τ would improve the filtering effects of the integrating preamplifier, but would not improve the low frequency noise limitation.

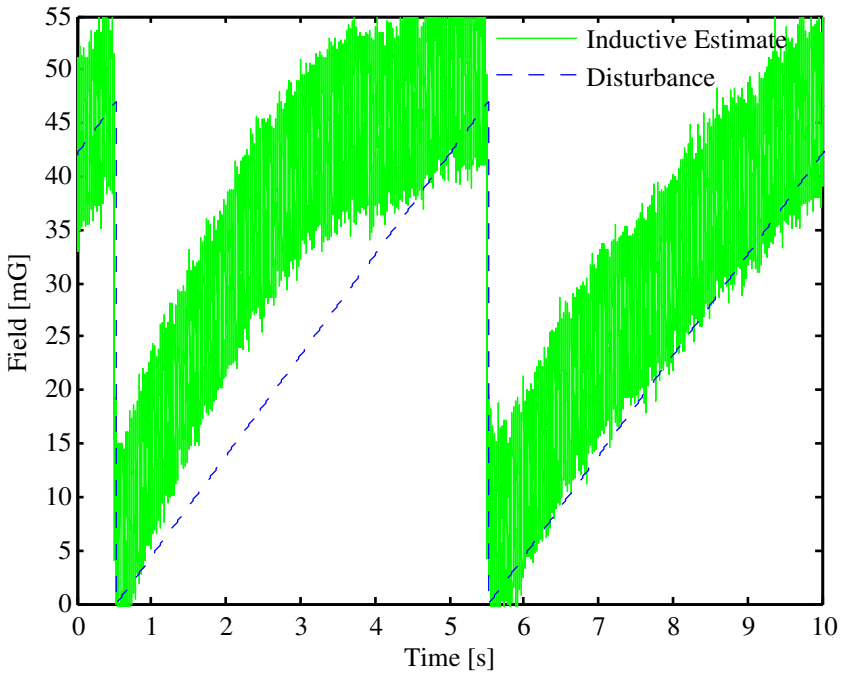

Figure 1.11. Inductive measurement for a low frequency field fluctuation superimposed on the 7.1 T field of a superconducting magnet.

The lower frequency limitations of inductive measurements can be overcome by estimating field fluctuations using NMR measurements. Using the NMR signal, field fluctuations can be estimated by observing changes in the NMR response of a reference sample, which has a Larmor frequency typically above 45 MHz. As a result, estimating temporal field fluctuations from NMR measurements is unaffected by low frequency noise sources that limit the inductive measurement system. The next section provides a discussion of feedback control using NMR measurements to estimate and reduce lower frequency fluctuations.

1.5 Feedback Control using NMR Measurements

An alternative, and often complimentary method to inductive feedback control is feedback control using NMR measurements. As mentioned previously, field fluctuations can be estimated by observing their effect on the NMR response. Therefore NMR measurements can be used in

feedback control to reduce the effects of field fluctuations. This approach has the advantage of being able to estimate field fluctuations down to DC without the limitations of the inductive measurements discussed in subsection 1.4.2.

Feedback control using NMR measurements is often defined in literature as field-frequency locks (FFL). Consequently, the acronym FFL will be used synonymously with NMR feedback control when describing these feedback control methods. Section 4 provides an extensive literature survey of FFL techniques over the last 60 years. From the literature, it was discovered that FFLs measure or estimate NMR signal components which are indirect or direct representations of the field fluctuations, and use them to reduce the effects of fluctuation on NMR. Thus in this dissertation FFLs are classified as indirect or direct.

Indirect FFLs measure NMR signal components which are indirectly related to field fluctuations. Under certain conditions to be discussed in Chapter 4, these NMR signal components represent field fluctuations well. Therefore these signal components can be used to estimate field fluctuations and reduce their effects on NMR.

In contrast to indirect FFLs, direct FFLs measure or estimate a NMR signal component which is directly related to field fluctuations. In this case, the NMR signal component is directly proportional to field fluctuations, and estimates of this component can be used to reduce the effects of fluctuations on NMR. While it may seem that direct FFLs are the most sensible approach, indirect FFLs have the benefit of being simpler and more convenient to implement. Section 4.1 provides a more detailed discussion of indirect and direct FFLs along with the NMR signal components used to estimate field fluctuations.

1.6 Performance Metrics

The performance metrics of the inductive feedback control system shown in subsection 1.4.1 where field fluctuation spectra and NMR spin echo signals. The reduction in field fluctuation spectra

and alignment of NMR spin echoes demonstrate reduction of higher frequency fluctuations, but not lower frequency fluctuations. This dissertation considers three performance metrics, defined in this section, that demonstrate reduction of both lower and higher frequency fluctuations.

The first performance metric is from a control systems viewpoint, where the system without feedback control and with feedback control is referred to as open and closed-loop respectively. The performance of the feedback control design can be evaluated by comparing the open and closed-loop frequency response of the transfer function from field fluctuations $B_f(t)$ to field output $B(t)$ while the system remains stable. As the magnitude of the transfer function B/B_f gets small, field fluctuations are reduced. The frequency response of B/B_f allows the control designer to quantify the amount of field fluctuation suppression for the frequencies of interest. Li *et al.* [27, 28] also used this performance metric but only derived it from inductive measurements. Chapter 6 shows this performance metric derived from NMR measurements.

The second and third performance metrics are from a NMR spectroscopy standpoint, where it is desirable to observe improvements in consecutive NMR signals. These metrics are derived from a NMR signal known as free-induction decay (FID), and are chosen to demonstrate reduction of higher and lower frequency fluctuations. An FID signal is an exponentially decaying sinusoid that is generated by the application of a single RF pulse. The RF pulse is repeated to obtain consecutive FID signals, where the time between each pulse is chosen long enough for the NMR system to return to thermal equilibrium. Higher frequency fluctuations modulate the frequency of a single FID, which broadens the linewidth of the FID magnitude spectra, and lower frequency field fluctuations shift the peak frequency of consecutive FID magnitude spectra [18]. The origin of an FID signal along with the effect of field fluctuations will be discussed in more detail in Sections 3.2 and 3.3.

The second performance metric used for this dissertation is the linewidth of FID magnitude spectra, which is defined as the bandwidth of the squared magnitude spectra at half its maximum value. In order to quantify a baseline measurement of linewidth, a series of consecutive FID

responses from the hydrogen nuclei of a NMR sample within the Keck powered magnet were acquired with no feedback compensation. These FID signals were processed by computing the magnitude spectra of each FID, aligning each FID spectra in frequency, and coherently averaging all FID spectra. The baseline measurement of linewidth is then the linewidth of the squared value of the average FID magnitude spectra.

The procedure for acquiring and processing this data will be discussed in detail in Section 6.3. The FID squared magnitude spectra, which is normalized by its maximum value for convenience, is shown in Figure 1.12. The double-sided arrow indicates the magnitude at which the linewidth of this spectra was calculated. With no compensation, the higher frequency fluctuations broaden the linewidth of the FID magnitude spectra to approximately 290 Hz. It is expected that when higher frequency field fluctuations are reduced, the linewidth of the FID spectra will be reduced. The effect of field fluctuations on linewidth will be studied in detail in Section 3.3.

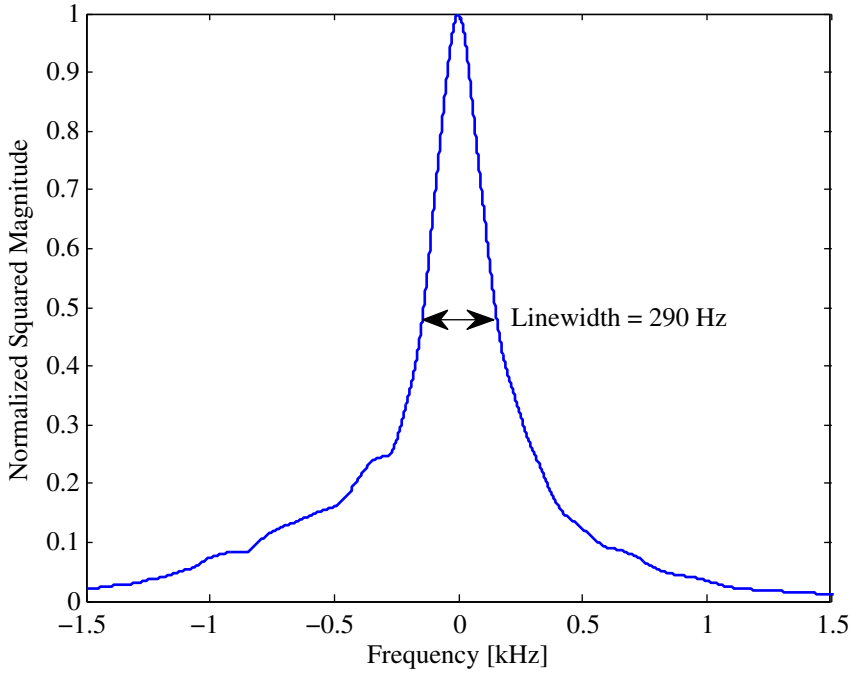

Figure 1.12. Normalized squared magnitude spectra of FID, Keck powered magnet operating at 25 T.

The third performance metric used for this dissertation is the peak frequency of consecutive FID magnitude spectra. The same FID responses used to derive the linewidth in Figure 1.12 were used to quantify a baseline measurement of this metric. These FID signals were processed by computing the magnitude spectra of each FID, and determining the frequency at which the spectra peak occurs. With no compensation, the peak frequency of the FID spectra as a function of time is the baseline measurement of this metric.

The procedure for acquiring and processing this data will also be discussed in detail in Section 6.3. The peak frequency of each FID magnitude spectra is shown in Figure 1.13 as a function of time. Recall that Larmor frequency is proportional to field, so FID spectra peak frequency can be represented in Hertz (Hz) or Gauss (G). Here the peak frequency is represented in Gauss because this is independent of the NMR sample nuclei. The circles indicate the FID spectra peak calculated at the time instant the FID was acquired. With no compensation, the lower frequency fluctuations shift the FID spectra peak by more than 9 G (36 ppm) over the duration of the experiment. The standard deviation of the shifts in spectra peaks is 2.96 G. It is expected that when lower frequency fluctuations are reduced, the shifts in FID spectra peaks will be reduced.

At this point one may ask why the second and third performance metrics were not derived from spin echo signals like those in Figure 1.10. Unlike FID signals, lower frequency fluctuations have very little effect on spin echo signals. For example, consider the consecutive spin echo signals in Figure 1.10, where the time-to-echo (T_E) of each signal was chosen as 7 ms. Field fluctuations that change quickly over 7 ms distort the phase coherence of consecutive echo signals [28]. If lower frequency fluctuations are present that change very little over 7 ms, consecutive spin echos will be phase coherent and the presence of lower frequency fluctuations cannot be observed. Therefore the performance metrics were derived from FID signals which can be used to observe the effects of both lower and higher frequency fluctuations on NMR.

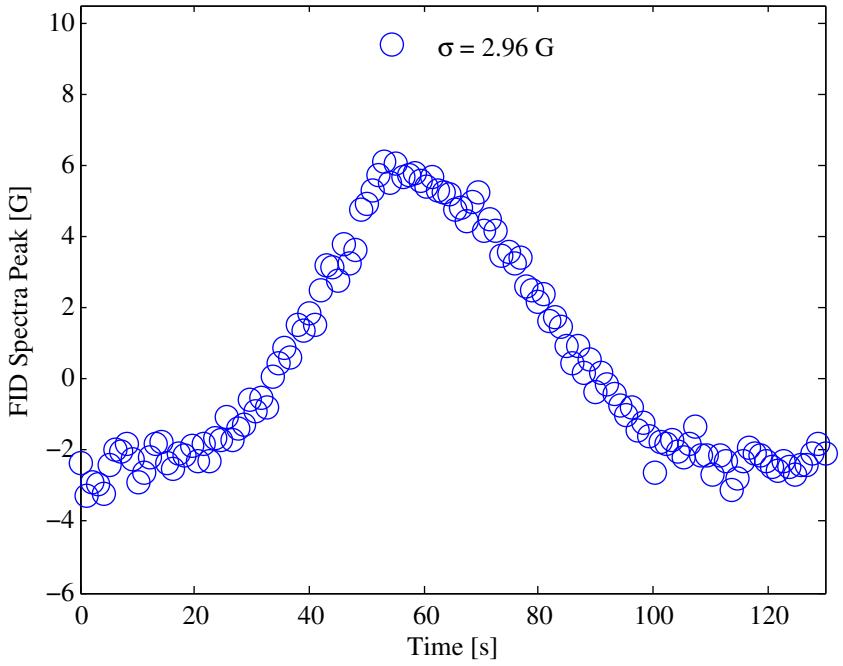

Figure 1.13. Peak frequencies from magnitude spectra of FIDs acquired on the Keck powered magnet operating at 25 T.

Using the three performance metrics described in this section, the contributions of this dissertation can now be stated. The following section discusses the contributions and organization of this dissertation.

1.7 Contributions and Organization

This dissertation presents the development of the feedback control system illustrated in the block diagram of Figure 2.1. This is a multi-loop, multi-rate feedback control system defined as a cascade control system because it is the cascade combination of a inductive feedback control loop and a direct FFL control loop, each with different sampling rates. The inductive feedback control loop is comprised of a current amplifier and correction coil, pickup coil and integrating preamplifier, and a compensator realized using a digital signal processor. The direct FFL control loop is defined as the amplifier and correction coil, NMR console and field estimator, and a direct

FFL compensator realized using a digital signal processor.

For the inductive feedback control loop, the pickup coil and integrating preamplifier provide an estimate of higher frequency fluctuations using inductive measurements. The analog signal at the integrating preamplifier output is sampled using an ADC at a fast sampling period T_F chosen as 20 μs to observe higher frequency fluctuations. The sampled-data inductive compensator, designed to reduce these fluctuations, provides an sampled-data correction voltage to the DAC. The DAC, amplifier, and correction coil convert the sampled-data correction voltage to an analog correction field.

In contrast to the inductive feedback control loop, the direct FFL control loop estimates lower frequency fluctuations using the NMR console and field estimator. The NMR console provides measurements to a chosen field estimator developed to sense lower frequency fluctuations. The lower frequency estimate is updated every T_S or 25 ms, which is modeled using a sampler with period T_S. The slow sample period T_S is much larger than T_F because the direct FFL loop updates much more slowly than the inductive feedback loop. Chapters 5 and 6 discuss the reasons for choosing T_S as 25 ms and T_F as 20 μs. The direct FFL compensator is a sampled-data compensator designed to reduce lower frequency fluctuations. This compensator provides a sampled-data correction voltage to the summer, which is combined with the correction signal from the inductive compensator, and converted to a analog correction field via a DAC, amplifier, and correction coil.

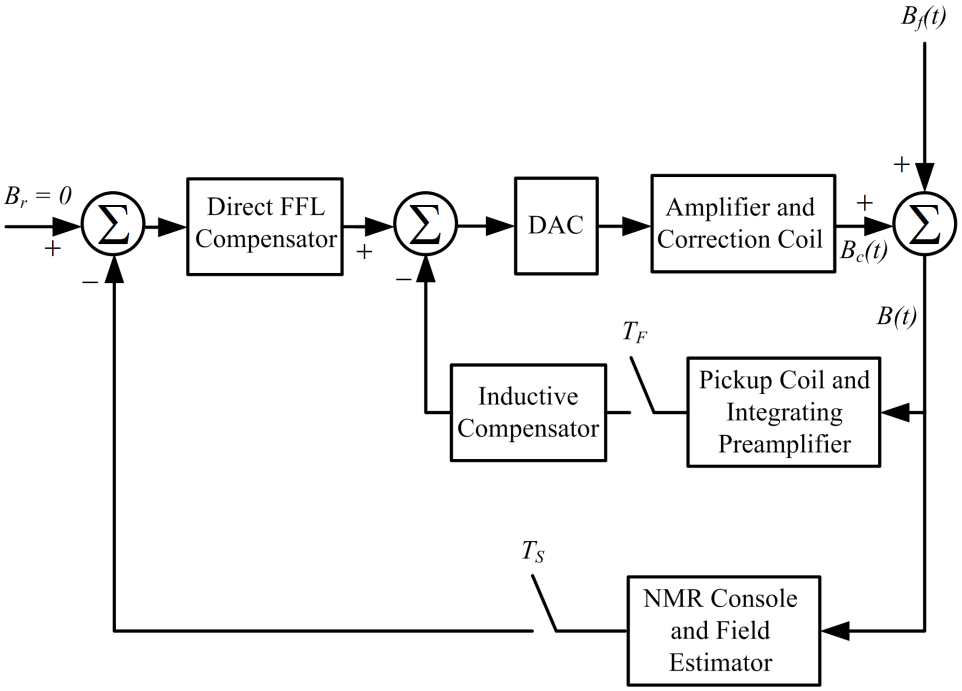

Figure 1.14. Block diagram of the cascade feedback control system for reducing lower and higher frequency fluctuations.

The contributions of the research work shown in this dissertation are:

- Demonstrate indirect FFL limitations which preclude their use in most powered magnets [57].
- Develop estimation methods for the NMR field estimator to use as a sensor for a direct FFL which overcomes limitations of indirect FFLs in powered magnets [62].
- Design and synthesize cascade feedback control system to reduce lower and higher frequency fluctuations in powered magnets [62].
- Demonstrate field fluctuation reduction by comparing the open and closed-loop frequency response of the transfer function B/B_f in a powered magnet [62].
- Demonstrate NMR spectroscopy improvement in a powered magnet by comparing open and closed-loop linewidth and shifts in peak frequencies of FID magnitude spectra [62].

The first contribution will be included in a publication which designs a indirect FFL using a small-signal model of the NMR dynamics [57]. The remaining contributions will be disseminated in a publication describing the development and verification of the cascade feedback control system [62]. Additional NMR experimental results afforded by the cascade feedback control system will also be submitted for publication [63].

Chapter 2 describes the instrumentation used for the inductive feedback control loop. Chapter 3 describes NMR physics and the available instrumentation for acquiring NMR measurements for estimating field fluctuations as well as deriving performance metrics. Chapter 4 provides a more detailed description of feedback control methods using NMR measurements, or FFLs, and their application to powered magnets. A particular indirect FFL design commonly used in superconducting magnets is studied, and the limitations of this FFL design in powered magnets is shown.

Chapter 5 develops candidate estimation methods for the NMR field estimator. Experimental measurements are used to compare the candidate methods, and one method is chosen as the NMR field estimator. This chapter also assesses the implementation of the NMR field estimator and its limitations when using it as a sensor for the direct FFL. Chapter 6 shows the cascade feedback control design to simultaneously reduce lower and higher frequency fluctuations. The lower frequency fluctuations are sensed using the NMR console and field estimator while the higher frequency fluctuations are sensed inductively using the pickup coil and integrating preamplifier. The field fluctuation reduction is verified experimentally by comparing the open and closed-loop frequency response of field fluctuations as well as the open and closed-loop linewidth and peak frequency shifts in FID magnitude spectra.

Chapter 2

Inductive Feedback Control Instrumentation

Section 1.7 introduced the cascade feedback control system as a cascade combination of an inductive feedback control loop and a direct FFL control loop. For convenience, the block diagram of this feedback control system is repeated in Figure 2.1. This chapter describes instrumentation for implementing the inductive feedback control loop of the cascade feedback control system.

Section 2.1 describes the pickup coil and integrating preamplifier, and how inductive measurements represent an estimate of field fluctuations. Section 2.2 describes the current amplifier and drive coils for superimposing fields on the B_0 field of the magnet. The drive coils include a correction coil for reducing field fluctuations, and a disturbance coil for superimposing disturbance field fluctuations on the B_0 field. Section 2.3 identifies analytical models of the pickup coil and integrating preamplifier as well as the current amplifier and drive coils using experimental data. The inductive compensator design for reducing higher frequency fluctuations will be discussed in detail in Chapter 6.

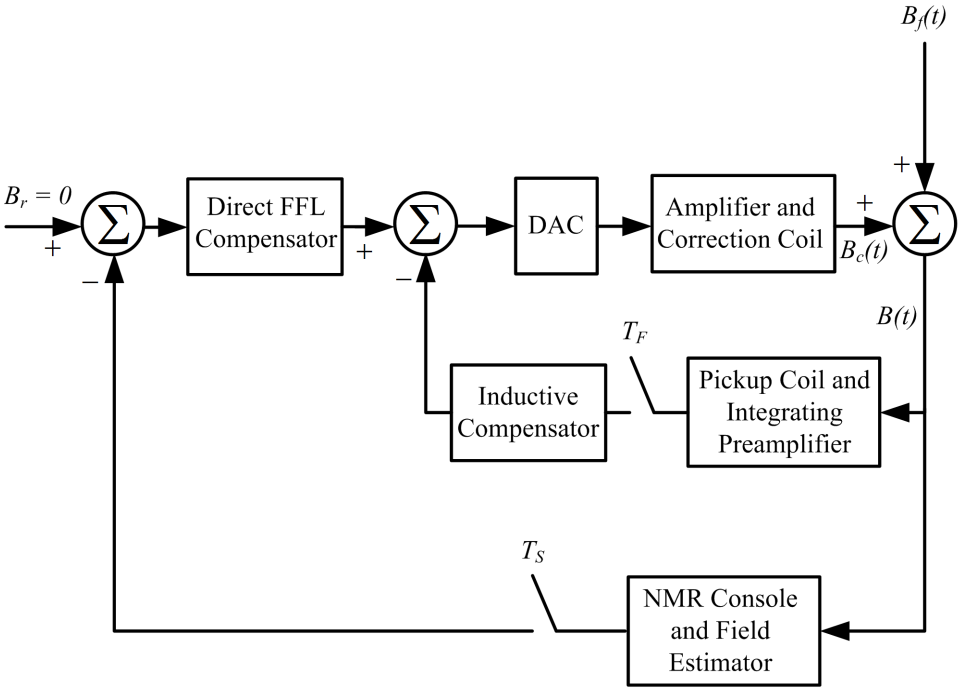

Figure 2.1. Block diagram of the cascade feedback control system for reducing lower and higher frequency fluctuations.

2.1 Pickup Coil and Integrating Preamplifier

The pickup coil used in this research work is installed within a High-Resolution Magic Angle Spinning (HR-MAS) probe as shown in Figure 2.2. The details of how the HR-MAS probe obtains NMR measurements will be discussed with NMR instrumentation in subsection 3.4.1. The pickup coil consists of 1600 turns of AWG 36 wire on a 12 mm diameter former. The former is offset 20 mm above the center of the NMR sample, which rests in a 5 mm cylindrical tube within a stator at a fixed angle. This pickup coil is mounted from the top of 7.1 T superconducting magnet and from the bottom of the Keck powered magnet to allow space for other equipment in the magnet bore.

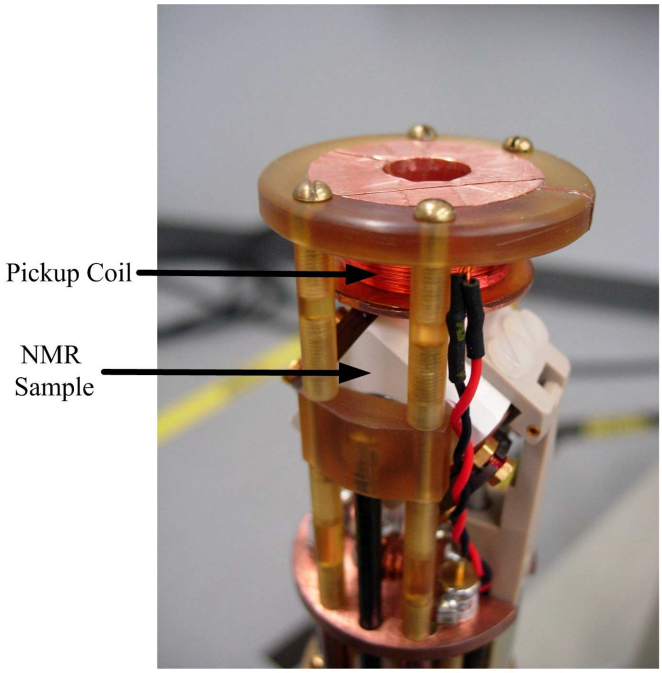

Figure 2.2. Photograph of the pickup coil used for inductive measurements of field fluctuations.

By Faraday's law, the open circuit pickup coil voltage is proportional to the derivative of the field fluctuations. An integrating preamplifier is used to integrate the pickup coil voltage providing a measurement proportional to field fluctuations. The integrating preamplifier in series with the pickup coil provides inductive measurements which are an estimate of the field fluctuations. It was mentioned previously that a pure integrator is undesirable as small DC offsets in analog instrumentation will saturate the integrator output. Instead, the integrating preamplifier was designed as a low pass filter with a -20 dB per decade slope and a very low cutoff frequency. The device is comprised of analog operational amplifiers, resistors, and capacitors to realize this low pass filter.

In order to demonstrate how inductive measurements are an estimate of field fluctuations, consider the following example with a sinusoidal field fluctuation

$$B_f(t) = B_{fo}\cos(\omega_f t). \tag{2.1}$$

The open circuit pickup coil voltage is the derivative of equation 2.1

$$v_{oc}(t) = -K_c B_{fo} \omega_f \sin(\omega_f t), \tag{2.2}$$

where the constant K_c is determined by the coil geometry. Observe that the amplitude of equation 2.2 scales with ω_f and B_{fo}. The integrating preamplifier is designed to eliminate the scaling factor ω_f to estimate the field fluctuation from $v_{oc}(t)$. The transfer function of the integrating preamplifier is modeled with a first order low pass filter

$$H_{int}(j\omega) = \frac{K}{j\omega\tau + 1}, \tag{2.3}$$

which for frequencies much greater than $1/\tau$, can be approximated as

$$H_{int}(j\omega) \approx \frac{K}{j\omega\tau}. \tag{2.4}$$

If the frequency of the field fluctuation, ω_f, is much greater than $1/\tau$, then the integrator transfer function in equation 2.4 is valid. In this case, when the pickup coil voltage in equation 2.2 is provided as the input, then the output of the integrating preamplifier will be the integration of the pickup coil voltage

$$v_{int}(t) = (K_c K B_{fo}/\tau) \cos(\omega_f t), \tag{2.5}$$

which is proportional to field fluctuations and has an amplitude independent of ω_f. The value of τ is known and can be used to identify the parameter $K_c K$ from experimental data. Section 2.3 shows a procedure for identifying model parameters such as $K_c K$ from experimental data.

If ω_f is less than $1/\tau$, then the integrating preamplifier behaves as a low pass filter with transfer function shown in equation 2.3. In this case the scaling factor ω_f is not completely eliminated from the pickup coil voltage input. The resulting integrating preamplifier output

$v_{int}(t)$ is no longer proportional to the field fluctuation. Furthermore, as ω_f gets small, the amplitude of $v_{int}(t)$ is reduced, decreasing the signal SNR. Section 1.4.2 demonstrated that low pass filtering effects and low frequency noise sources of the integrating preamplifier limit inductive measurements from accurately estimating lower frequency fluctuations.

2.2 Current Amplifier and Drive Coils

The current amplifier and drive coils serve two purposes in this work. The first purpose is to superimpose artificial field fluctuations, or disturbance fields, on the B_0 magnetic field to test design performance in presence of known field fluctuations. This is achieved with one channel of the current amplifier in series with the disturbance coil. The second purpose of these devices is to correct for field fluctuations with feedback control. When estimates of the field fluctuations are coupled to a chosen feedback compensator, the compensator must generate a correction field to reduce the field fluctuations. This is achieved with a second channel of the current amplifier in series with the correction coil.

The drive coil assembly, shown in Figure 2.3, consists of two coils wound one over another on a 44.28 mm diameter fiberglass tube. Both coils were wound using adhesive copper tape 0.125 inches wide and 0.001 inches thick and have identical characteristics. In order to distinguish between the two, we denote one as the disturbance coil and the other as the correction coil. The assembly is mounted from the top of both the superconducting and Keck magnets. Table 2.1 lists other specifications of the disturbance and correction coils.

Figure 2.3. Drive coil assembly, including disturbance and correction coils.

	Correction Coil (Disturbance Coil)
N[turns]	65
$L[\mu\text{H}]$	24.9
$R[\Omega]$	1.5
Wire Type	Copper Tape

Table 2.1. Specifications of the correction and disturbance coils.

The current amplifier is a wide-bandwidth pulsed gradient amplifier from Resonance Research, Inc.(RRI). This amplifier has three identical channels. The gain of the amplifier is 2 A/V, meaning a voltage at the input of the amplifier produces a current output that is twice the voltage input. The maximum continuous current the amplifier can source is a 3.5 A, which corresponds to a 1.75 V input.

The voltage input of the current amplifier produces a current output, which is supplied to a drive coil, producing a magnetic field which is superimposed on the B_0 field of the magnet. The gain from current amplifier voltage input to drive coil field output at the NMR sample is 4.33 G/V. The details of this gain measurement are left to Section 2.3 discussing model identification.

At the peak 1.75 V input, the current amplifier and correction coil produces a maximum 7.5 G field at the NMR sample. For the cascade feedback control system, the correction field was limited to 7 G to prevent the compensators from driving maximum current. Recall from Section 1.2 that the largest amplitude of the higher frequency fluctuations due to power supply ripple in the Keck was 0.16 G rms at 60 Hz. This implies that the inductive feedback control loop can cancel higher frequency fluctuations using the current amplifier and correction coil as it produces a maximum field much larger than 0.16 G. Additionally, it will be shown in Chapter 6 that field fluctuations due to cooling water variations are 5 G peak to peak when implementing inductive feedback control. This implies that a direct FFL control loop in cascade with an inductive feedback control loop can cancel lower frequency fluctuations using the current amplifier and correction coil because 7 G is larger than 5 G.

In addition to the maximum correction field, the minimum correction field is defined by the amplifier and correction coil as well as the digital to analog converters (DAC) of the cascade feedback system. The DACs are realized as 16 bit converters with a 20 V full scale range using a digital signal processor. These 16 bit DACs are used to convert the sampled-data correction signal from the compensators to an analog signal for the amplifier and correction coil. The minimum quantization voltage of this DAC is $20/2^{16}$ or 0.3 mV, which is implies the minimum correction field of the compensators is 0.3 mV $\times$ 4.33 G/V or 1.3 mG.

The previous two sections discussed the instrumentation used for inductive measurements and correcting field fluctuations. For the feedback control system design shown in Chapter 6, analytical models of these devices were necessary to predict the performance of the compensator design. The following section presents the procedure for identifying analytical models for the pickup coil and integrating preamplifier as well as the amplifier and correction coil.

2.3 Model Identification

The pickup coil, integrating preamplifier, current amplifier, and correction coil are represented by continuous-time transfer functions because they are analog devices. Consider the updated block diagram of the cascade feedback control system in Figure 2.4, where $H(s)$ has replaced the pickup coil and integrating preamplifier, and $G_a(s)$ has replaced the current amplifier and correction coil. The objective of this section is to identify the continuous-time transfer functions $H(s)$ and $G_a(s)$ that model these devices in the experimental system.

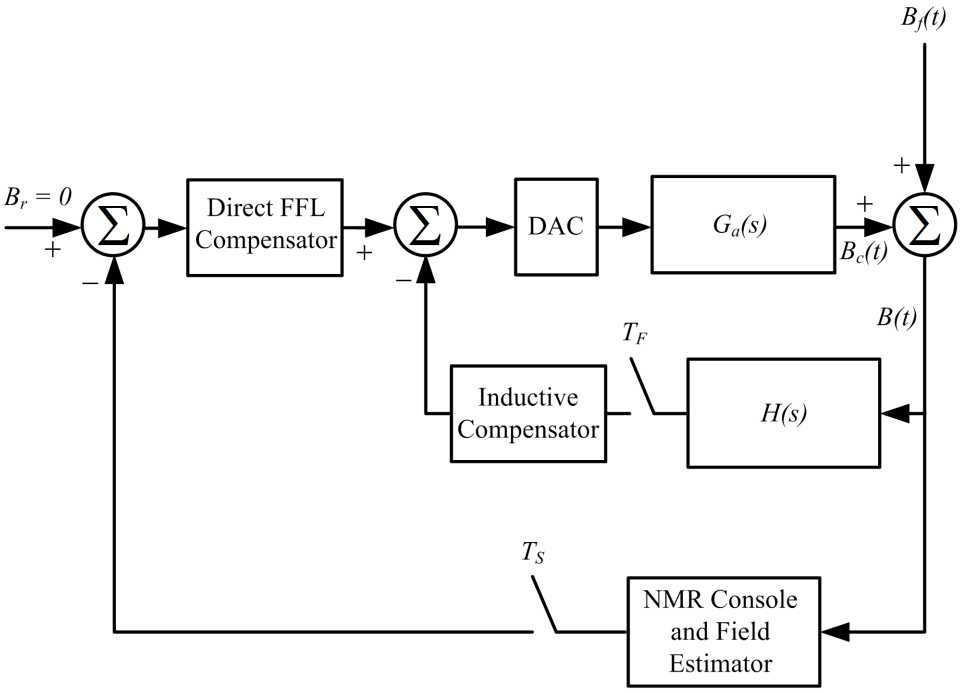

Figure 2.4. Cascade feedback control system with transfer function models $H(s)$, $G_a(s)$ for the inductive feedback control loop.

An analytical expression for $H(s)$ is derived first which will used to identify models from experimental data. The expression for the transfer function $H(s)$ is derived from the open circuit pickup coil voltage and integrating preamplifier transfer function. The open circuit pickup coil voltage is proportional to the derivative of the field fluctuations

$$v_{oc}(t) = K_c \frac{dB_f(t)}{dt}, \tag{2.6}$$

where the constant K_c is determined by the coil geometry. The Laplace transform of equation 2.6 is

$$V_{oc}(s) = K_c s B_f(s), \tag{2.7}$$

and the transfer function of the pickup coil from field fluctuations to open circuit voltage $H_p(s)$ is

$$H_p(s) = \frac{V_{oc}(s)}{B_f(s)} = K_c s. \tag{2.8}$$

The Fourier transform of the integrating preamplifier was defined in equation 2.3. By replacing $j\omega$ with s in this expression, the transfer function of the integrating preamplifier becomes

$$H_{int}(s) = \frac{V_{int}(s)}{V_{oc}(s)} = \frac{K}{s\tau + 1}, \tag{2.9}$$

where K is the DC gain of the integrating preamplifier and τ is the time constant. The cascade combination of $H_p(s)$ and $H_{int}(s)$ gives the expression for $H(s)$

$$H(s) = H_p(s) H_{int}(s) = \frac{K_c K s}{s\tau + 1}. \tag{2.10}$$

The loop transfer function $L(s)$ is used to identify models of $H(s)$ and $G_a(s)$ from experimental

data, and is defined as the cascade combination of $H(s)$ and $G_a(s)$

$$L(s) = H(s)G_a(s) = \frac{K_c K s}{s\tau + 1} G_a(s). \tag{2.11}$$

As $G_a(s)$ is a current amplifier and correction coil, the magnitude of this device is expected to be constant for low frequencies and get smaller at high frequencies. This implies that $G_a(s)$ will have high frequency poles and zeros thereby determining the upper cutoff frequency of $L(s)$. Additionally, observe from equation 2.11 that $L(s)$ has a pole when s is $-1/\tau$ and a zero at the origin when s is zero. Thus the lower cutoff frequency of $L(s)$ is $1/\tau$, and increasing τ reduces the lower cutoff frequency.

The time constant τ is a known parameter computed from resistors and capacitors of the integrating preamplifier circuit. In the earlier work by Li *et al.*, τ was set to 3 seconds. In this study, the value of τ was increased to 20 seconds, reducing the lower cutoff frequency of $L(s)$ from 0.33 rad/s (0.05 Hz) to 0.05 rad/s (0.008 Hz). Further increases in τ are not practical because it requires larger capacitors, and even if these capacitors were installed the inductive measurement will have poor SNR at low frequencies due to 1/f noise.

With τ known, equation 2.11 will now be used to identify the parameter $K_c K$ and the transfer function $G_a(s)$ to completely characterize $H(s)$ and $G_a(s)$. For frequencies above $1/\tau$ equation 2.11 is approximated as

$$L(s) \approx \frac{K_c K}{\tau} G_a(s). \tag{2.12}$$

The expression for the approximate $L(s)$ in equation 2.12 can be determined from experimental measurements of the loop transfer function.

The frequency response of the loop transfer function was measured using an Agilent Dynamic Signal Analyzer (DSA) on the Keck powered magnet at zero field. Figure 2.5 shows the setup for this frequency response measurement experiment. The DSA is connected between the integrating preamplifier output and the current amplifier input. The DSA has a output channel called the

source and two inputs denoted channel one and channel two. The output channel provides a sinusoidal excitation for the system identification experiment, and is connected to the input of the current amplifier as well as the channel one of the DSA.

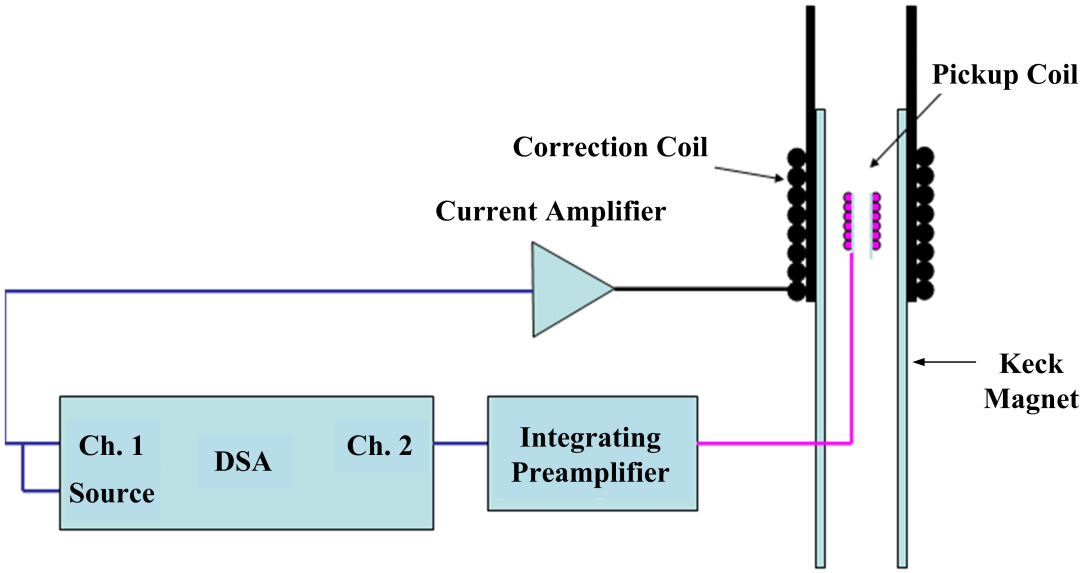

Figure 2.5. Experimental setup for measuring the loop transfer function on the Keck [27].

The DSA source channel generates a sinusoidal signal whose frequency is swept over a specified range. The DSA automatically adjusts the excitation amplitude of the sinusoid signal to maintain a good measurement SNR. This signal goes into channel one of the DSA and the current amplifier. The sinusoidal signal from the DSA is amplified by the current amplifier and fed into the correction coil to produce an additional magnetic field in the bore of the Keck powered magnet. This oscillating magnetic field induces a voltage in the pickup coil that is connected to the integrating preamplifier.

After integration, the sinusoidal output voltage of the integrating preamplifier is fed into channel two of the DSA. The DSA compares the signals on channel one and channel two to obtain the frequency response measurement of the loop transfer function. For this measurement, 659 data points were acquired over the frequencies 0.1 to 5 kHz. The 5 kHz upper limit was chosen because the inductive compensator will not be designed to attenuate field fluctuations

above 5 kHz. This is because fluctuations above 5 kHz do not have significant effects on NMR which will be discussed in Section 3.3.

Observe that the 0.1 Hz low frequency limit of the DSA is much greater than the pole of $H(s)$ at 0.008 Hz. Therefore loop transfer function data obtained with the DSA does not capture the low frequency characteristics of $L(s)$. Thus the loop transfer function data collected in this experiment can only be used to identify the approximate $L(s)$ in equation 2.12 which is valid for higher frequencies.

The approximate loop transfer function in equation 2.12 was derived from loop transfer function data using the complex-curve fitting algorithm [64] implemented using the Matlab function *invfreqs*. Given the number of poles and zeros, this algorithm estimates a transfer function which minimizes the least-squared error between the estimated transfer function and the true frequency response data. By iterating the number of poles and zeros, it was found that two poles and no zeros gave the smallest error between the estimated transfer function and the frequency response data. The resulting estimated loop transfer function is

$$L(s) \approx \frac{4.344e8}{(s+1.035e005)(s+2.094e004)}. \tag{2.13}$$

In comparing equations 2.12 and 2.13, the poles of $G_a(s)$ are the poles of equation 2.13. Recall from Section 2.2 that the DC gain of $G_a(s)$ was measured as 4.33 G/V. Therefore the transfer function of $G_a(s)$ is

$$G_a(s) = \frac{4.33}{(\frac{s}{1.035e005}+1)(\frac{s}{2.094e004}+1)}. \tag{2.14}$$

From the approximate expression of $L(s)$ in equation 2.12, the parameter K_cK is determined by dividing $L(s)$ and $G_a(s)$ and scaling the result by τ

$$K_cK = \frac{L(s)}{G_a(s)}\tau = 0.9257. \tag{2.15}$$

With this parameter identified, and the known 20 second time constant, the transfer function for $H(s)$ can now be written as

$$H(s) = \frac{0.9257s}{s20 + 1}. \tag{2.16}$$

The complete loop transfer function, with no approximations, is the product of equations 2.14 and 2.16

$$L(s) = \frac{0.9257s}{s20 + 1} \frac{4.33}{(\frac{s}{1.035e005} + 1)(\frac{s}{2.094e004} + 1)}. \tag{2.17}$$

The transfer function in equation 2.17 was verified by comparing the frequency response of $L(s)$ to the experimental loop transfer function data collected. Figure 2.6 compares the frequency response from experimental data to the frequency response of the identified $L(s)$ in equation 2.17. The frequency response of $L(s)$ matches the experimental data well, and the 3 dB bandwidth of $L(s)$ is approximately 3204 Hz. The lower cutoff frequency afforded by improvements in τ is now 0.008 Hz.

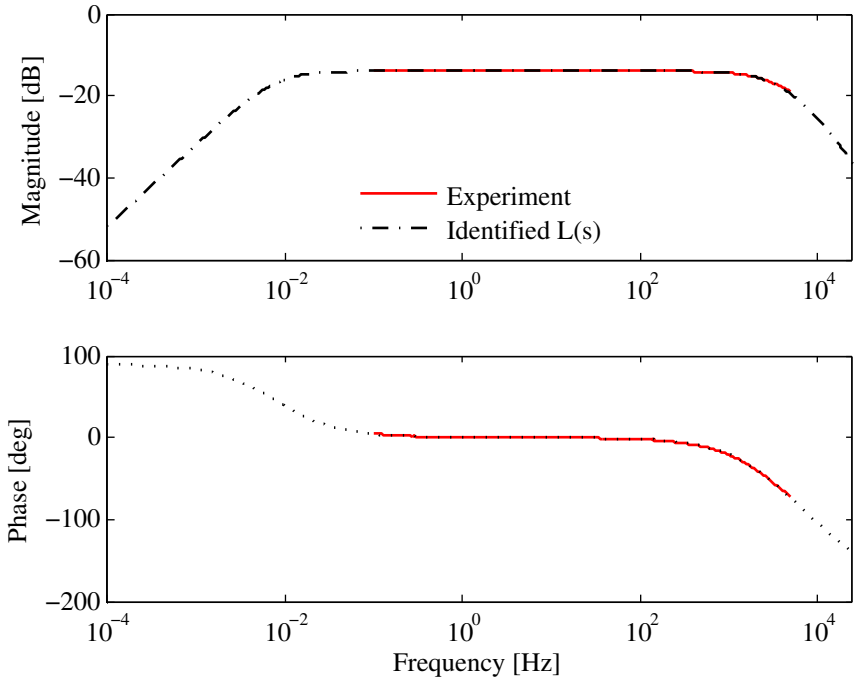

Figure 2.6. Transfer function $L(s)$ identified from measured frequency response of loop transfer function for the Keck operating at zero field.

Recall that the experimental data in Figure 2.6 was measured at zero field. This was done primarily to save operating costs of the Keck and to avoid having noisy data measurements when identifying transfer function models. Figure 2.7 shows the same loop transfer function measurements as in Figure 2.6 only with the Keck operating at 7.1 T and 25 T. To reduce experiment time and hence save operating cost, the lower frequency limit of this data was chosen as 5 Hz instead of 0.1 Hz. The maximum 800 points of data were acquired for the frequency range 5 Hz to 51.2 kHz.

When comparing the experimental results in Figures 2.6 and 2.7, the measurements have more noise when there is field present. Also, observe that just below 30 kHz there appears to be a high frequency mode when the magnet operates at 7.1 T and 25 T. As the field is increased from 7.1 T to 25 T, the magnitude of this mode becomes more pronounced. This mode was ignored when designing the inductive compensator to simplify the design, and Chapter 6 shows experimental results that a validate this assumption. However, future designs may have to account for this mode whose origin is currently unknown.

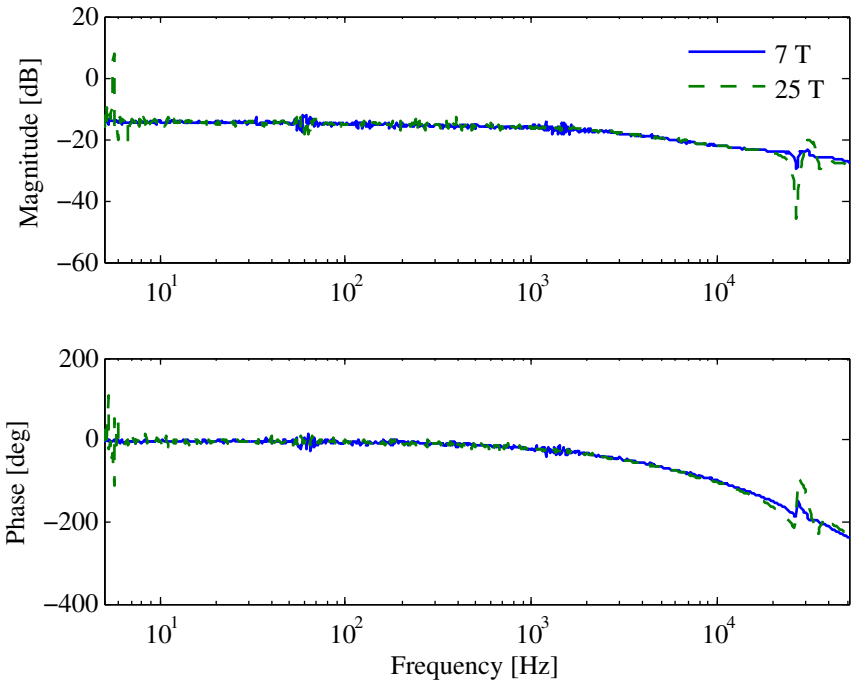

Figure 2.7. Measured frequency response of loop transfer function for Keck powered magnet operating at 7.1 T and 25 T.

The identified transfer functions $G_a(s)$ and $H(s)$ in equations 2.14 and 2.16 will be used in Chapter 6 when designing compensators for the cascade feedback control system. The following Chapter provides an introduction to NMR physics along with the instrumentation used to measure the NMR signal. The free-induction decay (FID) introduced in Chapter 1 is a particular NMR signal which will be discussed in detail.

Chapter 3

NMR Physics and Instrumentation

In order to understand how NMR can be used to estimate and reduce lower frequency field fluctuations, it is necessary to have some insight to NMR physics. Specifically, the NMR signal known as the free induction decay (FID) was used to estimate lower frequency field fluctuations as well as compute the NMR performance metrics mentioned in Chapter 1.

This chapter discusses NMR physics, providing specific discussion of FID signals, and the instrumentation used to generate and measure these signals in the laboratory. Section 3.1 discusses the vector representation of NMR physics in the presence of a B_0 field. Section 3.2 discusses the origin of the FID signal and its spectral characteristics. Section 3.3 discusses the effect of field fluctuations on the FID signal and its spectrum. Section 3.4 discusses the NMR instrumentation used to experimentally measure FID signals.

3.1 Vector Representation

The analysis of the NMR response in this dissertation uses the vector representation of the NMR signal and is not meant to be a complete treatment of the subject. Refer to text by Slichter [65] and Abragam [66] for a complete discussion of NMR physics.

Nuclear magnetic resonance (NMR) is a tool for determining chemical structure of a sample and relies on interactions between magnetic fields and magnetic moments of nuclei. Consider a hydrogen nucleus containing a single proton. This nucleus possesses an angular momentum producing a small magnetic field or magnetic moment. The angular momentum and magnetic moment are represented by the vectors $\vec{J}$ and $\vec{\mu}$ respectively, and the relationship between these vectors is

$$\vec{\mu} = \gamma \vec{J}, \tag{3.1}$$

where γ is the gyromagnetic ratio of the hydrogen nucleus.

In the presence of an external static magnetic field B_0, the magnetic moment of the nucleus aligns in a direction parallel or anti-parallel to the B_0 direction as indicated in Figure 3.1. The B_0 field is in the z direction, and the nucleus is represented by the small oval. The magnetic moment $\vec{\mu}$ of the nucleus has a fixed angle α with respect to the B_0 field direction. From quantum mechanics, the fixed angle α for a single proton in a hydrogen nucleus is approximately 54.7°. If the magnetic moment has a component parallel to B_0 in the positive z direction, then it is in the parallel state. Conversely a magnetic moment in the anti-parallel state has a component in the opposite direction of B_0.

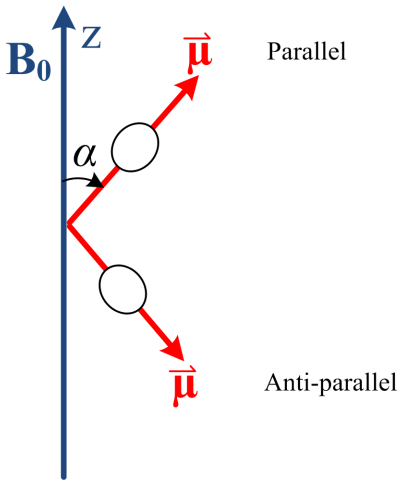

Figure 3.1. Magnetic moment alignment in presence of static external magnetic field B_0.

The B_0 field also interacts with the magnetic moment $\vec{\mu}$ to produce a torque $\vec{N}$ defined by

$$\vec{N} = \vec{\mu} \times B_0 \hat{z}. \tag{3.2}$$

The $\hat{z}$ is a unit vector in the positive z axis, which is the direction of B_0. The torque acting on the nucleus changes its angular momentum

$$\vec{N} = \frac{d\vec{J}}{dt} = \vec{\mu} \times B_0 \hat{z}. \tag{3.3}$$

Substituting equation 3.1 into 3.3 gives a differential equation for $\vec{\mu}$

$$\frac{d\vec{\mu}}{dt} = \gamma \vec{\mu} \times B_0 \hat{z}, \tag{3.4}$$

which reveals that $\vec{\mu}$ precesses about B_0 at the Larmor frequency γB_0.

A NMR sample contains a large number of nuclei, and the superposition of the magnetic moments for each nuclei results in a bulk magnetization, represented by the vector $\vec{M}$, which satisfies equation 3.4 with $\vec{\mu}$ replaced by $\vec{M}$

$$\frac{d\vec{M}}{dt} = \gamma \vec{M} \times B_0 \hat{z}. \tag{3.5}$$

When B_0 is switched on, the z component of the magnetization vector exponentially approaches a thermal equilibrium value M_0 with a time constant defined as the spin-lattice relaxation time T_1. This feature is represented by adding a T_1 term to equation 3.5

$$\frac{d\vec{M}}{dt} = \gamma \vec{M} \times B_0 \hat{z} - \frac{(M_z - M_0)\hat{z}}{T_1}, \tag{3.6}$$

where M_z is the z component of $\vec{M}$.

Coupling between the magnetic moments of adjacent nuclei results in a variation of precession frequencies of the magnetic moments in the NMR sample. Denote the $x-y$ plane as the transverse plane perpendicular to the direction of B_0. The variation in magnetic moment precession frequencies causes the magnetization components in the $x-y$ plane to vanish due to destructive interference. The spin-spin relaxation time constant T_2 describes the rate at which the magnetization vanishes in the $x-y$ plane. This process is represented by adding a T_2 term to equation 3.5

$$\frac{d\vec{M}}{dt} = \gamma\vec{M} \times B_0\hat{z} - \frac{M_x\hat{x} + M_y\hat{y}}{T_2}, \tag{3.7}$$

where M_x and M_y are the x and y components of $\vec{M}$.

Combining the spin-lattice and spin-spin relaxation processes leads to the expression

$$\frac{d\vec{M}}{dt} = \gamma\vec{M} \times B_0\hat{z} - \frac{M_x\hat{x} + M_y\hat{y}}{T_2} - \frac{(M_z - M_0)\hat{z}}{T_1}, \tag{3.8}$$

which is the well known Bloch equation with external field $B_0\hat{z}$ [3]. The general Bloch equation models the response of the bulk magnetization $\vec{M}$ to an external field. For equation 3.8, the external field is $B_0\hat{z}$. The time constant T_1 governs how fast the magnetization vector relaxes back to thermal equilibrium on the z axis, and T_2 governs how fast $M_x\hat{x} + M_y\hat{y}$ decays to zero. The time constant T_1 is much larger than T_2.

Up to this point, the magnetization vector has been discussed with respect to the laboratory $x-y-z$ coordinate frame. It is convenient to view the magnetization vector $\vec{M}$ in a rotating $u-v-z$ coordinate frame. The laboratory and rotating frame share the same z axis. In the rotating frame, the $u-v$ plane rotates about the z axis at the Larmor frequency γB_0. Therefore if $\vec{M}$ is precessing about the z axis in the $x-y-z$ frame, then it remains stationary in the rotating $u-v-z$ frame as demonstrated in Figure 3.2. The rotating reference frame will be used when discussing the magnetization vector for the remainder of this dissertation.

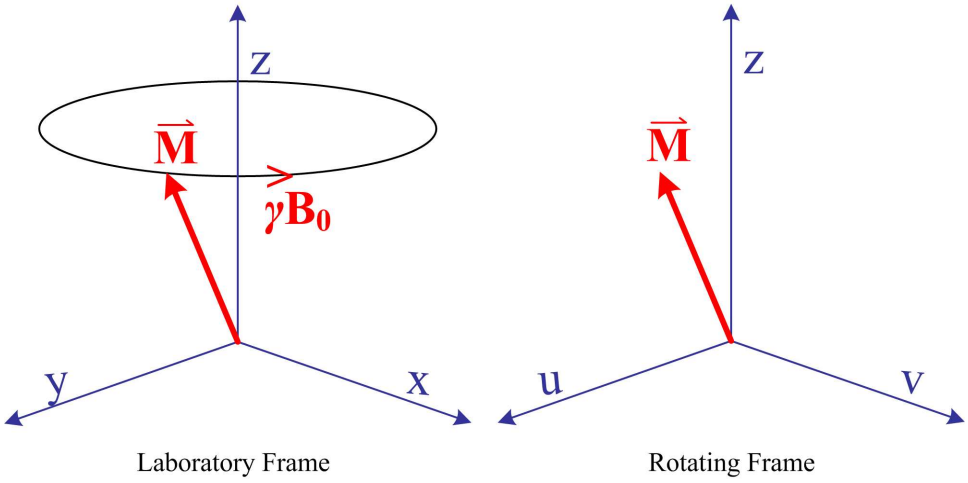

Figure 3.2. Magnetization vector in the laboratory and rotating reference frame.

The NMR signal known as a free induction decay (FID) will be used to estimate lower frequency field fluctuations as well as compute the NMR performance metrics from Chapter 1.2. The following section describes the FID signal and its mathematical representation as a complex signal. This representation is then be used to study spectral characteristics of the FID signal.

3.2 Free-Induction Decay

The free-induction decay (FID) is a common signal measured in NMR spectroscopy and it used throughout this dissertation. Chapter 5 develops methods for estimating field fluctuations from FID signals, and Chapter 6 shows performance metrics derived from FID signal measurements. Therefore it is useful to describe the origin and a mathematical representation of FID signals as it will be used often in this dissertation.

In any NMR experiment, the magnetization vector $\vec{M}$ is tipped away from the z axis with an applied magnetic field $\vec{B}_1$ in a direction perpendicular to the z axis. The applied $\vec{B}_1$ field is generated by an RF pulse applied to an RF coil oriented in the $x-y$ plane. The frequency of the RF pulse is chosen as the Larmor frequency γB_0, resulting in a $\vec{B}_1$ field in the $x-y$ plane which rotates about the z axis at frequency γB_0. In the rotating $u-v$ plane, $\vec{B}_1$ is stationary.

The response of the magnetization vector $\vec{M}$ to the magnetic field $\vec{B}_1$ in the -v direction is illustrated in Figure 3.3. Before application of $\vec{B}_1$, $\vec{M}$ lies completely on the z axis in thermal equilibrium with a value $M_0\hat{z}$. In the rotating frame, the effective field along the z axis is zero, so the magnetization vector responds only to the $\vec{B}_1$ field. The cross product term of the Bloch equations indicate that the $\vec{B}_1$ field tips the vector $\vec{M}$ away from the z axis. Upon application of $\vec{B}_1$, the magnetization vector is tipped an angle θ from the z axis in the $z-u$ plane. The expression for tip angle is

$$\theta = \gamma B_1 t_w, \tag{3.9}$$

where t_w is the RF pulse width in seconds and B_1 is the magnitude of the vector $\vec{B}_1$. The transverse magnetization $\vec{M}_{uv}$ is the projection of $\vec{M}$ onto the $u-v$ plane, which lies completely on the u axis in this case.

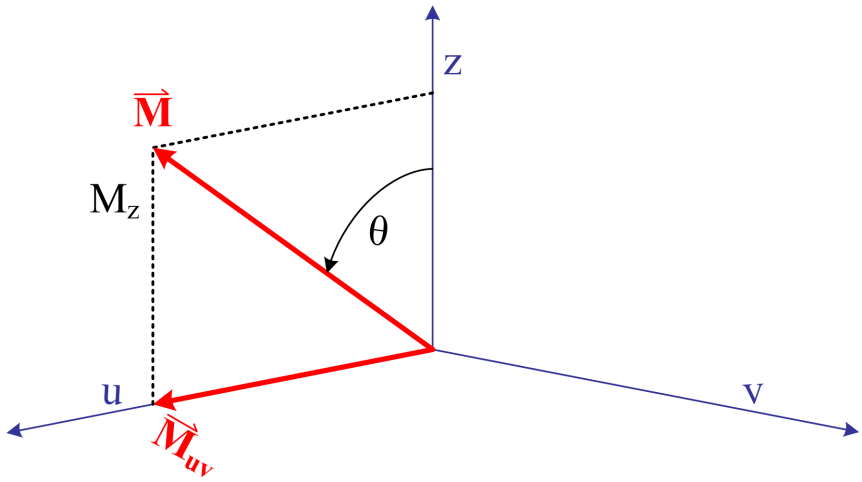

Figure 3.3. Magnetization vector response to applied magnetic field $\vec{B}_1$ in the -v direction.

A FID signal represents the transverse magnetization $\vec{M}_{uv}$ in response to a particular type of applied $\vec{B}_1$ field. In this case the RF pulse is chosen such that the $\vec{B}_1$ field tips $\vec{M}$ by an angle close to $\pi/2$. From equation 3.9, such a tip angle is achieved using either the field magnitude B_1 or pulse width time t_w. When the RF pulse is removed, a signal representing $\vec{M}_{uv}$ is detected with an RF coil in the $u-v$. This signal, denoted as $M_{uv}(t)$, is obtained as a function of time and

resolved into u and v components $M_u(t)$ and $M_v(t)$ with phase sensitive detection. The details of how $M_{uv}(t)$ is measured and resolved into these components is discussed with instrumentation in Section 3.4.

It was mentioned in Chapter 1.1 that powered magnets have spatial field inhomogeneities in the magnetic field strength B_0. In this case, additional time constants T_2^* and T_2' must be considered for the decay of the transverse magnetization $M_{uv}(t)$. The expression relating these time constants to spin-spin relaxation T_2 is

$$\frac{1}{T_2^*} = \frac{1}{T_2} + \frac{1}{T_2'}, \tag{3.10}$$

where T_2' is the decay time constant due to spatial field inhomogeneities. Note that in the presence of field inhomogeneities, $1/T_2^*$ is greater than $1/T_2$. This implies $M_{uv}(t)$ decays to zero faster when T_2^* must be considered due to field inhomogeneity, which is undesirable for NMR. For the remainder of this dissertation, T_2^* will be considered as the transverse decay time constant because the objective is to demonstrate a feedback control system on the Keck powered magnet where field inhomogeneities exist.

The complex signal representation of the FID signal in response to a single RF pulse is

$$\begin{aligned} M_{uv}(t) &= M_u(t) + jM_v(t) \\ &= Ae^{-t/T_2^*}e^{j\phi(t)}, \end{aligned} \tag{3.11}$$

where the amplitude of the FID is denoted by A and j represents the imaginary unit $\sqrt{-1}$. The angle $\phi(t)$ is the phase angle between $\vec{M}_{uv}$ and the u axis. For the response shown in Figure 3.3, the phase angle $\phi(t)$ is zero. Situations where $\phi(t)$ is non-zero will be discussed in Sections 3.3 and 3.4.

When $\phi(t)$ is zero, the complex signal representation of the FID with amplitude A equal to one simplifies to

$$M_{uv}(t) = e^{-t/T_2^*}, \tag{3.12}$$

The Fourier transform of equation 3.12 is

$$\begin{aligned} M_{uv}(\omega) &= \frac{1}{j\omega + 1/T_2^*} \\ &= \frac{T_2^*}{j\omega T_2^* + 1}, \end{aligned} \tag{3.13}$$

where the magnitude of this expression represents the magnitude spectra of the FID. The linewidth is defined from the squared magnitude spectra of equation 3.13

$$|M_{uv}(\omega)|^2 = \frac{(T_2^*)^2}{(\omega T_2^*)^2 + 1}. \tag{3.14}$$

Observe from equation 3.14 that the maximum of the squared magnitude spectra occurs when ω is zero with a value of $(T_2^*)^2$. Additionally, half the maximum of squared magnitude spectra, $(T_2^*)^2/2$, occurs when ω is plus or minus $1/T_2^*$. The linewidth is computed as the difference of these two frequencies, which is $2/T_2^*$ rad/s or $1/(\pi T_2^*)$ Hz.

Figure 3.4 shows a normalized FID squared magnitude spectra plotted using equation 3.14. The time constant T_2^* was chosen as 3.2 ms which corresponds to the 100 Hz linewidth desirable for NMR. The horizontal axis shows frequency normalized by linewidth (LW), and the vertical axis shows $|M_{uv}(\omega)|^2$ normalized by T_2^*. Observe that when frequency is plus or minus one half the linewidth, $|M_{uv}(\omega)|^2$ is half its maximum magnitude. Also, the shape of $|M_{uv}(\omega)|^2$ is symmetric about the vertical axis.

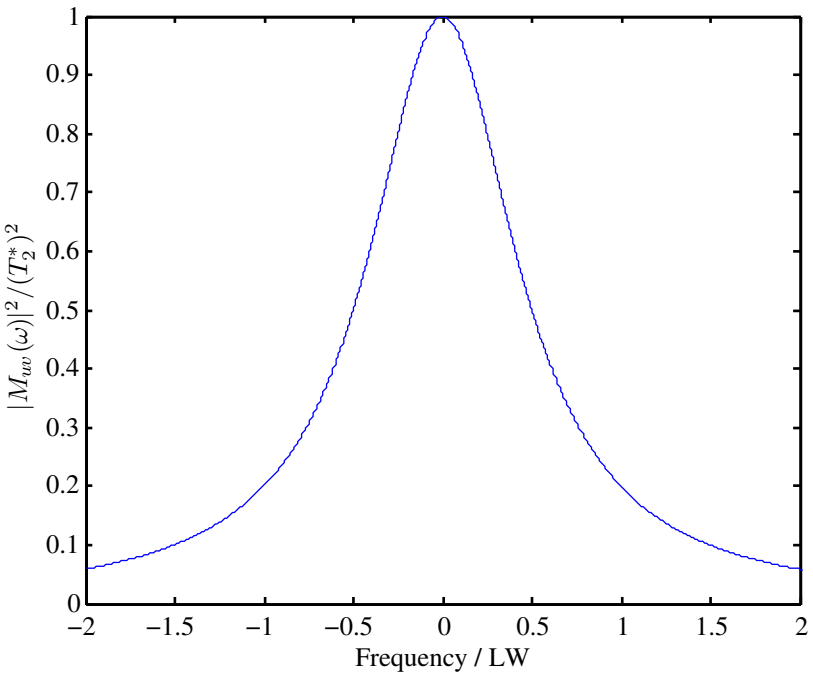

Figure 3.4. Normalized squared magnitude of FID spectra with 100 Hz linewidth.

The following section discusses the effect of temporal field fluctuations on an FID. These effects are discussed using both the vector representation $\vec{M}$ and complex signal representation $M_{uv}(t)$ of an FID. The complex signal representation will be used to analyze how these fluctuations affect the FID magnitude spectra. These effects are useful when considering a feedback control design in Chapter 6.

3.3 Effect of Temporal Field Fluctuations on the Free-Induction Decay

The response of the magnetization vector shown in Figure 3.3 assumes there are no temporal field fluctuations in the magnetic field. Figure 3.5 depicts the magnetization vector response when temporal field fluctuations $B_f(t)$ are present in the -z direction. In this case, the magnetization vector $\vec{M}$ precesses about the direction of the field fluctuations, and the transverse magnetization

$\vec{M}_{uv}$ sweeps out a phase angle $\phi(t)$. The vector $\vec{M}_{uv}$ rotates at a frequency $\omega_f(t)$ which is $\gamma B_f(t)$. The expression for the phase angle can be found by taking the integral of the frequency $\omega_f(t)$

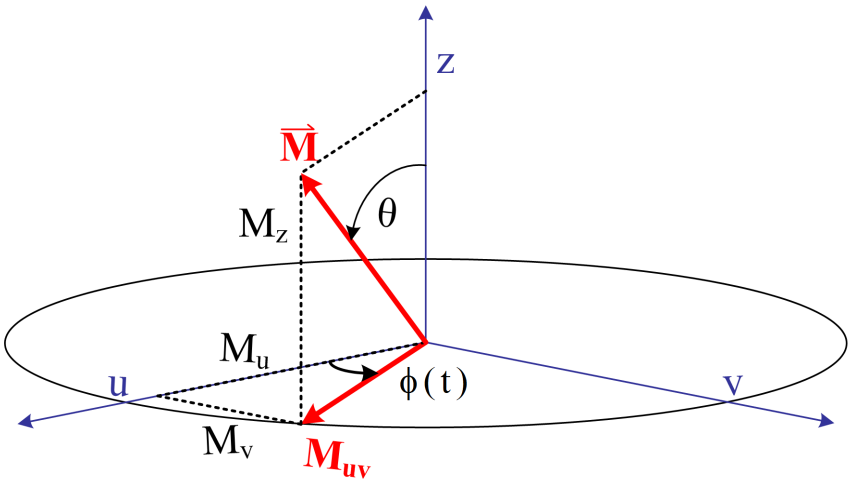

Figure 3.5. Diagram of magnetization vector when temporal field fluctuations $B_f(t)$ are present in the -z direction.

$$\phi(t) = \int_0^t \omega_f(\tau)d\tau = \int_0^t \gamma B_f(\tau)d\tau. \tag{3.15}$$

Recall from Section 1.2 that a constant 0.16 Gauss field fluctuation shifted the Larmor frequency of hydrogen nuclei by 681 Hz. The effect of time varying sinusoidal fluctuations on the complex signal representation $M_{uv}(t)$ and its magnitude spectra will now be analyzed. Consider a field fluctuation of the form

$$B_f(t) = B_{fo}\cos(\omega_f t), \tag{3.16}$$

where B_{fo} and ω_f is the amplitude and frequency of the field fluctuation respectively. In this case the phase angle in equation 3.15 becomes

$$\phi(t) = \int_0^t \gamma B_{fo}\cos(\omega_f\tau)d\tau = \left(\frac{\gamma B_{fo}}{\omega_f}\right)\sin(\omega_f t). \tag{3.17}$$

The complex signal representation of the FID in the presence of this fluctuation is denoted as

$\tilde{M}_{uv}(t)$, and can be written in terms of the FID signal with no fluctuations present $M_{uv}(t)$

$$\begin{aligned}\tilde{M}_{uv}(t) &= e^{-t/T_2^*} e^{j\phi(t)} \\ &= e^{-t/T_2^*} e^{j\left(\frac{\gamma B_{fo}}{\omega_f}\right)\sin(\omega_f t)} \\ &= M_{uv}(t) e^{j\left(\frac{\gamma B_{fo}}{\omega_f}\right)\sin(\omega_f t)}. \end{aligned} \tag{3.18}$$

It is desirable to determine magnitude spectra of this expression by computing its Fourier transform. The expression in equation 3.18 is similar to an angle modulation expression often encountered in communication systems [68]. The challenging term here is the complex exponential with a sinusoid argument. In communication systems, the analysis is simplified by using the Fourier series representation of this exponential term. The same approach can be used here, where the Fourier series representation of this exponential is

$$e^{j\left(\frac{\gamma B_{fo}}{\omega_f}\right)\sin(\omega_f t)} = \sum_{n=-\infty}^{n=\infty} J_n\left(\frac{\gamma B_{fo}}{\omega_f}\right) e^{jn\omega_f t}, \tag{3.19}$$

where n is an integer, and $J_n(\cdot)$ is the n^{th} order Bessel function of the first kind with constant argument $\gamma B_{fo}/\omega_f$.

Substituting equation 3.19 into equation 3.18 gives

$$\begin{aligned}\tilde{M}_{uv}(t) &= M_{uv}(t) \sum_{n=-\infty}^{n=\infty} J_n\left(\frac{\gamma B_{fo}}{\omega_f}\right) e^{jn\omega_f t} \\ &= \sum_{n=-\infty}^{n=\infty} J_n\left(\frac{\gamma B_{fo}}{\omega_f}\right) M_{uv}(t) e^{jn\omega_f t}, \end{aligned} \tag{3.20}$$

and the Fourier transform of equation 3.20 is

$$\tilde{M}_{uv}(\omega) = \sum_{n=-\infty}^{n=\infty} J_n\left(\frac{\gamma B_{fo}}{\omega_f}\right) M_{uv}(\omega - n\omega_f). \tag{3.21}$$

By substituting equation 3.13, shifted by $n\omega_f$, into equation 3.21, the Fourier transform of $\tilde{M}_{uv}(t)$ can be expressed as

$$\tilde{M}_{uv}(\omega) = \sum_{n=-\infty}^{n=\infty} J_n\left(\frac{\gamma B_{fo}}{\omega_f}\right) \frac{T_2^*}{j(\omega - n\omega_f)T_2^* + 1}. \tag{3.22}$$

Observe from equation 3.22 that the argument of the Bessel function is inversely proportional to ω_f. As ω_f gets large, the Bessel function argument approaches zero, and $J_1(\cdot)$ approaches unity while $J_n(\cdot)$ approaches zero for all other n. Therefore as ω_f increases the effect of field fluctuations on the FID spectra is diminished. In general higher frequency fluctuations above several kHz do not affect NMR spectroscopy, a fact that will be exploited when designing the cascade feedback control system in Chapter 6

Equation 3.22 was used to study the effect of temporal field fluctuations on the FID magnitude spectra. Let β be defined as the argument of the Bessel function $\gamma B_{fo}/\omega_f$. For this study, the FID magnitude spectra was computed using equation 3.22 for β equal 1, 2, and 5. This allows one to study how fluctuations affect the FID spectra when B_{fo} increases with respect to ω_f. The gyromagnetic ratio γ was chosen as the value for hydrogen nuclei, and the time constant T_2^* was chosen as 3.2 ms which corresponds to a 100 Hz linewidth with no field fluctuations. The frequency ω_f was fixed at $2\pi 60$ and the amplitude B_{fo} was varied so that β was 1, 2, and 5. For these values of β, the Bessel function is negligible for orders above 20, allowing the summation in Equation 3.22 to be approximated with n between -20 and 20. The FID magnitude spectra and resulting linewidth was computed for each value of β.

The results of this study is shown in Figure 3.6. The horizontal axis shows frequency normalized by linewidth (LW), and the vertical axis shows squared magnitude of FID spectra normalized by $(T_2^*)^2$. The solid line represents the case where there are no field fluctuations, which is the same magnitude spectra shown in Figure 3.4. The other line types represent the cases where field fluctuations are present with β equal to 1, 2, and 5. In comparison to the case with no

fluctuations, the magnitude spectra is no longer symmetric and the linewidth is broadened as β increases. This implies that if the fluctuation amplitude increases or its frequency decreases, then the FID spectra is adversely affected. Table 3.1 shows the numerical values of linewidth for several values β. For the 60 Hz field fluctuation observed experimentally, B_{fo} is 0.16 G and ω_f is $2\pi 60$. This corresponds to a β of 1.81 which results in a 190 Hz linewidth, slightly less than when β is 2.

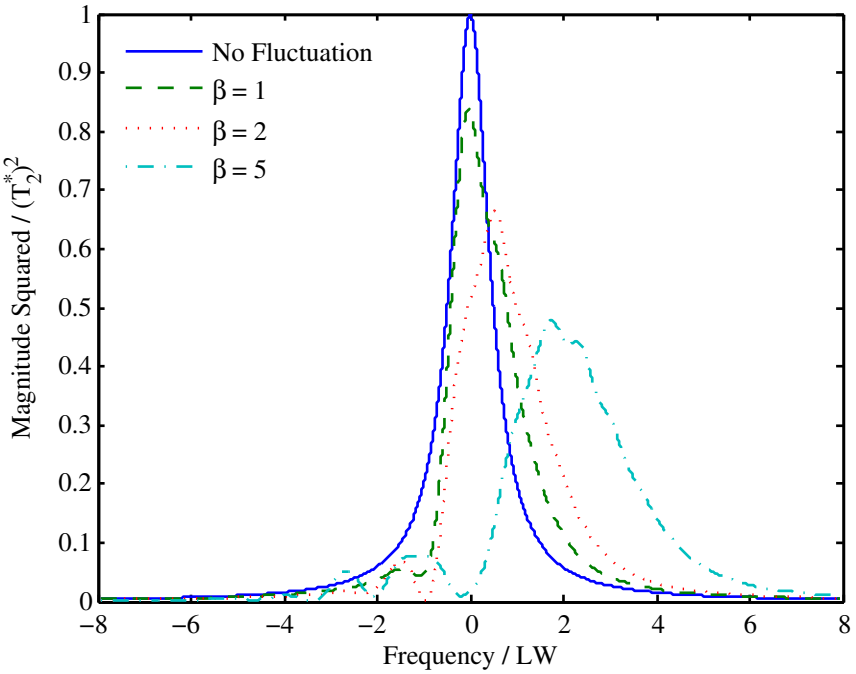

Figure 3.6. Normalized squared magnitude of FID spectra for different cases of temporal field fluctuations.

β	Linewidth [Hz]
1	140
2	192
5	256
10	322

Table 3.1. Linewidth for different values of β.

The results shown in this section demonstrate that temporal field fluctuations adversely affect both the FID spectra lineshape and linewidth. Chapter 6 demonstrates that the cascade feedback

control system improves the linewidth of the FID spectra. In the following section, the NMR instrumentation used to measure NMR signals will be discussed.

3.4 NMR Instrumentation

In this research work, FID measurements were performed on the 7.1 T superconducting magnet and the Keck powered magnet. These two experimental platforms required different configurations of NMR instrumentation to measure FID signals. This section describes the NMR instrumentation necessary to measure FID signals on these two magnets.

A NMR probe and NMR console are the two primary devices used to measure FID signals. The general interface between the NMR probe and console is depicted in Figure 3.7. The NMR console generates an RF pulse with a transmitter and supplies the RF pulse to a power amplifier. The power amplifier provides an amplified RF pulse to a duplexer. The duplexer allows bi-directional communication over a single channel. When transmitting the RF pulse, the duplexer supplies the RF pulse to the NMR probe installed within the magnet. The probe contains a NMR sample in a cylindrical tube which is surrounded by an RF coil. The RF pulse excites a NMR response, and upon removal of this pulse, the RF coil in the probe measures the NMR response and supplies the measurement to the duplexer. The measurement is amplified with a preamplifier and then supplied to the NMR console for recording. The following two subsections describe th NMR probe and console in more detail.

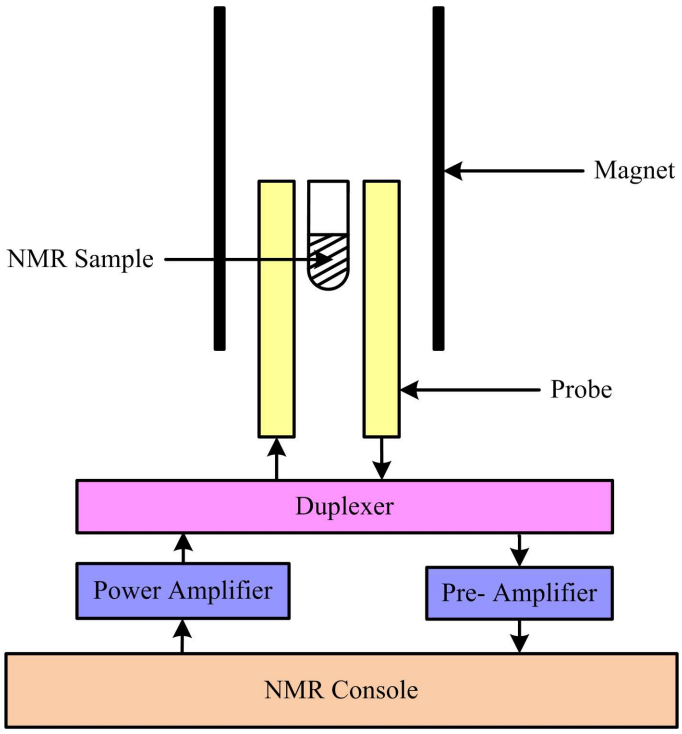

Figure 3.7. NMR console interface with NMR probe.

3.4.1 NMR Probes

Recall from Section 3.2 that in NMR spectroscopy, a transverse field $\vec{B}_1$ tips the magnetization vector from the z axis. The device used to produce the $\vec{B}_1$ field and measure the NMR response is known as an NMR probe. A NMR probe typically uses a single channel for transmitting and receiving. When an RF pulse with a frequency equivalent to the Larmor frequency is supplied to the transmit channel, an RF coil is used to produce the transverse field $\vec{B}_1$. When the RF pulse is removed, the transverse magnetization vector precesses about the z axis at the Larmor frequency in the laboratory frame. This induces a voltage in the RF coil which provides a measurement of the NMR response on the receive channel, which is the same as the transmit channel. The RF transmitter and receiver are controlled by a NMR console which will be discussed in subsection 3.4.2.

A NMR probe can have multiple transmit and receive channels with each channel tuned for a particular Larmor frequency. Two probes were necessary for this research work so that FID signals could be measured using either the Keck powered magnet or 7.1 T superconducting magnet. One probe is tuned to measure FID signals from hydrogen and deuterium nuclei at 25 T while the other probe is tuned to measure FID signals from the same nuclei at 7.1 T. Therefore these probes could be used to measure FID signals on the Keck operating at 25 T as well as the 7.1 T superconducting magnet.

The first probe is described as a High Resolution Magic Angle Spinning (HR-MAS) probe, which was used to obtain FID measurements on the Keck powered magnet. A photograph of this probe is shown in Figure 3.8. This probe has two transmit and receive channels. One channel is tuned to approximately 1.065 GHz, which is the Larmor frequency of hydrogen nuclei at 25 T. This channel was used to excite hydrogen nuclei at 25 T with RF pulse signals and observe the FID response.

The other channel is tuned to approximately 163 MHz, which is the 25 T Larmor frequency of the reference deuterium nuclei used for NMR feedback control. This allows for excitation and observation of the FID response of the deuterium nuclei at 25 T. Using the two channels, hydrogen and deuterium FID signals can be simultaneously observed with this probe. This probe is also capable of spinning the NMR sample up to a rate of 15 kHz. Spinning the sample causes the nuclei to see an average value of the spatial field distribution, and therefore reduces the linewidth broadening due to spatial field inhomogeneities [23, 24, 20]. Recall from section 2.1 that the pickup coil used for inductive measurements is also contained within this probe. The probe is mounted from the bottom of the Keck powered magnet.

Figure 3.8. Photograph of the HR-MAS probe used for NMR measurements.

The second probe is described as the Bruker probe, which was used to obtain NMR measurements on the 7.1 T superconducting magnet. A photograph of this probe is shown in Figure 3.9. Like the HR-MAS probe, this probe has two transmit and receive channels. One channel is tuned to approximately 300 MHz, which is the Larmor frequency of hydrogen nuclei at 7.1 T. The other channel is tuned to approximately 46 MHz, which is the Larmor frequency of deuterium nuclei at 7.1 T. These two transmit and receive channels allow for simultaneous excitation and observation of hydrogen and deuterium nuclei NMR signals at 7.1 T.

Unlike the HR-MAS probe, this probe does not have a pickup coil. If inductive measurements were required for an experiment on the 7.1 T superconducting magnet, then the pickup coil from the HR-MAS probe would have to be used in conjunction with the Bruker probe to obtain both inductive and NMR measurements. This was done by mounting the Bruker probe from the bottom and the HR-MAS probe from the top of the superconducting magnet.

Figure 3.9. Photograph of the Bruker probe used for NMR measurements.

3.4.2 NMR Consoles

A NMR console transmits the RF pulse to the NMR probe and receives the NMR response measurement from the probe. A transmitter within the NMR console generates the RF pulse supplied to the RF coil of the NMR probe. Upon removal of the RF pulse, the NMR response measured by the probe is provided to a receiver which resolves the measurement into quadrature components. The timing between the transmitter RF pulse and when the receiver observes the NMR response is controlled by a pulse sequence. The pulse sequence can be repeated to provide multiple measurements of the NMR response.

The receiver in a NMR console uses quadrature phase detection to demodulate the NMR measurement and resolve it into quadrature components. Figure 3.10 shows a block diagram of the quadrature phase detection scheme used in NMR console receivers. The signal $S(t)$ is a voltage measurement representing the transverse magnetization with a Fourier spectrum centered at the Larmor frequency ω_0. The NMR console operator chooses the RF signal frequency ω_r. When the signal $S(t)$ is mixed with $\cos(\omega_r t)$ it is demodulated to the frequencies $\omega_0 - \omega_r$ and $\omega_0 + \omega_r$. The low pass filter then eliminates the frequency component at $\omega_0 + \omega_r$, and its output is a measurement $S_u(t)$ representing $M_u(t)$.

Similarly, when $S(t)$ is mixed with $\sin(\omega_r t)$ it is demodulated to frequencies $\omega_0 - \omega_r$ and $\omega_0 + \omega_r$. Here the mixer output has a 90° phase difference from the signal mixed with $\cos(\omega_r t)$. This results in a measurement $S_v(t)$ representing $M_v(t)$ which is 90° out of phase from $S_u(t)$. The low pass filters in this detection scheme set the measurement bandwidth of the NMR signals.

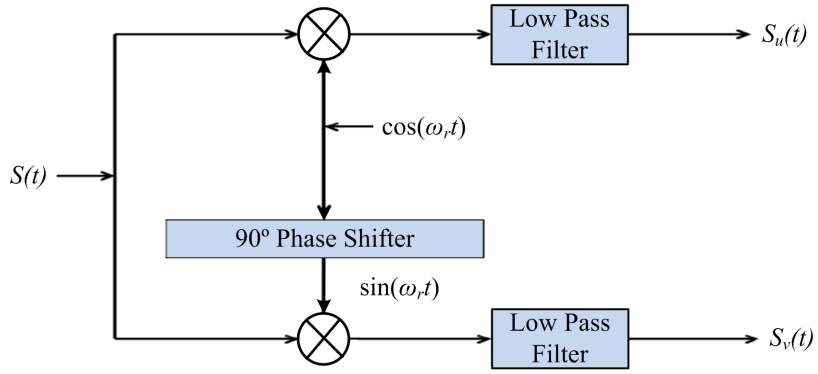

Figure 3.10. Quadrature phase detection of a NMR console.

The discussion from Sections 3.2 and 3.3 on FIDs assumed the frequency of the RF signal is chosen to be the Larmor frequency γB_0 or ω_0. In NMR experiments, measurements are often obtained using an RF signal frequency ω_r that is relatively close to the Larmor frequency but not exact. This results in signals $S_u(t)$ and $S_v(t)$ having a baseband frequency defined by

$$\omega_b = \omega_0 - \omega_r. \tag{3.23}$$

For the vector representation of the magnetization, a non-zero ω_b implies the transverse magnetization vector $\vec{M}_{uv}$ rotates about the z axis at a frequency ω_b. Recall from the Section 3.1 that in the rotating reference frame, the $u-v$ plane rotates about the z axis at γB_0 or ω_0. In this reference frame, when a RF pulse with frequency γB_0 is removed, the magnetization vector does not precess about the z axis as it returns to thermal equilibrium. However, if the RF signal frequency is different from the Larmor frequency, then the magnetization vector precesses about the z axis as it returns to thermal equilibrium. The transverse magnetization vector $\vec{M}_{uv}$ rotates about the z axis at a baseband frequency ω_b that is the difference of the Larmor frequency ω_0 and RF signal frequency ω_r.

Three NMR consoles were used to measure NMR signals in this research work. These consoles are defined herein as the Tecmag spectrometer, Tecmag lock, and NMRkitII. The Tecmag spectrometer was used to obtain hydrogen FID signals for deriving the linewidth and peak frequency

shift performance metrics introduced in Section 1.6. These metrics are derived in Chapter 6 and will provide information about the how well the cascade feedback control system reduces field fluctuations. The Tecmag lock console was used to demonstrate limitations of a previous field-frequency lock design in powered magnets. Experimental data obtained using this console will be shown in Chapter 4. The NMRkitII was used to measure the analog signals $S_u(t)$ and $S_v(t)$ from the reference deuterium nuclei dissolved in the NMR sample to use in estimating field fluctuations. Experimental measurements using this console will be shown in Chapters 5 and 6.

The first console described here is a Tecmag spectrometer whose block diagram is depicted in Figure 3.11. A host computer controls the pulse sequence generator, which is responsible for synchronizing the timing of the transmit and receive operations, as well as providing the RF pulse amplitude and width for a desired tip angle θ. When the pulse sequence requests that an RF pulse is transmitted, the transmitter supplies the RF pulse to the power amplifier from Figure 3.7.

When a measurement of the NMR response is available, the receiver digitizes the NMR measurement and resolves it into quadrature components for communication with the host computer. The low pass filter of the quadrature phase detector can be tuned by the host computer. The pulse sequence generator controls the sample period and acquisition time of the digital quadrature components S_u and S_v. This console does not easily provide access to the real–time signals of the quadrature components.

The second NMR console used for experimental measurements in this research work was the Tecmag lock console. This console uses an indirect field-frequency lock (FFL) to regulate the analog measurement S_v to zero with a proportional plus integral plus derivative (PID) compensator. Under certain conditions, regulating S_v to zero also regulates field fluctuations to zero. The details of this FFL and its limitations in powered magnets will be discussed in Chapter 4. The pulse sequence of this console has a fixed pulse repetition rate and pulse width. The pulse repetition rate, defined as the time between consecutive RF pulses, is 500 μs. The pulse width

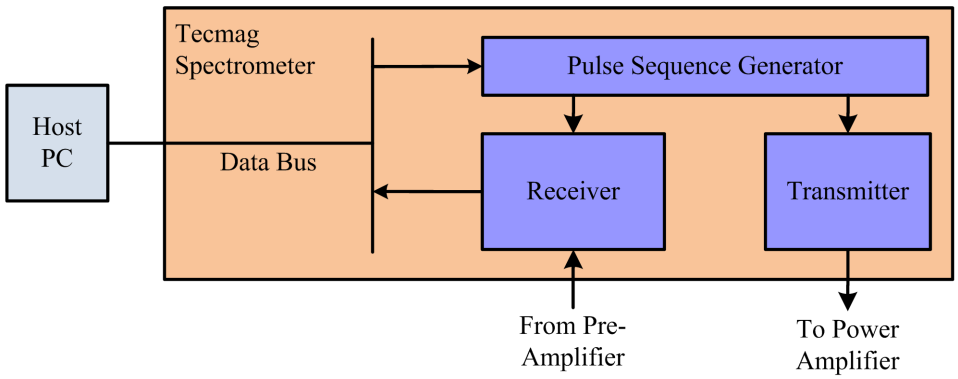

Figure 3.11. Block diagram of the Tecmag NMR console.

was measured to be approximately 70 μs [29]. The tip angle θ of the NMR response is controlled by the adjustable amplitude of the RF pulse.

The receiver filter is set to the *fast* operating mode so as to give the highest cutoff frequency of the low pass filter in the receiver. The receiver resolves the NMR measurement into quadrature components, which is sampled once per pulse, and provides the digitized signal S_v to the PID compensator whose gains are adjustable through software. Using measurements of the digital signal S_v, the compensator generates an correction voltage V_c which can be provided to a current amplifier and correction coil to suppress field fluctuations. Note that if the compensator gain is proportional only, then the output of the compensator can be used to measure S_v in real–time.

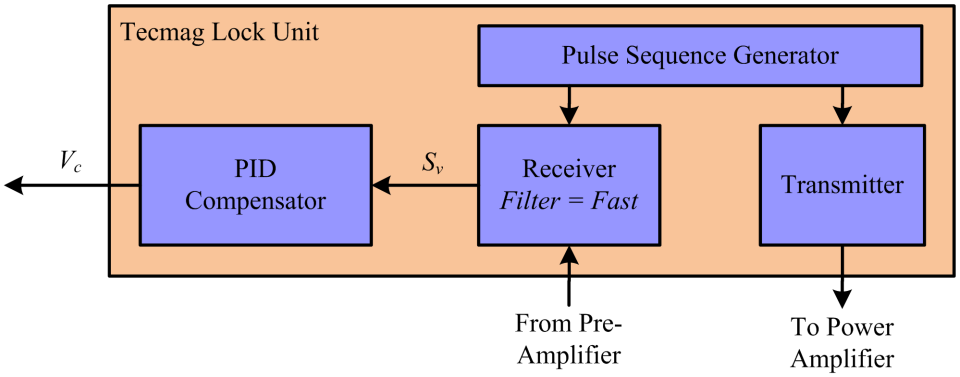

Figure 3.12. Block diagram of the Tecmag lock NMR console.

The third NMR console used for experimental measurements in this research work is described as the NMRkitII console. The pulse sequence timing for this NMR console is controlled by the

external digital gate signals *TX Gate* and *RX Gate*. These gate signals enable the transmit and receive operations of pulse sequence. When *TX Gate* is set high, the RF pulse is supplied to the power amplifier, where the amplitude of the RF pulse and the RF signal frequency ω_r is set by an external frequency synthesizer. The RF pulse width is set by the width of *TX Gate*. When *RX Gate* is high, the receiver measures the NMR response and resolves it into analog quadrature components $S_u(t)$ and $S_v(t)$. The width of *RX Gate* determines the acquisition time of the NMR measurement. The receiver filter is a 4 pole Butterworth low pass filter where the cutoff frequency is typically set to 10 kHz. The tradeoffs in choosing this cutoff frequency will be discussed in subsection 5.3.2. Analog measurements of $S_u(t)$ and $S_v(t)$ are available in real–time with this NMR console.

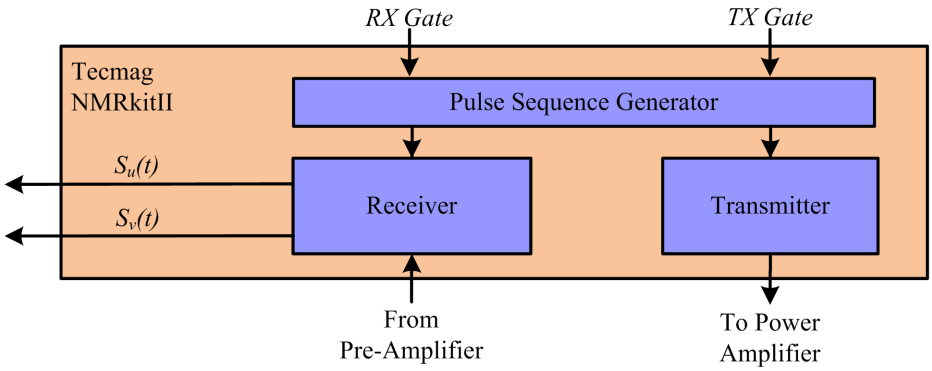

Figure 3.13. Block diagram of the NMRkitII NMR console.

When comparing these three NMR consoles, there are several features to discuss. The NMR signals available for real–time measurement are of central importance when considering estimation and control using NMR. For the Tecmag spectrometer, the NMR signals S_u and S_v are digital and sent directly to the host computer. As a result, it is very difficult to access the hardware for real–time measurements of these signals. The Tecmag lock provides real–time measurements of the digital signal S_v when a proportional compensator is chosen. The NMRkitII provides real–time measurements of analog signals $S_u(t)$ and $S_v(t)$.

There are several advantages to measuring both $S_u(t)$ and $S_v(t)$ in real–time as opposed to measuring just S_v for NMR feedback control in powered magnets. These advantages will be discussed in Chapter 4. The Tecmag spectrometer and NMRkitII both have an adjustable pulse sequence while the pulse repetition rate and pulse width of the Tecmag lock console is fixed. Table 3.2 summarizes the features of the three NMR consoles discussed in this section.

Console	**Pulse Sequence**	**Accessible Real–Time NMR Signals**	**NMR Signal Type**
Tecmag Spectrometer	Adjustable	None	–
Tecmag Lock	Fixed Pulse Repetition Rate, Fixed Pulse Width	S_v	Digital
NMRkitII	Adjustable	$S_u(t)$ $S_v(t)$	Analog

Table 3.2. Salient features of NMR consoles.

The following Chapter examines feedback control using NMR measurements, or FFLs. A discussion of the prior methods using feedback control of NMR measurements is provided including indirect FFLs often used in superconducting magnets. The application of these FFLs to powered magnets is studied through analysis and experimental results, where experimental results are obtained using the indirect FFL in the Tecmag lock console.

Chapter 4

Field-Frequency Locks in Powered Magnets

Recall from Section 1.4 that inductive measurements have limited ability to estimate lower frequency fluctuations due to poor measurement SNR and low pass filtering effects at low frequencies. The lower frequency limitations of inductive measurements can be overcome by estimating field fluctuations using NMR measurements. Section 1.5 introduced NMR feedback control, or field-frequency locks (FFLs), which use NMR measurements to estimate lower frequency fluctuations without the limitations of inductive measurements.

This chapter examines FFL techniques in more detail, and analyzes their application to powered magnets. Using the background about NMR physics in Chapter 3, it will be discussed how particular NMR signal components can be used to estimate lower frequency fluctuations. A common FFL technique designed for superconducting magnets will be studied along with its application to powered magnets.

Section 4.1 provides a literature survey of FFLs and their techniques for estimating and reducing lower frequency fluctuations. Section 4.2 provides analysis of a common FFL technique designed for superconducting magnets. Section 4.3 shows the limitations of this FFL technique in powered magnets.

4.1 Survey of Field-Frequency Lock Techniques

Recall from Section 3.4 that a NMR probe and console obtains voltage signals $S_u(t)$ and $S_v(t)$, which represent measurements of the quadrature component signals $M_u(t)$ and $M_v(t)$. In some cases, for example the NMRkitII console, it is possible to access $S_u(t)$ and $S_v(t)$ in real–time. In other cases, for example the NMR Tecmag console, it is difficult to access these signals in real–time. Given these various NMR configurations, it is not surprising that FFLs measure different NMR signal components to estimate lower frequency fluctuations.

Field-frequency locks were classified in Section 1.4 as indirect or direct. Indirect and direct FFLs measure or estimate NMR signal components which are indirectly or directly related to field fluctuations $B_f(t)$. More specifically, indirect FFLs measure either $M_v(t)$ or $\phi(t)$ to provide estimates of $B_f(t)$. The vector representation of the magnetization vector in Figure 3.5 shows that $M_v(t)$ and $\phi(t)$ are non-zero when field fluctuations are present. Therefore it is reasonable to use measurements of these signals to estimate field fluctuations.

Direct FFLs measure or estimate the frequency $\omega_f(t)$ which is equivalent to $\gamma B_f(t)$, and is directly proportional to $B_f(t)$. Recall from Figure 3.5 that when $B_f(t)$ is present the transverse magnetization vector $\vec{M}_{uv}$ precesses about the z axis at a frequency $\omega_f(t)$. Therefore measurements or estimates of $\omega_f(t)$ provide an estimate of $B_f(t)$. In an effort to provide a historical overview of indirect and direct FFLs, the reminder of this section provides a literature survey in chronological order of these FFLs.

Original FFLs were indirect using measurements from continuous-wave NMR spectrometers. Prior to the advent of pulsed spectrometers, NMR spectroscopy was performed by exciting the nuclei with a continuous-wave RF signal. The first FFL measured $M_v(t)$ from a continuous-wave spectrometer in 1948 [45]. The signal $M_v(t)$ representing an indirect estimate of $B_f(t)$ was fed through a proportional compensator to regulate current supplied to the magnet which regulates field. This approach is insufficient for the powered magnets studied in this dissertation as other factors besides power supply current are sources of field fluctuations, for example cooling water temperature and flow rate. In 1957, Baker and Burd [46] described an indirect FFL using a continuous-wave spectrometer to measure $M_v(t)$ from a reference sample. Rather than regulate the magnetic field, this group varied the spectrometer reference frequency ω_r to offset the predicted frequency shift caused by the field fluctuation estimate. This preserved the Larmor frequency of the NMR signal in spite of the field fluctuations present.

In the late 1950's, a class of continuous-wave NMR experiments known as time-sharing or time-division was developed. Grunwald *et al.* [47] and Anderson *et al.* [48] attributed this approach to Arnold [49]. In this method, RF signals excite the nuclei for a short time duration, where the time between each RF signal is large compared to the RF time duration. When the RF pulse is removed, the NMR response is measured for a chosen amount of time between the next RF pulse. In 1962, Grunwald *et al.* reported the first known indirect FFL using measurements of $M_v(t)$ in response to time-shared NMR. Similar to Baker *et al.*, these measurements of $M_v(t)$ were used to vary the spectrometer reference frequency to offset the effects of field fluctuations.

During the 1950's, pulsed NMR spectroscopy was beginning to develop. The remaining techniques mentioned here used measurements from pulsed NMR spectroscopy as this became the convention. Indirect FFLs were further developed in 1978 by Hoult *et al.* [51] and Kan *et al* [52]. Both approaches measure the phase $\phi(t)$ and use a phase-locked loop to regulate $\phi(t)$ to zero. Hoult's design considered mathematical analysis of the NMR response and assumed $\phi(t)$ was small so that $\sin\phi(t)$ is approximately $\phi(t)$. This approximation is not valid in a powered

magnets where large field fluctuation amplitudes cause large perturbations in the phase angle. Kan *et al.* used an integral compensator while Hoult *et al.* used a proportional plus integral compensator.

In 1978, Hofer *et al.* published a patent [58] describing the first known direct FFL using a frequency counter to directly measure $\omega_f(t)$, and thus field fluctuations, in a superconducting magnet. The frequency counter measures FID signal frequency and compares the result to a desired baseband frequency to obtain a direct estimate of $\omega_f(t)$.

One year later in 1979, Hill published a patent [53] describing a FFL capable of operating in indirect or direct modes. If the FID signal frequency is not close to zero, then the FFL generates FID signals by exciting the nuclei with high power RF pulses at a low repetition rate. A frequency counter directly measures the frequency of $M_u(t)$ as an error signal. The polarity of the correction signal is determined by a phase comparison between $M_u(t)$ and $M_v(t)$. If $M_u(t)$ leads $M_v(t)$, then the Larmor frequency ω_0 is greater than the spectrometer reference frequency ω_r. Similarly if $M_u(t)$ lags $M_v(t)$, then ω_0 is less than ω_r. When the FID signal frequency passes through the resonant condition ω_0 equal to ω_r, the FFL switches to an indirect operating mode. In this mode the FFL excites the nuclei with low power pulses at a high repetition rate and measures $M_v(t)$ as an error signal for correction.

Fifteen years later Schett *et al.* proposed another significant direct FFL in 1994 [60]. In this patent, the frequency difference of the FID signal from the Larmor frequency $\Delta\omega$ is derived as

$$\Delta\omega = \frac{1}{T_2}\frac{M_u(t)}{M_v(t)} + \frac{1}{M_v(t)}\frac{dM_u(t)}{dt}. \tag{4.1}$$

The expression in equation 4.1 is derived from the Bloch equations in the rotating reference frame, and depends on the NMR time constant T_2. If the spectrometer reference frequency ω_r is equivalent to the Larmor frequency ω_0, then $\Delta\omega$ is a direct estimate of $\omega_f(t)$. The frequency difference $\Delta\omega$ is used as an error signal and is fed through a proportional compensator and correc-

tion coil to regulate the FID signal frequency to the Larmor frequency. Four years later, Schnur *et al.* proposed a method which estimates $\omega_f(t)$ from the derivative of $\phi(t)$, and again supplies the estimate to a correction coil using a proportional compensator. A derivative operation is not recommended for feedback control as it accentuates high frequency noise.

In 2000, Soghomonian *et al.* combined an indirect FFL with inductive feedback control, and demonstrated this system in a 24 Tesla powered magnet [31]. The indirect FFL used measurements of $M_v(t)$. While this work showed reduction in overall field fluctuations, the FFL design does not consider NMR dynamics in response to the pulse sequence and temporal field fluctuations. Another direct FFL design was proposed in a 2007 patent by Park *et al* [61]. Park's design assumed the magnetization components $M_u(t)$ and $M_v(t)$ reached a steady-state value when deriving an expression for deviation of FID signal frequency from the Larmor frequency. Sections 4.2 and 4.3 provides a more detailed discussion of the steady-state magnetization behavior and its limitations in powered magnets.

In 2008, Samra was the first to design an indirect FFL using measurements of $M_v(t)$ from a NMR dynamics model [29, 57]. Section 4.2 describes some of the salient features of this dynamics model. This model was used to design a dead-beat compensator which rejects a step change in field fluctuations in an optimal time. One year later Schenkel *et al.* proposed a design which combines a direct FFL with a device described as a multi-selective filter [56]. The direct FFL estimates and reduces broadband lower frequency fluctuations while the multi-selective filter is designed to reduce periodic lower frequency fluctuations. The measurement bandwidth of the field fluctuations for this design has an upper cutoff frequency limited by the RF pulse spacing used to obtain NMR signals.

Recent indirect and direct FFLs have been proposed in 2012. A 1.56 kHz (20 ppm) linewidth of NMR spectra was achieved using both a pulse sequence insensitive to field fluctuations in conjunction with an indirect FFL [41]. This linewidth is still much larger than the 100 Hz desired for NMR spectroscopy. Takahashi's group adopted the concept proposed by Hofer *et al.*

wherein a frequency counter directly measures $\omega_f(t)$ [59]. Here the frequency counter estimated $\omega_f(t)$ from a reference sample in a powered magnet operating at 11.74 T. The estimate was supplied through a proportional compensator to a correction coil to suppress fluctuations.

It will be shown in Section 4.2 that typical indirect FFLs measuring $M_v(t)$ requires knowledge of NMR time constants. Furthermore, several direct FFLs require explicit knowledge of NMR time constants to estimate $\omega_f(t)$ [60, 61, 56]. For example, the expression for $\Delta\omega$ in equation 4.1 depends on the NMR time constant T_2. These approaches are not desirable for powered magnets as precise knowledge of NMR time constants is often difficult. Conversely, direct FFLs using frequency counters do not require knowledge of NMR time constants as they directly measure $\omega_f(t)$.

The majority of FFLs described in this literature survey were designed for permanent or superconducting magnets. Three FFLs described in this survey were, however, designed for powered magnets [31, 41, 59]. Soghomonian *et al.* demonstrated an indirect FFL in a powered magnet operating at 24 T, which required the cooling water temperature to change by less than 0.3°C/min, corresponding to field changes, or fluctuations which are less than 1.22 G/min (5.1 ppm/min) [31]. Experimental results in Figure 1.13 showed that the field can change by more than 9 G/min (32 ppm/min), and so this indirect FFL would be insufficient. Another indirect FFL demonstrated in a powered magnet at 30 T only achieved a linewidth of 1.56 kHz (20 ppm), which is much larger than the desired 100 Hz [41].

Takahashi *et al.* demonstrated a direct FFL on a powered magnet operating at 11.74 T [59]. Unlike the indirect FFL shown by Soghomonian *et al.*, this approach estimated fields that change by much more than 1.22 G/min (5.1 ppm/min). Additionally, as mentioned before this approach does not require explicit knowledge of NMR time constants T_1, T_2 and T_2^*. While these features make this an attractive approach for implementing a FFL in a powered magnet, this approach does not consider aliasing of higher frequency fluctuations. Therefore the direct FFL shown in this research work adopts the concept of using FID signal frequency to estimate

lower frequency fluctuations while considering aliasing of higher frequency fluctuations. Chapter 5 presents direct estimation methods with the objective of estimating $\omega_f(t)$ without knowledge of NMR time constants, and demonstrates aliasing of higher frequency components as well as a method for reducing aliasing.

Indirect FFLs measuring $M_v(t)$ are often described as dispersion locks in the NMR community. This is because the NMR component signal $M_v(t)$ is also defined as the dispersion component of the NMR signal. These FFLs are simple to implement and are widely used in NMR instrumentation with superconducting magnets [54, 55, 13]. The application of dispersion locks to powered magnets is investigated in the following sections. Section 4.2 analyzes a dynamics model of $M_v(t)$ in response to a dispersion lock pulse sequence in the presence of field fluctuations. Section 4.3 demonstrates limitations of a dispersion lock in powered magnets.

4.2 Dispersion Lock Analysis

Dispersion locks measure a signal representing $M_v(t)$ in response to a high repetition rate pulse sequence, and regulate this indirect estimate of $B_f(t)$. In order to understand the operation of dispersion locks, a dynamics model governing the response of $M_v(t)$ to this pulse sequence in the presence of $B_f(t)$ should be considered. This section presents such a dynamics model and analyzes it for typical $B_f(t)$ observed in superconducting magnets. This will explain why dispersion locks have been effective for superconducting magnets. Additionally, this model is used in the following section when discussing dispersion lock limitations in powered magnets.

In 2008, Samra [29, 57] was the first to consider a dynamics model when designing a compensator for a dispersion lock. This design, demonstrated on the 7.1 T superconducting magnet, used measurements of $M_v(t)$ in response to a high repetition rate pulse sequence. A small-signal linear model as well as a steady-state approximation was derived from a nonlinear discrete-time NMR dynamics model [67]. The nonlinear discrete-time model and corresponding steady-state

approximation from this analysis are studied here to demonstrate the operation of a dispersion lock in superconducting magnets. It may be useful to refer to the vector representation of the magnetization response in Figure 3.5 for the following discussion of these NMR dynamics models.

Consider the pulse sequence with RF pulses of width t_w and pulse period T, as shown in Figure 4.1. These pulses tip the magnetization vector $\vec{M}$ an angle θ from the z axis. As discussed in Section 3.3, the presence of temporal field fluctuations from times 0 to t, directed along the z axis, cause the magnetization vector $\vec{M}_{uv}$ to sweep a phase angle $\phi(t)$. For pulse sequence in Figure 4.1, field fluctuations present during the time interval $t_k + t_w$ to t_{k+1} cause $\vec{M}_{uv}$ to sweep a phase angle during this interval.

The pulse width t_w is small to achieve a small tip angle, resulting in a t_w that is much smaller than the pulse period T. For superconducting magnets, any field fluctuations that are present will change slowly over a long period of time, and the pulse period T is much shorter than time scale of these field fluctuations. As a result, the field fluctuations can be assumed constant during the time interval $t_k + t_w$ to t_{k+1}. The constant field fluctuation in the k^{th} time interval is denoted $B_f(k)$ and the corresponding phase angle swept over this time interval is denoted as $\phi(k)$.

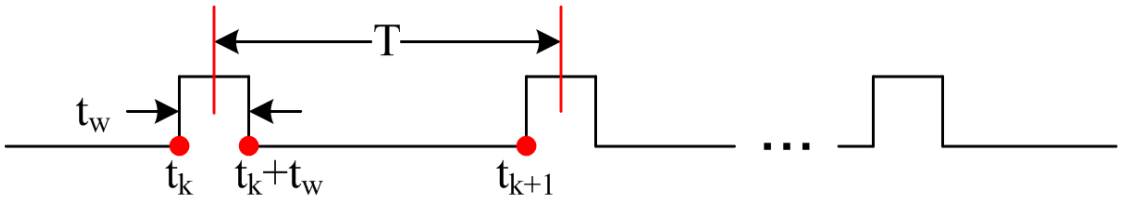

Figure 4.1. High repetition rate RF pulse sequence for dispersion lock.

The discrete-time dynamics model that maps an magnetization vector $\vec{M}$ from times t_k to t_{k+1} in response to the pulse sequence in Figure 4.1 and $B_f(k)$ was described by Schiano *et al* [67]. This model considered the magnetization response for an ensemble of identical nuclei experiencing a homogeneous magnetic field B_0. Recall from Section 3.2 that when the field is homogeneous, the NMR time constant T_2 models the decay of the transverse magnetization. If the magnetization response for multiple ensembles of nuclei is instead considered, where a

inhomogeneous field is present, then the ensemble average of the magnetization response can be used where the NMR time constant T_2 can be replaced by T_2^*.

By denoting the vector $\vec{M}$ at time t_k and t_{k+1} as $M(k)$ and $M(k+1)$ respectively, the discrete-time dynamics model derived by Schiano *et al.* with T_2 replaced by T_2^* is

$$M(k+1) = A\left(T_1, T_2^*\right) W(\phi(k)) V(\theta) M(k) + B\left(T_1\right), \tag{4.2}$$

where

$$V(\theta) = \begin{bmatrix} \cos\theta & 0 & -\sin\theta \\ 0 & 1 & 0 \\ \sin\theta & 0 & \cos\theta \end{bmatrix},$$

$$A\left(T_1, T_2^*\right) = \begin{bmatrix} e^{-T/T_2^*} & 0 & 0 \\ 0 & e^{-T/T_2^*} & 0 \\ 0 & 0 & e^{-T/T_1} \end{bmatrix},$$

$$W(\phi(k)) = \begin{bmatrix} \cos\phi(k) & -\sin\phi(k) & 0 \\ \sin\phi(k) & \cos\phi(k) & 0 \\ 0 & 0 & 1 \end{bmatrix}, \text{ and}$$

$$B\left(T_1\right) = \begin{bmatrix} 0 \\ 0 \\ M_0\left(1 - e^{-T/T_1}\right) \end{bmatrix}.$$

The matrix $V(\theta)$ models the magnetization vector $\vec{M}$ tipping an angle θ from the z axis due to the RF pulse. After the RF pulse, the matrix $A(T_1, T_2^*)$ models the relaxation of the magnetization vector back to thermal equilibrium. The matrix $W(\phi(k))$ models the magnetization

vector $\vec{M}_{uv}$ sweeping a phase angle $\phi(k)$ due to $B_f(k)$.

When the RF pulse frequency is equivalent to the Larmor frequency, the expression for the phase angle was shown in equation 3.15 of Section 3.3. For $B_f(k)$ which is constant over the time interval $t_k + t_w$ to t_{k+1}, the phase angle swept during this time interval is

$$\phi(k) = \int_{t_k+t_w}^{t_{k+1}} \gamma B_f(k) d\tau = \gamma B_f(k)[t_{k+1} - t_k - t_w] = \gamma B_f(k)[T - t_w]. \tag{4.3}$$

The pulse period T is much greater than t_w, so the difference $T - t_w$ can be approximated as T and equation 4.3 becomes

$$\phi(k) = \gamma B_f(k) T. \tag{4.4}$$

The input for the discrete-time dynamics model in equation 4.2 is $\phi(k)$ or $B_f(k)$. This model is nonlinear because of the $\cos\phi(k)$ and $\sin\phi(k)$ terms in the matrix $W(\phi(k))$. As nonlinear systems are difficult to analyze, Samra derived simplified models by placing restrictions on the parameters T_1/T , T_2^*/T , θ and $\phi(k)$ [29, 57]. This section studies one of Samra's simplified models which is a steady-state approximation to the nonlinear model. This model will be used to discuss the operation of dispersion locks on superconducting magnets.

The steady-state model assumes the field fluctuation $B_f(k)$, which is constant during the k^{th} time interval, remains constant over many sample instants. For this assumption $B_f(k)$ can be replaced by B_f, and as the phase angle $\phi(k)$ is proportional to $B_f(k)$, it can be replaced by a constant phase angle ϕ. In this case, the magnetization will eventually reach a steady-state value denoted M^{ss} where $M(k)$ is equivalent to $M(k+1)$. The nonlinear discrete-time dynamics model of the magnetization from equation 4.2 can be approximated by a nonlinear but instantaneous map from B_f to M^{ss}.

In addition to constant field fluctuations, the amplitude of B_f, and consequently the phase angle ϕ, was assumed to be small. This allows for the small angle simplification where $\cos\phi$ and $\sin\phi$ are approximated by one and ϕ respectively. The pulse sequence in Figure 4.1 implies the

pulse period T is much smaller than T_1 and T_2^*. This allows for exponential terms in the matrix $A(T_1, T_2^*)$ to be simplified using a first order Taylor Series expansion where e^{-T/T_1} and e^{-T/T_2^*} are approximated by $1 - T/T_1$ and $1 - T/T_2^*$ respectively. The pulse sequence in Figure 4.1 also implies θ is small, so $\cos\theta$ and $\sin\theta$ can be approximated by one and θ respectively. Using these simplifications, the steady-state components of the magnetization were derived as [29, 57]

$$M_u^{ss} = \frac{-\frac{\theta}{T} T_2^* M_0}{1 + \left(\frac{\theta}{T}\right)^2 T_1 T_2^* + \left(\gamma B_f T_2^*\right)^2} \tag{4.5}$$

$$M_v^{ss} = \frac{-\gamma B_f \frac{\theta}{T} T_2^{*2} M_0}{1 + \left(\frac{\theta}{T}\right)^2 T_1 T_2^* + \left(\gamma B_f T_2^*\right)^2} \tag{4.6}$$

$$M_z^{ss} = \frac{\left[1 + \left(\gamma B_f T_2^*\right)^2\right] M_0}{1 + \left(\frac{\theta}{T}\right)^2 T_1 T_2^* + \left(\gamma B_f T_2^*\right)^2}. \tag{4.7}$$

The focus of this analysis is on the magnetization component M_v because it is the signal measured by dispersion locks. The steady-state magnetization component M_v^{ss} in equation 4.6 shows that M_v^{ss} is proportional to B_f. Thus if the signal M_v has reached steady-state and is regulated to zero then B_f is also regulated to zero. This is why dispersion locks regulate M_v to zero because in steady-state this implies B_f is regulated to zero. Additionally, M_v^{ss} depends on NMR time constants T_1 and T_2^*, and the mapping from B_f to M_v^{ss} is nonlinear due to the B_f^2 term in the denominator of equation 4.6.

Figure 4.2 shows the steady-state magnetization component M_v^{ss} as a function field fluctuations B_f. As expected, the relationship between M_v^{ss} and B_f is nonlinear and B_f is zero when M_v^{ss} is zero. While this figure shows a nonlinear mapping from B_f to M_v^{ss}, it also revels that if B_f is small then the mapping from B_f to M_v^{ss} is linear. The region where B_f is small enough for this linear mapping is defined as the full width of the linear region (FWLR). When B_f is within the FWLR, a linear compensator can be designed from a small-signal model for use in a dispersion lock as was shown by Samra [29, 57]. This is not recommended, however, for powered magnets as field fluctuations are typically much greater in amplitude than the FWLR.

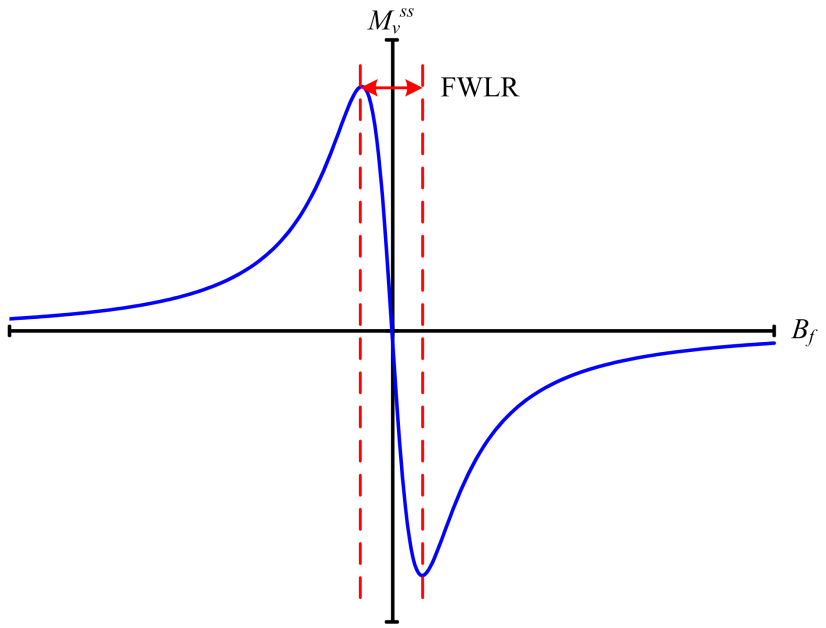

Figure 4.2. Magnitude of steady-state magnetization for constant field change B_f.

There are two conditions on B_f which simplify the compensator design for a dispersion lock. The first was mentioned above when B_f is within the FWLR, allowing for a linear compensator design. The second is when B_f changes slowly compared to the spin-lattice relaxation time constant T_1. Recall from Section 3.1 that T_1 is much greater than T_2 and hence T_2^*. Therefore T_1 is the dominant time constant implying that the steady-state behavior of M_v depends on T_1. When B_f changes quickly with respect to T_1 then the steady-state model is no longer valid and M_v is no longer proportional to B_f. Both these conditions are likely to be invalid in a powered magnet where transient field fluctuations with large amplitudes over a small time scale are typically observed.

The remainder of this section shows two simulation results. The first result supports the assertion that steady-state M_v behavior depends on T_1. The second result evaluates the M_v response to a B_f which varies slowly with respect to T_1, which will show that a dispersion lock can use M_v to regulate such a B_f. The steady-state model in equation 4.6 is compared to the full nonlinear dynamics model in equation 4.2 for both simulations. As FWLR and T_1 are the

parameters of interest, B_f and simulation time will be normalized by FWLR and T_1 in these simulations.

In order to execute these simulations, the NMR parameters listed in Table 4.1 were used. The pulse period T was chosen as 500 μs because this matches the pulse period for the Tecmag lock console described in subsection 3.4.2. The FWLR was measured using results from a the Tecmag lock field sweep. The NMR time constants T_1 and T_2^* were measured using the Tecmag NMR console described in subsection 3.4.2. The NMR sample used throughout this work contains 90 % deuterium and 10 % water with 50 mM copper sulfate doping. The deuterium nuclei in this sample represent the reference sample that will be used throughout this dissertation. This means any FFL design will be tested using the NMR response to RF pulses with transmit frequencies near the deuterium Larmor frequency. Thus the time constants T_1 and T_2^* were measured for deuterium nuclei and the gyromagnetic ratio γ was chosen for deuterium.

Parameter	**Value**
θ	0.3°
T	500 [μs]
T_1	283.2 [ms]
T_2^*	22.4 [ms]
γ	653.6 [Hz/G]
M_0	1 [m^2A]
$FWLR$	22.9 [mG]

Table 4.1. NMR parameters for simulating Mv response using steady-state and full nonlinear models.

A step field disturbance was chosen for the first simulation. A field fluctuation of this type will allow one to observe the transient response of M_v during the step field change as well as the steady-state behavior when the field remains constant. The amplitude of the step field disturbance was chosen as three times the FWLR, so as to observe any effects of a larger amplitude disturbance on the M_v response. In the presence of this step field disturbance, the M_v response was simulated using both the full nonlinear dynamics model and the steady-state model represented in equations 4.2 and 4.6 respectively.

Figure 4.3 shows the M_v response to this step field disturbance changing from 0 to three times the FWLR at time $0.5T_1$. The horizontal axis shows time normalized by T_1 and the vertical axis shows the M_v response normalized by M_0 for the two models. The steady-state model is an instantaneous map from field to M_v, so its response to step field disturbance is a step change in M_v. In contrast, the full nonlinear dynamics model has an under-damped, or oscillatory, response to the step field transient. When the field is constant for times greater than $0.5T_1$, the response of the full model eventually converges to a value matching that predicted by the steady-state model.

The step field disturbance response shown in Figure 4.3 supports the claim that the steady-state behavior of M_v depends on the NMR time constant T_1. During a transient field change, the NMR component M_v has an under-damped response. However, if the field remains constant after the field transient, then the NMR component M_v converges to the steady-state value after a time $3T_1$.

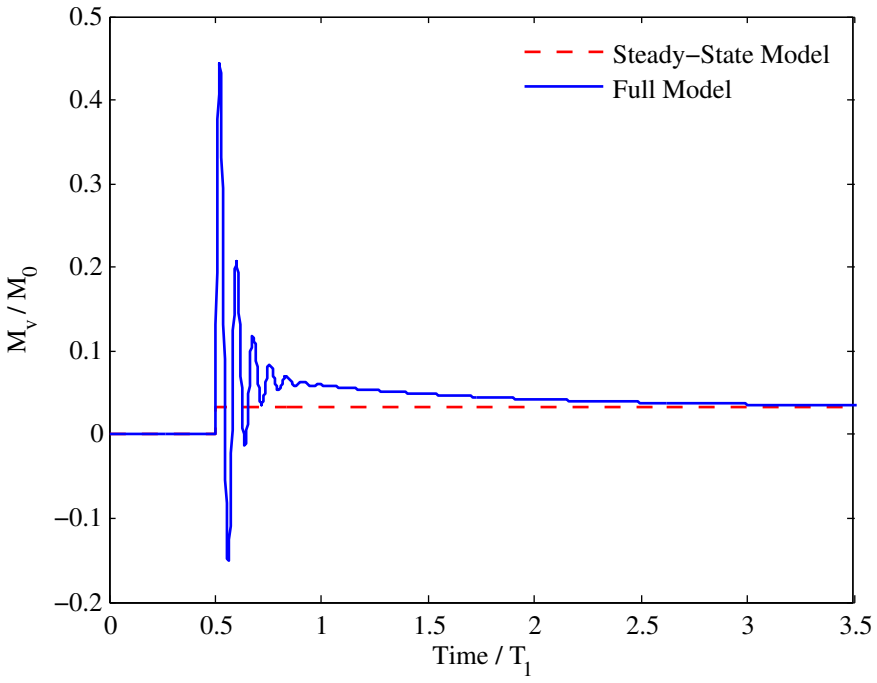

Figure 4.3. Response of M_v to a step disturbance field that is three times the FWLR.

As dispersion locks were originally designed for superconducting magnets, it is expected that any field fluctuations present will vary slowly with time. Thus the second simulation considers a field sweep varying slowly with respect to the NMR time constant T_1. This fluctuation is shown in Figure 4.4 where the horizontal axis shows time normalized by T_1 and the vertical axis shows B_f normalized by FWLR. The field sweep disturbance was chosen to be constant for a time $10T_1$, then swept slowly over a time $40T_1$, then fixed at a constant value for a time interval $10T_1$. The field was fixed before and after the sweep to ensure M_v reaches a steady-state before and after the field sweep. The field sweep was chosen to change from $\pm$ 7.5 times the measured FWLR to show the M_v response of the models for fields well outside the FWLR.

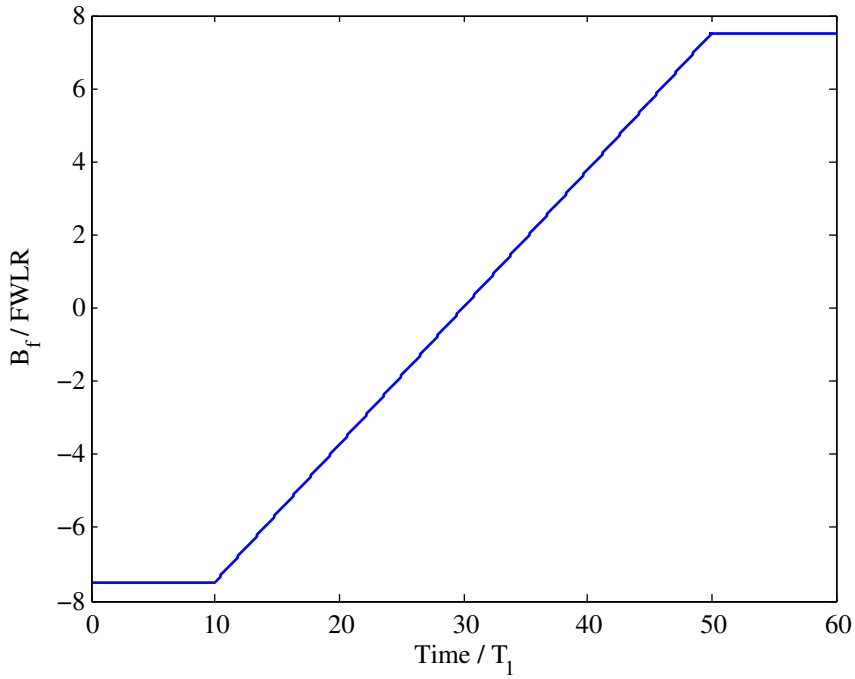

Figure 4.4. Field sweep for observing M_v response to slowly varying field with respect to T_1.

The steady-state and full nonlinear dynamics models were simulated in the presence of the field sweep disturbance shown in Figure 4.4. The simulated M_v response is shown in Figure 4.5 for both models in the presence of the field sweep disturbance from Figure 4.4. The horizontal axis is B_f normalized by FWLR and the vertical axis is the M_v response normalized by M_0.

The results of Figure 4.5 show that when the field varies slowly with respect to T_1, M_v is perturbed from steady-state as the full model does not exactly match the steady-state model for field disturbances within the FWLR. Although this is the case, the M_v response from both models does cross the horizontal axis when B_f is equal to zero. Even though the magnetization is not in steady-state, the nonlinear model response indicates that M_v can still be regulated to zero to regulate B_f to zero. Thus a dispersion lock measuring M_v and regulating it to zero would be regulating B_f to zero as long as B_f varies slowly with respect to T_1.

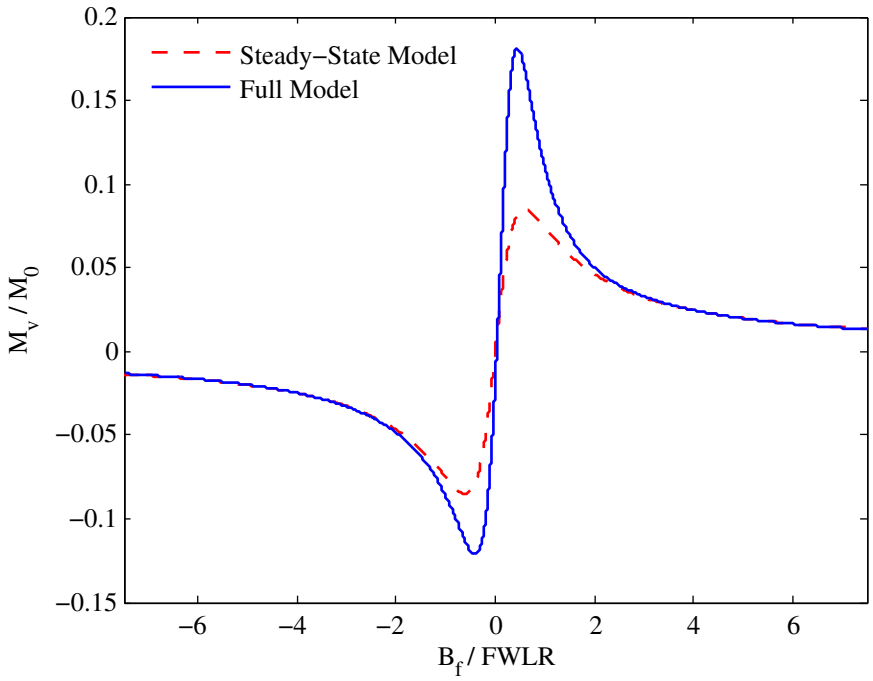

Figure 4.5. Response of M_v to field sweep that is slow with respect to T_1.

The analysis and simulation results presented in this section demonstrate that dispersion locks regulating M_v is an effective approach for reducing field fluctuations in superconducting magnets, where field fluctuations change slowly with respect to time. A nonlinear discrete-time model and steady-state approximation mapping B_f to M_v was shown. Using these models, a simulation result showed that the steady-state behavior of M_v depends on the dominant NMR time constant T_1. A second simulation result showed that if B_f varies slowly with respect to T_1,

regulating M_v to zero is equivalent to regulating B_f to zero for both models. Thus a dispersion lock is a reasonable approach for superconducting magnets.

In contrast to superconducting magnets, the B_f in powered magnets change quickly with respect to T_1. For example, recall that T_1 of deuterium nuclei was measured as 283.2 ms at 7.1 T. In the Keck powered magnet, B_f changes over fractions of a millisecond, which is much smaller than this measured value of T_1. While T_1 will change at 25 T in a powered magnet, it is still reasonable to expect that B_f will change on a time scale much smaller than T_1. The following section shows that dispersion locks are limited when B_f changes quickly with respect to T_1. The M_v response to the high repetition rate pulse sequence will be investigated in the presence of a B_f changing quickly with respect to T_1. The full nonlinear and steady-state approximation models will be used to study the mapping from B_f to M_v for such field fluctuations. Furthermore, this section will study the effects of these field fluctuations on an dispersion lock implementing a proportional plus integral (PI) compensator. Simulation and experimental results will be presented for such a dispersion lock.

4.3 Dispersion Lock Limitations in Powered Magnets

The previous section considered the dispersion lock M_v response for a field disturbance sweep changing from $\pm$ 7.5 times the FWLR over $40T_1$ seconds. Field fluctuations that change much faster than T_1 are expected in powered magnets even when inductive feedback control is employed. This is due to the upper cutoff frequency limits of the inductive feedback control system. As the intention is to develop a FFL on the Keck powered magnet, it is crucial to understand how such fluctuations affect the performance of dispersion locks.

This section shows the limitations of dispersion locks in powered magnets by studying the effect of these fluctuations through simulation and experiment. Simulations will show how a B_f that changes quickly with respect to T_1 affect the M_v response. Simulations and experiment

will be used to show the effect of such field fluctuations on a dispersion lock implementing PI compensation to regulate M_v.

The first field fluctuation considered in this section is a field sweep disturbance like that shown in Figure 4.4. In this case the field sweep is chosen to change by $\pm$ 7.5 times the FWLR over $3T_1$ and $0.1T_1$ seconds as opposed to $40T_1$ seconds in the previous section. This is to observe the M_v response for a fluctuation changing quickly with respect to T_1.

The full nonlinear model from the previous section is used to simulate the response of M_v in the presence of the field sweep disturbance. The same NMR parameter values in Table 4.1 were used for this simulation. Figure 4.6 compares the response M_v for field sweep disturbances which change over $40T_1$, $3T_1$, and $0.1T_1$. The horizontal axis is B_f normalized by FWLR and the vertical axis is M_v normalized by M_0. The solid line is the response for a field sweep changing over $40T_1$ and is the same response shown in Figure 4.5. The dashed line is the response for a field sweep changing over $3T_1$ and the dotted line is the response for a field sweep changing over $0.1T_1$.

When the field sweep disturbance changes over $3T_1$, the response M_v no longer crosses the horizontal axis when B_f is equal to zero. This implies that regulating M_v to zero does not regulate B_f to zero for this disturbance field. While it is desirable to regulate B_f to zero, regulating B_f to a constant value would still maintain a constant field in the magnet. Thus compensation of B_f could still be achieved by measuring M_v during the $3T_1$ field sweep.

However, when the field sweeps over $0.1T_1$, it would be difficult to use M_v to compensate B_f. In this case M_v crosses the horizontal axis for two different values of B_f. Thus regulating M_v to zero does not imply B_f is regulated to zero. Furthermore, there are multiple points where M_v crosses the B_f axis, so if the compensator regulates M_v to zero it may still introduce field changes. This is because M_v may be regulated to one of the zero crossings during one sample period, and the other zero crossing during another sample period depending on the disturbance field present.

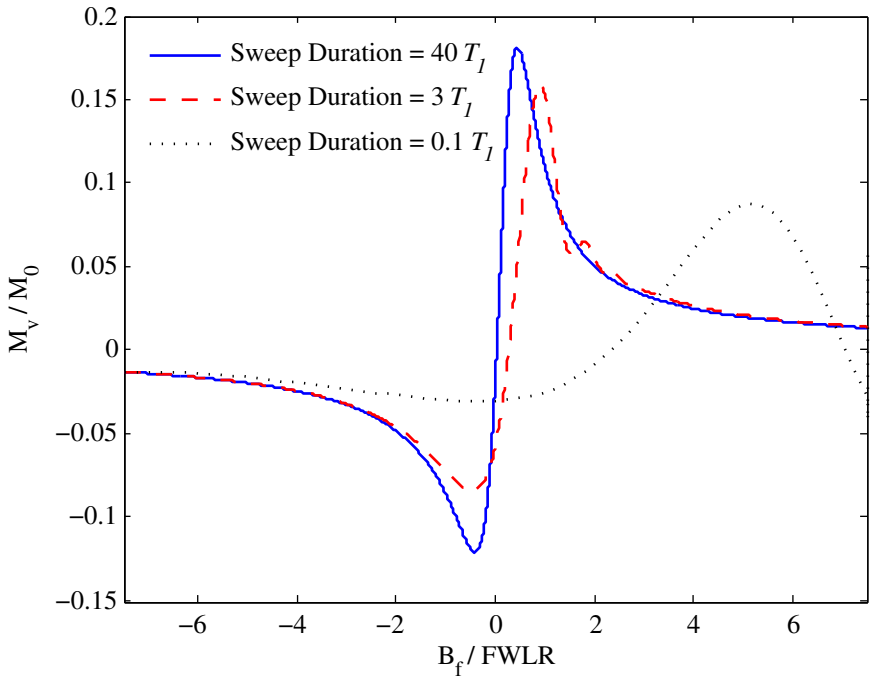

Figure 4.6. Response of M_v from full nonlinear dynamics model for field sweeps $40T_1$, $3T_1$, and $0.1T_1$.

The results of Figure 4.6 indicate that when field fluctuations B_f change quickly with respect to T_1, the mapping from B_f to M_v make it difficult to regulate B_f by regulating M_v. The remainder of this section studies the effects of such a B_f on a dispersion lock using measurements of M_v as indirect estimates of B_f. This study is conducted in simulation and experiment to verify the observed results.

Dispersion locks typically use a proportional plus integral plus derivative (PID) compensator to regulate M_v. The Tecmag lock NMR console discussed in subsection 3.4.2 is a dispersion lock which uses a PID compensator. Thus a dispersion lock using PID compensation can be studied to understand the limitations of them in powered magnets.

The dispersion lock was studied using one type of disturbance field fluctuation over two time scales. The chosen disturbance field was a ramp disturbance field, which is similar to field sweep disturbance shown in Figure 4.4. The difference between the ramp and field sweep disturbance is that the ramp changes from 0 to 7.5 times the FWLR, as opposed to -7.5 to +7.5 times the

FWLR in the case of the field sweep. The ramp field disturbance was chosen to change over $3T_1$ and $0.1T_1$ to observe the dispersion lock performance when the field fluctuations are fast compared to T_1.

Simulation results of the dispersion lock using PID control was obtained using the same NMR parameters listed in Table 4.1. The control gains were tuned through experimental testing, where using the Tecmag lock it was found that a proportional gain (P) of 100 and an integral gain (I) of 400 would allow the lock to regulate M_v close to zero for no disturbance field fluctuations. When comparing simulation to experiment, it was estimated that the voltage measurement representing M_v is 2.1×10^6 times greater than the true value of M_v. Thus to compare simulation and experiment the control gains P and I where chosen as 2.1×10^{-4} and 8.4×10^{-4} in simulation, which is 400 and 100 divided by 2.1×10^6.

Before discussing the simulation results, a brief statement is made about tuning controller gains. If it was found that a dispersion lock using indirect regulation could work on a powered magnet, then this method of tuning gains and determining scale factors of M_v would not be recommended for control design. Instead a control design should be developed based on identified models from an appropriate system identification algorithm. However, as is being shown in this section, dispersion locks will be very difficult to implement in powered magnets. Therefore, tuning control gains and determining scale factors is acceptable here in order to demonstrate that a dispersion lock is insufficient for powered magnets.

The simulation results for a ramp disturbance field changing over $3T_1$ is shown in Figure 4.7. The horizontal axis shows time normalized by T_1 and the vertical axis shows field normalized by FWLR. The ramp disturbance field, represented by the solid line, begins at $1T_1$ and changes from 0 to 7.5 times the FWLR from $1T_1$ to $4T_1$. During the ramp disturbance field, the changes in M_v are computed from the dynamics model and fed as an error signal to the compensator. The compensator generates a correction signal which is converted to a correction field B_c to regulate M_v. The correction field generated by the compensator is inverted for convenience and

shown with the dashed line. In this case the inverted correction field $-B_c$ matches the ramp disturbance field, implying that B_f is regulated to zero. For a field fluctuation that varies over $3T_1$, the PID compensator regulates B_f to zero by regulating M_v to zero.

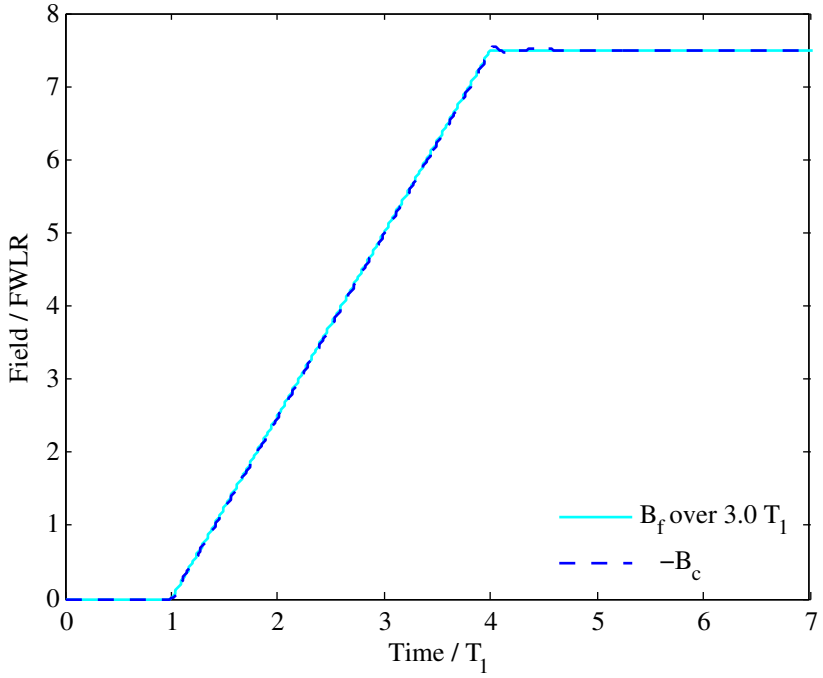

Figure 4.7. Simulation results of dispersion lock implementing PID control, ramp disturbance field rising over $3T_1$.

The simulation results in Figure 4.7 shows that a dispersion lock performs well for a ramp disturbance field changing over $3T_1$. In order to test the performance of this FFL for field ramp disturbance which changes quickly with respect to T_1, the same simulation was executed with a ramp disturbance field changing over $0.1T_1$ instead of $3T_1$. The results of this simulation is shown in Figure 4.8 where the horizontal axis is time normalized by T_1 and the vertical axis is field normalized by FWLR.

In contrast to the results of Figure 4.7, these results reveal that as the field disturbance change over $0.1T_1$, the inverted correction field does not match the disturbance field well. The FFL cannot properly regulate the ramp field disturbance when it changes quickly with respect to T_1. This may not come as a surprise when considering M_v response to a field sweep changing over $0.1T_1$ as shown in Figure 4.6. Recall that the results in this figure showed that when a field disturbance sweep changes over $0.1T_1$, there are multiple points where M_v crosses the B_f axis. This effect precludes the compensator from properly regulating M_v to zero when B_f changes over $0.1T_1$, and consequently the field ramp disturbance B_f is not regulated to zero. Once the field ramp is over at $1.1T_1$, the field is constant and the dispersion lock regulates it to zero.

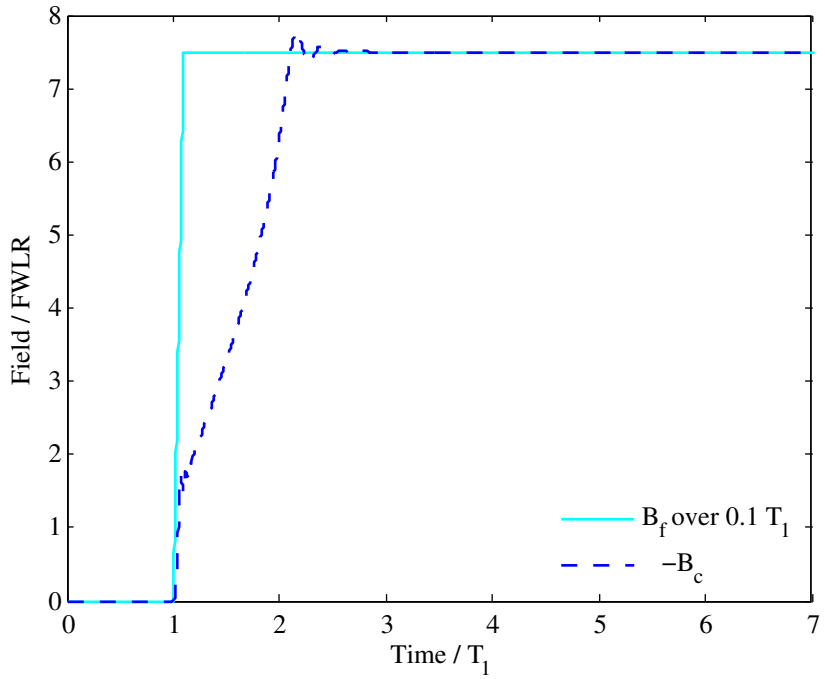

Figure 4.8. Simulation results of indirect FFL implementing PID control, ramp disturbance field rising over $0.1T_1$.

The results of these two dispersion lock simulations are compared in Figure 4.9. The field error $(B_f + B_c)$ normalized by FWLR is plotted against time normalized by T_1. The normalized field error is plotted for a ramp disturbance field changing over $3T_1$ and $0.1T_1$ in the solid and dashed

lines respectively. These results show that while the field error is very small for a disturbance field changing over $3T_1$, the field error is almost 6 times the FWLR, or approximately 140 mG for a disturbance changing over $0.1T_1$. In NMR spectroscopy, 140 mG corresponds to almost a 600 Hz shift in the Larmor frequency of hydrogen nuclei, which is unacceptable.

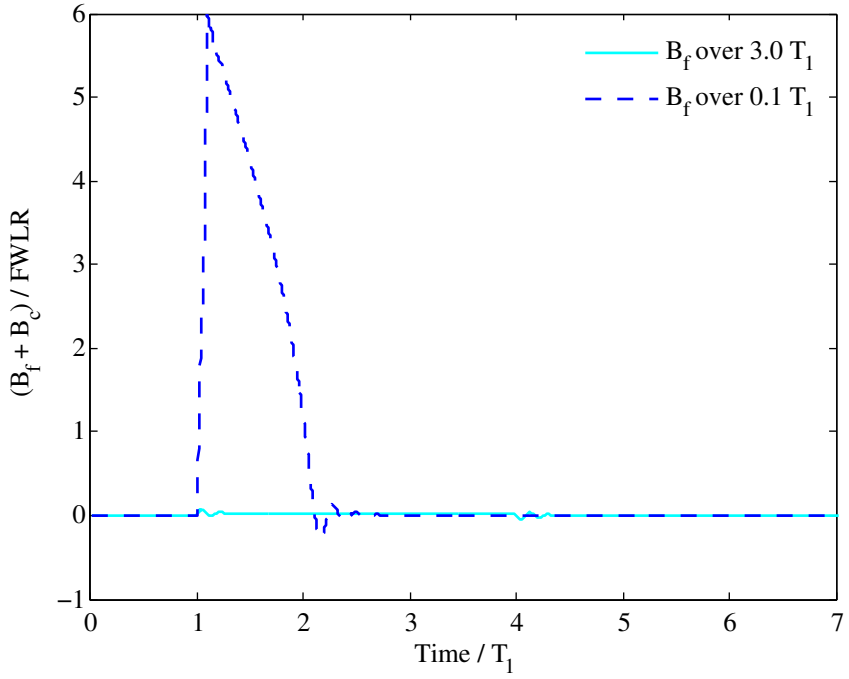

Figure 4.9. Field error determined from simulation for ramp disturbance field over $3T_1$ and $0.1T_1$.

In order to verify the results shown in these simulations, a dispersion lock which regulates M_v using PID control was studied in experiment. The Tecmag lock NMR console described in subsection 3.4.2 is a dispersion lock which regulates M_v. Just as in simulation, the performance of this FFL will be studied in the presence of the same two ramp field disturbances.

The experimental setup for evaluating the performance of the Tecmag lock FFL is shown in Figure 4.10. These experiments were implemented on a 7.1 T superconducting magnet, where field fluctuations are inherently small. In this way, the drive coil can be used to superimpose the desired ramp field disturbances on the B_0 without interference from other fluctuations. The correction coil, disturbance coil, current amplifier, Bruker NMR probe, and Tecmag lock where

all described in Sections 2.2 and 3.4. The NMR sample contains 90 % deuterium and 10 % water with 50 mM copper sulfate doping.

The dSPACE DS1104 controller board is a real-time digital signal processor (DSP) that is programmed using the Simulink block diagram environment in Matlab. Additional software provided by dSPACE generates C code based on the block diagram and transfers it to the DSP processor on the controller board. The dSPACE board includes eight analog to digital converters (ADC), eight digital to analog converters (DAC), and 20 digital input/output lines. The ADCs consist of eight total channels, four 16 bit and four 12 bit. These are used to sample, or digitize analog signals so they can be processed by the DSP. After processing the sampled-data signals, the DACs are used to convert the sampled-data output signals to analog signals for use in analog devices like the current amplifier and correction coil. The DACs consist of eight channels that are all 16 bit. The 20 digital input/output lines provide binary signals, which can be used to trigger devices external to the dSPACE.

The signal generator for this experiment was programmed in dSPACE and provides a disturbance voltage V_f to one channel of a current driver. The output current of this driver is applied to the disturbance coil, which superimposes a disturbance field fluctuation onto the magnet's 7.1 T field. The P and I gains of the Tecmag lock where chosen as 100 and 400 because this allowed the lock to regulate M_v close to zero for no field fluctuations. The pulse repetition rate is fixed by the Tecmag lock at 2 kHz. The Tecmag lock measures M_v in response to this pulse sequence and the PID compensator generates a correction voltage V_c to regulate M_v. Similar to the disturbance voltage, this voltage is converted to correction field using a current driver and correction coil. The disturbance signal and correction signals were recorded using dSPACE. As in the case with the simulations, if the inverted correction field matches the disturbance field then the dispersion lock is successfully regulating B_f.

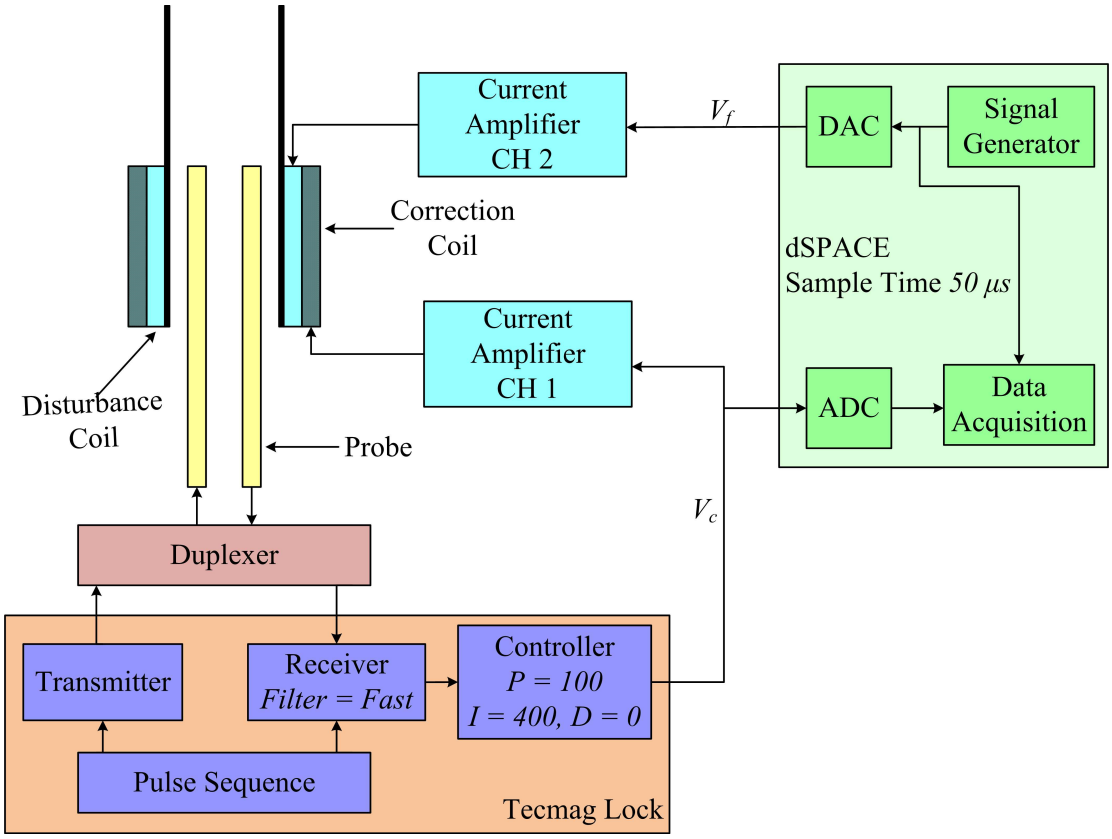

Figure 4.10. Experimental setup for measuring Tecmag dispersion lock response to field disturbances.

The same two ramp disturbance fields from the simulations were chosen for these experiments. The recorded disturbance voltage V_f and correction voltage V_c was converted to field using the DC gain of the current amplifier in series with the drive coil. Recall from Section 2.3 that this gain was measured by determining the shift in NMR Larmor frequency to a step field change. The results of the this experiment for ramp disturbance field changing over $3T_1$ is shown in Figure 4.11. As in the simulations, the horizontal axis shows time normalized by T_1 and the vertical axis shows field normalized by FWLR. The disturbance field, represented by the solid line, is compared to the inverted correction field for both simulation (dashed line) and experiment (dotted line).

The results in Figure 4.11 are consistent with the simulations during the $3T_1$ ramp time. When the field is changing over $3T_1$, the dispersion lock is able to regulate M_v and thus regulate B_f. The experimental results do show that there is some error after time $4T_1$ between the disturbance field and correction field. This could be due to some other field fluctuation besides the applied disturbance present in the magnet. Note that the measurement of V_f and hence B_f is the predicted field disturbance based on the applied voltage to the disturbance coil. It was not measured with a sensor inside the magnet, so any field fluctuations present in this magnet without an applied disturbance are not taken into account.

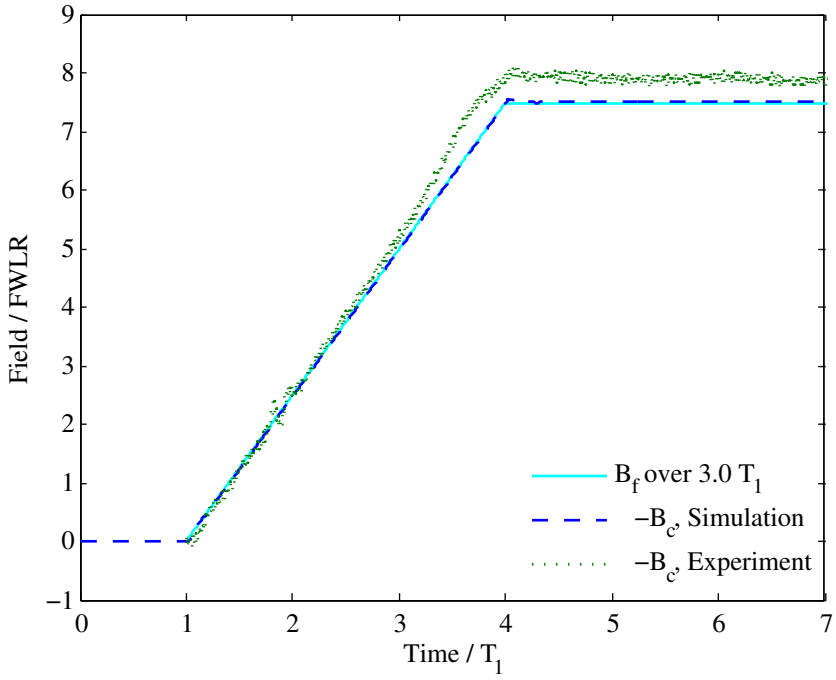

Figure 4.11. Experiment and simulation results of dispersion lock implementing PID control, ramp disturbance field rising over $3T_1$.

Figure 4.12 shows the results of the this experiment for ramp disturbance field changing over $0.1T_1$, where the axes are the same as the previous figure. The disturbance field is again compared to the inverted correction field for both simulation and experiment. The simulations and experiment are consistent during the $0.1T_1$ ramp time. Similar to the $3T_1$ ramp field disturbance

case, there is a error between experimental disturbance and correction field after $1.1T_1$ when the disturbance is constant. This may also be attributed to any small field fluctuations present in the magnet. As in the simulations, the dispersion lock cannot regulate B_f well when it changes quickly with respect to T_1.

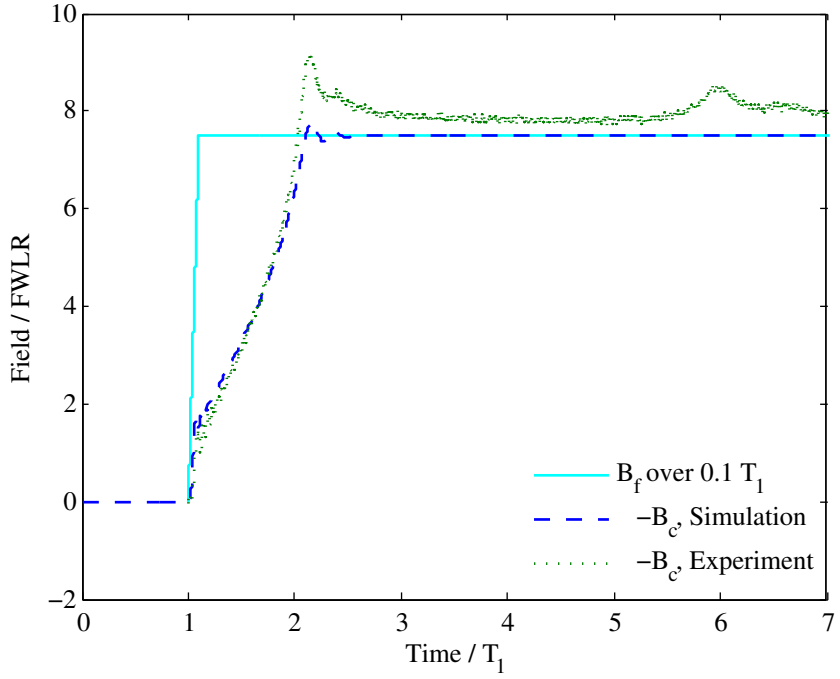

Figure 4.12. Experiment and simulation results of dispersion lock implementing PID control, ramp disturbance field rising over $0.1T_1$.

The results of these two dispersion lock experiments are compared in Figure 4.13. As in the simulations, the normalized field error is plotted against time normalized by T_1 for the two ramp disturbance fields. The field error is much less than the FWLR and is within 20 mG for a disturbance field changing over $3T_1$. In contrast, this error is greater than 6 times the FWLR and is almost 150 mG for a disturbance changing over $0.1T_1$. A 20 mG field change corresponds to 82 Hz shift in Larmor frequency of hydrogen nuclei, which is acceptable for NMR spectroscopy. However, a 150 mG field change corresponds to a 616 Hz shift in Larmor frequency, which is unacceptable for NMR.

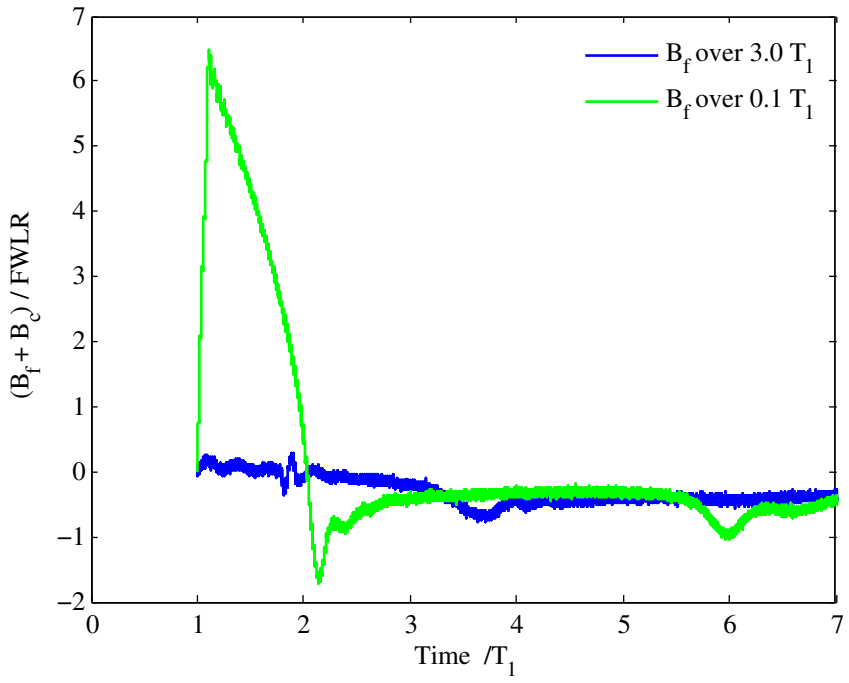

Figure 4.13. Field error from experimental measurement for ramp disturbance field over $3T_1$ and $0.1T_1$.

The simulation and experimental results presented in this section show that a dispersion lock using PID control cannot regulate field fluctuations changing quickly with respect to T_1. It may be possible to improve the dispersion lock performance by modifying the compensator. For the PID compensators used in dispersion locks, increasing the gains may cause the system to be unstable, and decreasing the gains may reduce the rise time of the inverted correction field, leading to larger field error during a ramp disturbance. Additionally a different compensator, most likely nonlinear, could be designed for the dispersion lock. However, the time constants T_1 and T_2^* would need to be known well because the full nonlinear NMR dynamics model depends on theses parameters. These time constants depend on the NMR sample and are often not precisely known.

The limitations of dispersion locks discussed in this section arise because they use indirect measurements to reduce field fluctuations. These dispersion locks regulate M_v to reduce B_f, which is sufficient as long as B_f changes slowly with respect to T_1. It was shown in this section

that when B_f changes quickly with respect to T_1 the nonlinear dynamics model mapping B_f to M_v makes it difficult to reduce B_f by regulating M_v. These limitations can be overcome by directly estimating B_f from FID signal frequency. As changes in FID frequency is proportional to B_f, the resulting mapping from B_f to estimation output will be linear and explicitly independent of T_1 and T_2^*, which simplifies the compensator design. The following chapter discusses methods for directly estimating B_f from FID signal frequency without explicit knowledge of T_1 and T_2^*.

Chapter 5

Direct Estimation of Field Fluctuations using NMR

Chapter 4 showed that dispersion locks using $M_v(t)$ to indirectly estimate $B_f(t)$ are limited in powered magnets because $B_f(t)$ changes quickly with respect to T_1. This can be overcome by estimating $\omega_f(t)$ from an FID signal, which is a direct estimate of $B_f(t)$ because $\omega_f(t)$ is proportional to $B_f(t)$. This approach also can provide a direct estimate of $B_f(t)$ which is explicitly independent of NMR time constants T_1, T_2, and T_2^*. This chapter discusses new approaches for directly estimating $B_f(t)$ from FID signals without explicit knowledge of T_1, T_2, and T_2^*.

Section 5.1 studies different methods for directly estimating $B_f(t)$ from FID signals and discusses the tradeoffs amongst these methods. Section 5.2 shows experimental comparison of these methods to determine which method can be chosen as a sensor for a direct FFL. Section 5.3 provides an assessment of the chosen estimation method, showing considerations for realizing the estimating method and the known limitations of this method.

5.1 Methods for Direct Estimation

Section 4.1 reviewed several FFLs which directly estimate $B_f(t)$ but only one such direct FFL was demonstrated in a powered magnet. This design used a frequency counter to directly measure $\omega_f(t)$ and was explicitly independent of NMR time constants [59]. The magnet used to verify this approach was a powered magnet using a superconducting coils with an external power supply.

This approach has three limitations when considering application to powered magnets which use resistive coils like the Keck or SCH magnets. First, resistive coils have much smaller inductance and require larger operating current. For example, the SCH has an inductance of 236 mH and requires an operating current of 19 kA. Conversely, the powered magnet used by Takahashi *et al.* has an inductance 210 H and an external power supply operating at 71.2 A. The inductance of this magnet is three orders of magnitude larger than the SCH and the operating current is three orders of magnitude smaller than the SCH. Both these factors inherently reduce higher frequency fluctuations, and so the effects of these fluctuations on the direct FFL are not significant. Subsection 5.3.3 demonstrates that higher frequency fluctuations present in powered magnets with resistive coils will alias and thus have a significant impact on a direct FFL. Therefore aliasing must be considered when designing a direct FFL for powered magnets with resistive coils.

Second, this approach estimates $\omega_f(t)$ from a signal representing the transverse magnetization $M_{uv}(t)$. If instead signals representing the quadrature components $M_u(t)$ and $M_v(t)$ are measured, then more options are available for developing direct estimation methods. For example, the phase $\phi(t)$ can be computed from $M_u(t)$ and $M_v(t)$, which can be used to estimate $\omega_f(t)$. Additionally, the frequency of $M_u(t)$ and $M_v(t)$ can be estimated independently, providing two frequency estimates of the FID signal which can be combined to improve estimation accuracy. The direct estimation methods shown in this section use $M_u(t)$ and $M_v(t)$ to estimate $\omega_f(t)$. Note that the NMRkitII console described in subsection 3.4.2 provides real–time access to $M_u(t)$ and $M_v(t)$, which can be supplied to the dSPACE for digital signal processing. Therefore these

estimation methods using $M_u(t)$ and $M_v(t)$ can be realized using the available instrumentation.

Third, this approach does not consider system dynamics when designing the compensator. Using system dynamics allows the control designer to develop and test compensator designs in frequency range of interest. The degree of stability and performance of the compensator design can be quantified when system dynamics are known.

Given the limitations of this previous method, this section investigates three different methods for directly estimating $B_f(t)$ from the quadrature components $M_u(t)$ and $M_v(t)$ of a FID signal. As a starting point, this analysis considers estimation of a field fluctuation $B_f(t)$ that changes slowly over a long period of time. In this case $B_f(t)$ and hence $\omega_f(t)$ can be assumed constant during the acquisition of a single FID. The end of this section discusses how these methods are affected when this assumption is not valid.

The complex signal representation of an FID was introduced in Section 3.2. This represents the NMR response to a single RF pulse providing a tip angle θ close to $\pi/2$. The expression for the complex FID signal is

$$\begin{aligned} M_{uv}(t) &= M_u(t) + jM_v(t) \\ &= Ae^{-t/T_2^*}e^{j\phi(t)}. \end{aligned} \tag{5.1}$$

The NMR time constant T_2^* is defined by the NMR sample, and is the time constant which describes the decay of the transverse magnetization vector $\vec{M}_{uv}$. The angle $\phi(t)$ is the phase angle between $\vec{M}_{uv}$ and the u axis as shown in Section 3.3.

The expression for phase angle $\phi(t)$ from Section 3.3 assumes the initial phase angle ϕ_0 and baseband frequency ω_b are zero. In a NMR experiment, these parameters may be non-zero, in which case the expression for phase angle can be rewritten as

$$\phi(t) = \phi_0 + \omega_b t + \int_0^t \omega_f(\tau)d\tau = \phi_0 + \omega_b t + \int_0^t \gamma B_f(\tau)d\tau, \tag{5.2}$$

where ϕ_0 is the initial phase angle between the u axis and the vector $\vec{M}_{uv}$ at a time just after the RF pulse. When B_f is constant, equation 5.2 becomes

$$\phi(t) = \phi_0 + (\omega_b + \omega_f)t, \tag{5.3}$$

which results in following expression for $M_{uv}(t)$

$$M_{uv}(t) = Ae^{j\phi_0}e^{-t/T_2^*}e^{j(\omega_b t + \omega_f t)}. \tag{5.4}$$

The expressions in equations 5.3 and 5.4 were used to develop the three methods for directly estimating B_f. Each method uses different techniques to estimate ω_f, which can be used to derive B_f. The methods developed are defined here as FFT, level interpolation, and phase least-squares (LS) fit.

The FFT method estimates ω_f from changes in the frequency at which the FFT magnitude peak occurs. Consider the Fourier transform of equation 5.4

$$M_{uv}(\omega) = \frac{Ae^{j\phi_0}}{j(\omega - (\omega_b + \omega_f)) + 1/T_2^*}. \tag{5.5}$$

Because ω_b is fixed, changes in the peak of the Fourier transform are estimates of ω_f, which can be used to derive B_f. The Fourier transform in equation 5.5 is computed using an approximation known as the Fast-Fourier-Transform (FFT) so this method is defined as the FFT method.

The disadvantage of the FFT method is that zero padding is required to improve resolution of the FFT calculation. Ultimately, the estimation method will be implemented in real–time using the dSPACE controller board, where the minimum sample period for this device is 20 μs, corresponding to a 50 kHz sample rate. For a typical FID acquisition time, this implies there are a limited number of points measured for each FID.

For example, consider an FID acquired for 2.5 ms at a sample rate of 50 kHz. Then only

500 points of the signal is acquired for estimation. A signal length of 500 points with a sample rate of 50 kHz gives a FFT resolution of only 100 Hz. This means that ω_f can be estimated only to within 100 Hz, which is inadequate for feedback control. Thus zero padding is necessary in the FFT calculation to improve resolution. Zero padding requires more computation time to determine the FFT, which is undesirable when implementing the estimation in real–time. The advantage of the FFT method is that all FID data acquired is used to estimate ω_f. As long as FID SNR is adequate, this can be viewed as an advantage as no data is discarded. This is different than the level interpolation method to be discussed next.

The second method for estimating ω_f, level interpolation, is an extension of the frequency counter methods introduced in Section 4.1 [58, 59]. Figure 5.1 demonstrates the operation of a frequency counter [69]. A hysteresis window is defined with the threshold levels E_{ON} and E_{OFF}. When the sinusoidal input signal transitions from threshold levels E_{OFF} to E_{ON}, a Schmitt trigger detects the transition and outputs a pulse signal which changes from a low to high state. Similarly, when the signal transitions from E_{ON} to E_{OFF} the output of the Schmitt trigger changes from a high to low state. As the input signal is periodic, the resulting output of the Schmitt trigger is also periodic with a period equivalent to the input signal. The period of the Schmitt trigger output is inverted to obtain a measurement of the input signal frequency.

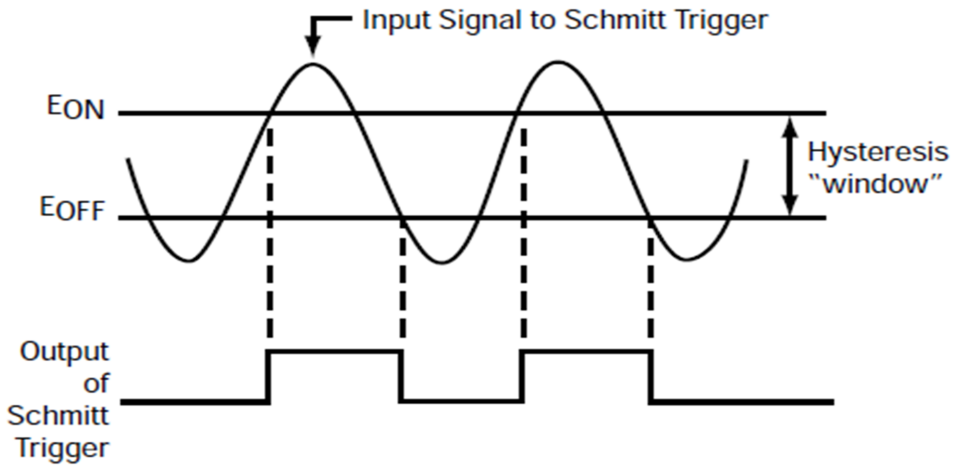

Figure 5.1. Frequency counter operation [69].

The level interpolation method was developed to extend the principle of a frequency counter to sampled-data measurements of the quadrature signals $M_u(t)$ and $M_v(t)$. The frequency counter assumes an analog input signal and only provides one frequency measurement for each cycle of the input signal. The level interpolation method uses a sampled-data input signal to determine multiple frequency estimates for each cycle of the input signal. For this development, a frequency estimate must be determined from a sampled-data signal as the estimator will be implemented on the dSPACE controller board. Furthermore, the level interpolation method was designed to provide more frequency estimates per cycle than the frequency counter to improve estimation accuracy.

For level interpolation, when the sampled-data FID signals transition thru a threshold level, the nearest data point is interpolated to the threshold using a linear approximation between adjacent data points. The time between interpolated points can be used to estimate the signal period and frequency. Figure 5.2 demonstrates level interpolation for a simulated sampled-data signal M_u.

When M_u transitions thru the threshold level Tn, the nearest data point is interpolated to Tn using a linear approximation between adjacent data points. The same is done for threshold level Tn. The open circles are sampled-data points of M_u and the solid triangles are the points from interpolating to the threshold. The time between interpolated points can be used to estimate the signal period and frequency.

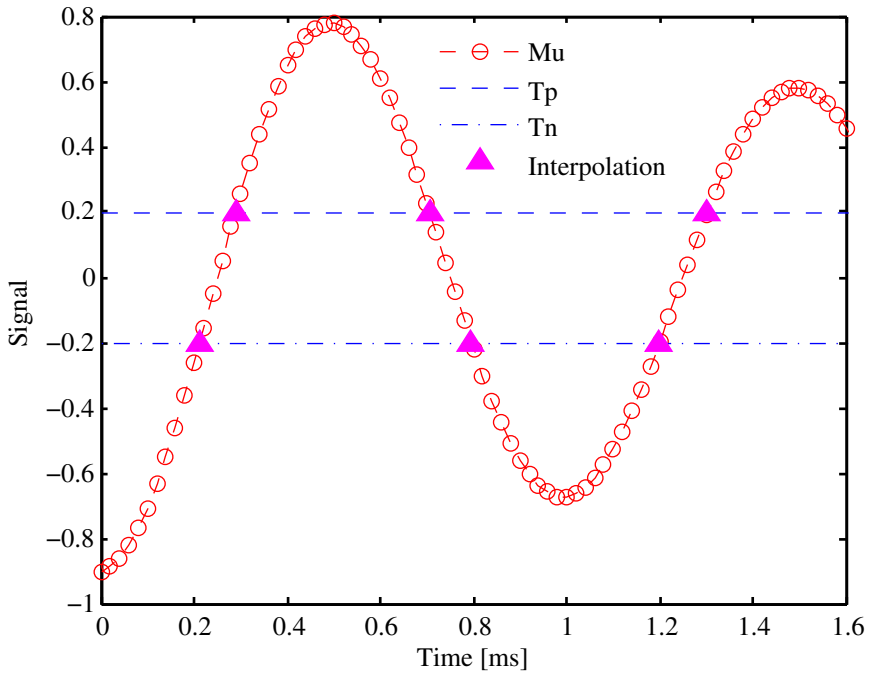

Figure 5.2. Demonstration of level interpolation for a simulated sampled-data M_u.

The level interpolation method gives two frequency estimates per cycle, which is one more estimate per cycle than the frequency counter. In the case of a FID signal, there are two sampled-data signals M_u and M_v that can be used to estimate frequency, and level interpolation provides four frequency estimates per cycle. These four estimates can be averaged to give a more accurate frequency estimate then when using a single estimate per cycle. In addition, if more threshold levels are used then more estimates per cycle can be determined at the expense of computation time. When this method is applied to multiple FID signals, changes in the average frequency estimate of consecutive FIDs represent an estimate of ω_f.

The advantage of the level interpolation method is that it will take less computation time than the FFT method because there is no zero padding necessary. Another advantage of level interpolation is it provides a means for ignoring portions of the FID signal data that has poor SNR. By appropriately choosing the threshold levels above the noise floor of the FID, the estimation method will only be applied to FID data above the noise floor. This is not the case for

the other two estimation methods which use all FID signal data. If only noisy measurements of the FID signals are available, then the level interpolation may be the best choice.

A disadvantage of this method is not all FID data acquired is used to estimate ω_f when FID SNR is adequate. This is different than the FFT method which uses all the data. Another disadvantage of this method is that the input FID signal must transition through the levels Tp and Tn a sufficient number of times to give a frequency estimate. In the level interpolation method, the FID signal must transition from Tp to Tn two times and from Tn to Tp two times, which implies that two complete cycles of the FID signal with amplitudes above the threshold levels must be observed for a proper frequency estimate. Any method based on threshold levels like level interpolation assumes there are full cycles present in the FID signal which is not guaranteed.

The third method for estimating ω_f is phase LS fit, which approximates the frequency of the FID signal using a least-squares fit to the phase angle $\phi(t)$. The expression for the phase angle $\phi(t)$ in equation 5.3 is a first order polynomial with slope $\omega_b + \omega_f$. It is desirable to estimate this slope using a least-squares fit to this polynomial. This is because the LS fit reduces the effect of error due to measurement noise on the estimate [70]. The derivative of the phase angle could also be used but was not preferable because derivative operations accentuate high frequency noise.

A brief description of the LS fit algorithm applied to the phase angle in equation 5.3 is now provided. Suppose the FID signal is sampled at time t_k where k is an integer from 0 to $N-1$, and the phase angle is computed at each time t_k, denoted as $\phi(k)$. There is error in each phase computation because it is derived from noisy measurements of the FID signal. If the error in the phase computation $\phi(k)$ is denoted $e(k)$, then each of the N phase computations satisfy

$$\begin{aligned} \phi(0) &= a_0 + a_1 t_0 + e(0) \\ &\vdots \\ \phi(N-1) &= a_0 + a_1 t_{N-1} + e(N-1), \end{aligned} \tag{5.6}$$

where a_0 and a_1 are the true parameters ϕ_0 and $\omega_b + \omega_f$ respectively. The LS fit determines estimates $\hat{a}_0, \hat{a}_1$ of the true parameters a_0 and a_1 that minimize the squared error in these expressions. The set of expressions in 5.6 can be written in matrix form as

$$\Phi = F\Theta + E, \tag{5.7}$$

where

$$\Phi = \begin{bmatrix} \phi(0) \\ \vdots \\ \phi(N-1) \end{bmatrix},$$

$$F = \begin{bmatrix} 1 & t_0 \\ \vdots & \vdots \\ 1 & t_{N-1} \end{bmatrix}$$

$$\Theta = \begin{bmatrix} a_0 \\ a_1 \end{bmatrix}, \text{ and.}$$

$$E = \begin{bmatrix} e(0) \\ \vdots \\ e(N-1) \end{bmatrix}.$$

The squared error can be expressed as

$$\begin{aligned} J(\Theta) &= \sum_{k=0}^{N-1} e^2(k) \\ &= E^T E \\ &= (\Phi - F\Theta)^T(\Phi - F\Theta), \end{aligned} \tag{5.8}$$

where it has been shown in the text by Ljung [70] that the vector $\hat{\Theta}$ that minimizes the squared

error $J(\Theta)$ is

$$\begin{aligned} \hat{\Theta} &= (F^T F)^{-1} F^T \Phi \\ &= (F^T F)^{-1} F^T (F\Theta + E) \\ &= \Theta + (F^T F)^{-1} F^T E. \end{aligned} \tag{5.9}$$

For the phase angle in equation 5.7, $\hat{\Theta}$ is a column vector containing the elements $\hat{a}_0, \hat{a}_1$, which are the least-squares estimates of the true parameters a_0 and a_1. Comparing equations 5.6 to 5.3, it can be seen that $\hat{a}_1$ is an estimate of the frequency $\omega_b + \omega_f$. So with ω_b fixed, changes in $\hat{a}_1$ is an estimate of ω_f.

When computing the phase angle in equation 5.7, each element of the error vector $e(0)$, $e(1)$, ..., $e(N-1)$ can be modeled as a independent random variable with zero mean and variance λ_0. It was shown in the textbook by Ljung [70] that in this case the expected value of $\hat{\Theta}$ is

$$E[\hat{\Theta}] = \Theta, \tag{5.10}$$

which means the estimate is unbiased. Additionally, the covariance matrix of $\hat{\Theta}$ was shown to be

$$Cov[\hat{\Theta}] = \lambda_0 (F^T F)^{-1}, \tag{5.11}$$

where λ_0 can be approximated by

$$\lambda_0 \approx \frac{1}{N-2} E^T E. \tag{5.12}$$

Thus as N gets large, λ_0 gets small, and the diagonal elements of $Cov[\hat{\Theta}]$, which represent the variance of $\hat{\Theta}$, get small.

The advantage of the phase LS fit method is the effect of measurement noise on the estimate is reduced. This is because this method minimizes the squared error in the NMR signal phase.

Another advantage of this method is that the parameter estimates $\hat{a}_0, \hat{a}_1$, and hence ϕ_0 and $\omega_b + \omega_f$, are derived using simple matrix multiplications. As such this method will take less computation time than the FFT method when deriving estimates of ω_f. The disadvantage of this method is that N must be large enough so that the variance of $\hat{\Theta}$ is small enough to provide an accurate estimate of ω_f.

When comparing the three methods discussed in this section, there are some common advantages and disadvantages. The level interpolation and phase LS fit methods have the advantage of taking less processing time than the FFT method. The phase LS fit and FFT methods have the advantage of using all the measured FID signal data where the level interpolation only uses certain points of this data. The common disadvantage of all three methods is there must be a sufficient number of FID points acquired to provide an accurate estimate.

Recall that the assumption in developing these three estimation methods is that $B_f(t)$ is constant during a single FID acquisition. Now consider the case when $B_f(t)$ is not constant during this time interval. For the FFT method, this will distort the lineshape of the magnitude spectra, and the center of mass or centroid of the magnitude spectra can be computed instead of peak frequency to estimate $\omega_f(t)$. In the time domain, the frequency $\omega_f(t)$ will modulate the FID signal frequency so that it will have the form of a chirp signal. The level interpolation produces an estimate which is the average of $\omega_f(t)$. As long as $\omega_f(t)$ changes gradually, and provides only moderate frequency modulation, then this estimate should still be adequate.

The Phase LS fit method can be viewed as estimating $\omega_f(t)$ from the derivative of $\phi(t)$. If $B_f(t)$ is not constant, then the derivative of the phase in equation 5.3 is

$$\frac{d\phi(t)}{dt} = \omega_b + \gamma B_f(t). \tag{5.13}$$

The computation of the phase derivative in equation 5.13 will be noisy in an experimental system. In order to reduce the effects of noise, the average of $d\phi(t)/dt$ can be computed. For the phase

LS fit, this average is computed using a least-squares algorithm. Therefore in the case where $\omega_f(t)$ is not constant during a single FID, the phase LS fit would estimate the average of $\omega_f(t)$.

For all three methods, the effects of $B_f(t)$ changing with respect to time can be mitigated from the estimate by some form of averaging. Recall from Section 4.3 that dispersion locks cannot use M_v to estimate B_f when it changes quickly with respect to T_1. This is because M_v is not proportional to B_f under these conditions. Therefore averaging M_v will not improve performance of the dispersion lock as M_v will still not be proportional to B_f. The methods provided in this section have the significant advantage over dispersion locks as they use averaging to mitigate the effect of B_f which change quickly with respect to T_1.

The following section evaluates these three methods for estimating ω_f in further detail. These methods will be verified by applying them to FID data collected on the 7.1 T superconducting magnet. The performance of these methods will be compared in order to determine which method will be used for NMR feedback control.

5.2 Experimental Comparison

Now that three direct estimation methods have been presented in Section 5.1, one of these methods must be chosen as a sensor for a direct FFL designed to reduce lower frequency fluctuations. As such, the FFT, level interpolation, and phase LS fit methods were compared by observing how well they estimate lower frequency fluctuations. This section describes an experiment designed to evaluate how well each method estimates such a fluctuation. These experimental results are used to choose a direct estimation method as a sensor for a direct FFL.

The 7.1 T superconducting magnet was used for this experiment because field fluctuations are relatively constant in this magnet. This way a known disturbance field fluctuation can be superimposed on the magnetic field without interference from other fluctuations. A series of FID signals were acquired using this magnet in the presence of a lower frequency fluctuation. The

estimation methods were then applied to the FID data off-line to evaluate their performance.

The disturbance field applied while acquiring the FID signals is shown in Figure 5.3. The leftmost vertical axis shows the applied disturbance field $B_f(t)$ in mG, and the rightmost vertical axis shows the resulting change in FID signal frequency $\Delta f(t)$ in Hz. The frequency $\Delta f(t)$ is the frequency $\omega_f(t)$ converted to Hz, so it is equivalent to $\omega_f(t)/(2\pi)$. The amplitude of $B_f(t)$ was chosen to shift the FID signal frequency by 200 Hz (6.62 ppm), which was a small percentage of the hydrogen nuclei Larmor frequency of 300 MHz. The period T_d of the disturbance field was chosen as 5 seconds to evaluate estimator performance for lower frequency fluctuations.

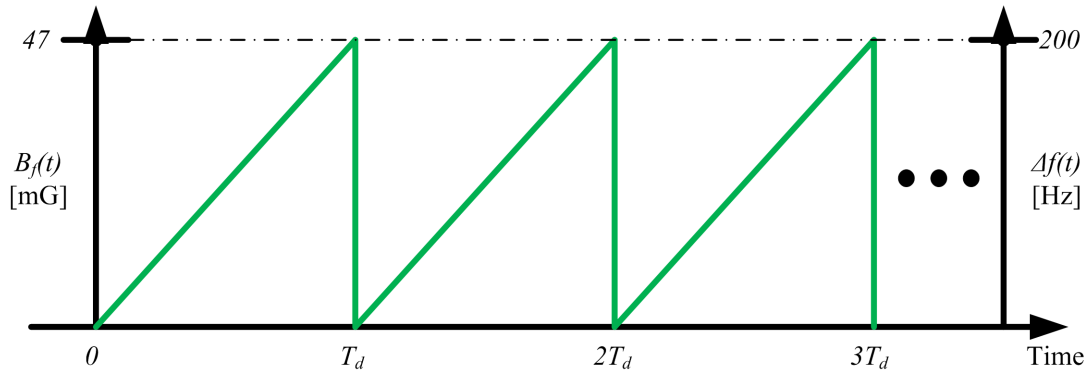

Figure 5.3. Periodic ramp disturbance field, $T_d = 5$ sec, chosen max $\Delta f = 200$ Hz.

The sample used for this experiment was 90 % deuterium and 10 % water with 50 mM copper sulfate doping. The RF transmit signal frequency was chosen near 300 MHz, so as to excite hydrogen nuclei of the sample at 7.1 T. The NMR time constant T_1 and T_2^* were measured as 26 ms and 3.43 ms respectively.

Figure 5.4 shows the pulse sequence used for this experiment, with the quadrature components $M_u(t)$ and $M_v(t)$ indicated. The pulse period T was chosen as 100 ms, which is larger than $3T_1$, allowing for the magnetization to relax to thermal equilibrium in between pulses. The RF pulse width was chosen as 20 μs, which is the smallest sample period of the dSPACE controller board used to gate this RF pulse. The RF pulse amplitude was adjusted by to give a tip angle θ close to $\pi/2$ so that the FID signals would have good SNR. The signals $M_u(t)$ and $M_v(t)$ where acquired

in response to 100 consecutive RF pulses over a total time interval of 10 seconds. This was chosen so that FID signals were observed over two periods of the applied disturbance field.

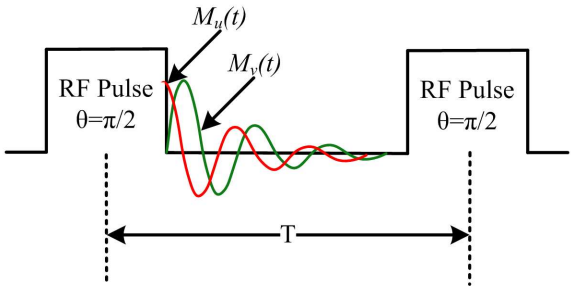

Figure 5.4. Pulse sequence used to generate FID signals, $M_u(t)$ and $M_v(t)$ are the quadrature components of the FID response, $T = 100$ ms.

The setup for this experiment including instrumentation is shown in the block diagram of Figure 5.5. The NMR console and probe chosen was the NMRkitII and the Bruker probe, which are described in Section 3.4. The Bruker probe was used because it has a RF channel tuned to the 300 MHz Larmor frequency of hydrogen nuclei. The NMRkitII was chosen because it provides real–time access to the analog signals $M_u(t)$ and $M_v(t)$ as opposed to just $M_v(t)$. The dSPACE controller board generates a ramp signal voltage $V_f(t)$ as an input to an actuator comprised of a current amplifier and disturbance coil. This actuator superimposes a field fluctuation $B_f(t)$ onto a 7.1 T field of the superconducting magnet.

While generating the ramp disturbance signal, digital input/output lines of dSPACE are used to simultaneously generate the digital gate signals *TX Gate* , *RX Gate* , and *Blank Gate* . Each gate signal has a high and low state. As described in Section 3.4, these gate signals are used to control the pulse sequence timing of the NMRkitII and power amplifier, producing a pulse sequence like that in Figure 5.4. The quadrature components $M_u(t)$ and $M_v(t)$ of the FID signal, generated by the NMRkitII, are recorded as sampled-data signals using dSPACE. These signals are sampled at a period of 20 μs over a time interval of 2.5 ms. The 20 μs sample period was chosen because it is the smallest sample period of the dSPACE, and the 2.5 ms acquisition time was chosen slightly less than T_2^* to have good FID SNR.

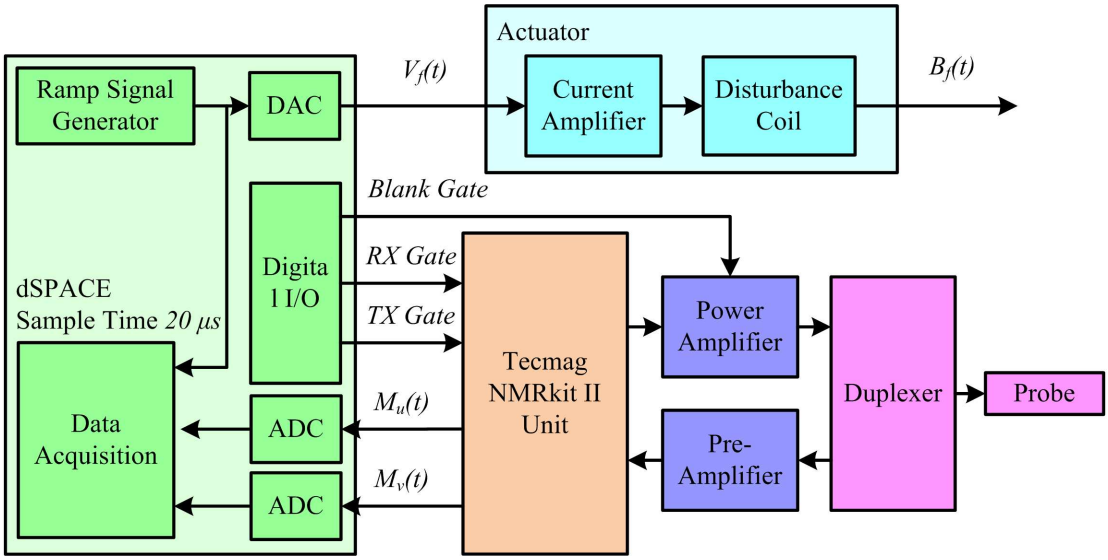

Figure 5.5. Experimental setup for generating ramp disturbance field and acquiring sampled-data measurements of $M_u(t)$ and $M_v(t)$.

Figure 5.6 shows one of the FID signals acquired from this experiment that was applied to the estimation methods. The horizontal axis indicates time in milliseconds and the three vertical axis show sampled-data measurements of $M_u(t)$ and $M_v(t)$ as well as the phase computed using them. In the upper two subplots, the circles indicate the sampled-data points of the FID signals and the dotted lines represent the threshold levels used for the level interpolation method. The bottom subplot shows the phase angle computed from sampled-data measurements of $M_u(t)$ and $M_v(t)$. This is a line for which the slope is estimated as $\omega_b + \omega_f$ using the phase LS fit method described in Section 5.1. For this experiment, 100 FID signals like this were acquired in the presence of the ramp disturbance field in Figure 5.3.

Each direct estimation method described in Section 5.1 was applied off-line to the 100 sampled-data FID signals. Just as in Figure 5.6, each FID was acquired for a time duration of 2.5 ms. The results of each estimation method is shown in Figure 5.7. The blue dashed line is the applied disturbance, which is represented as field in the left axis and frequency shift in the right axis. The red squares, green circles, and magenta triangles are the estimate of the disturbance using the FFT, level interpolation, and phase LS fit methods respectively.

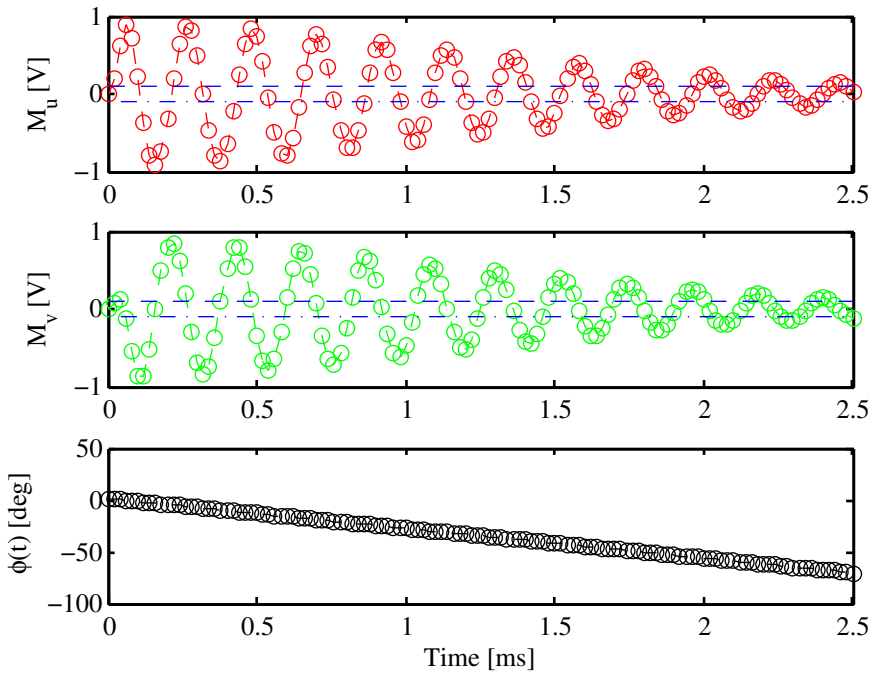

Figure 5.6. Example FID signal M_u and M_v acquired using dSPACE and corresponding phase.

This figure shows that the estimate matches the disturbance well during the ramp field change from 0 to 5 seconds and from 5 to 10 seconds. However, at the time instants 5 and 10 seconds when the disturbance changes from 47 mG to 0 mG, the estimates are somewhere in between 47 and 0 mG. This is because the assumption that B_f is constant during FID acquisition is no longer valid. Recall from the previous section that when this assumption is violated, the estimation methods find an average value of the field change. In this case the average value is computed as 17 mG at 5 and 10 seconds, which is close to half the 47 mG change at that these time instants.

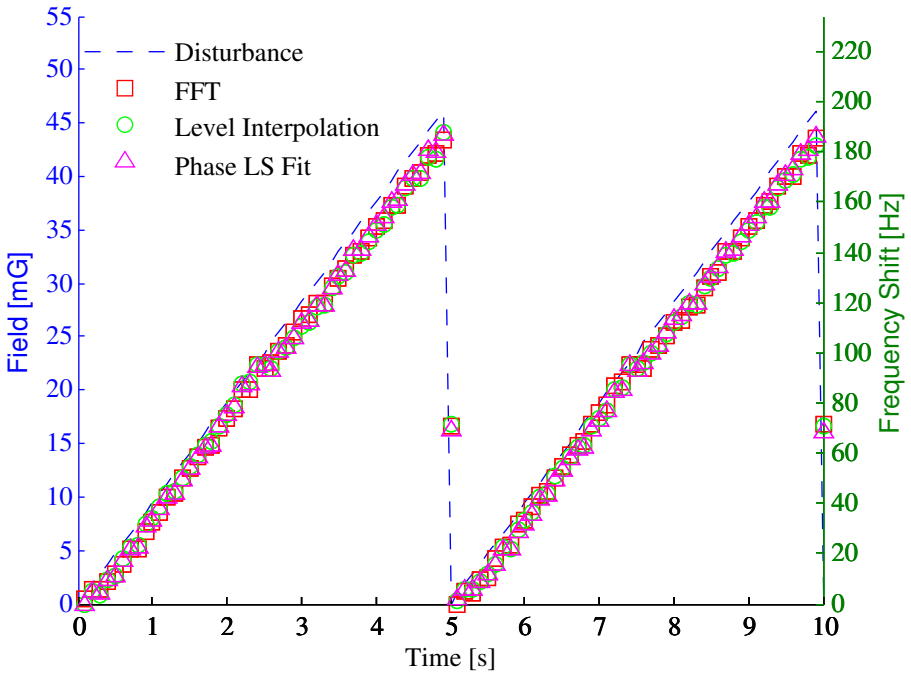

Figure 5.7. Disturbance field estimation for three direct estimation methods.

Before further analyzing these experimental results, it is important to compare the performance of the field estimate derived from NMR measurements to that derived from inductive measurements. Figure 5.8 shows the estimate of the same periodic ramp disturbance field using inductive measurements. This result, introduced in Section 1.4.2, shows the applied ramp disturbance field in the dashed line and the estimate from inductive measurements in the solid line. The inductive estimate suffers from low frequency noise and low pass filtering effects, and when comparing Figures 5.7 and 5.8 it is apparent that these limitations are no longer present when using NMR to estimate the disturbance. This demonstrates the advantage of using the NMR measurements over inductive measurements for estimating lower frequency fluctuations.

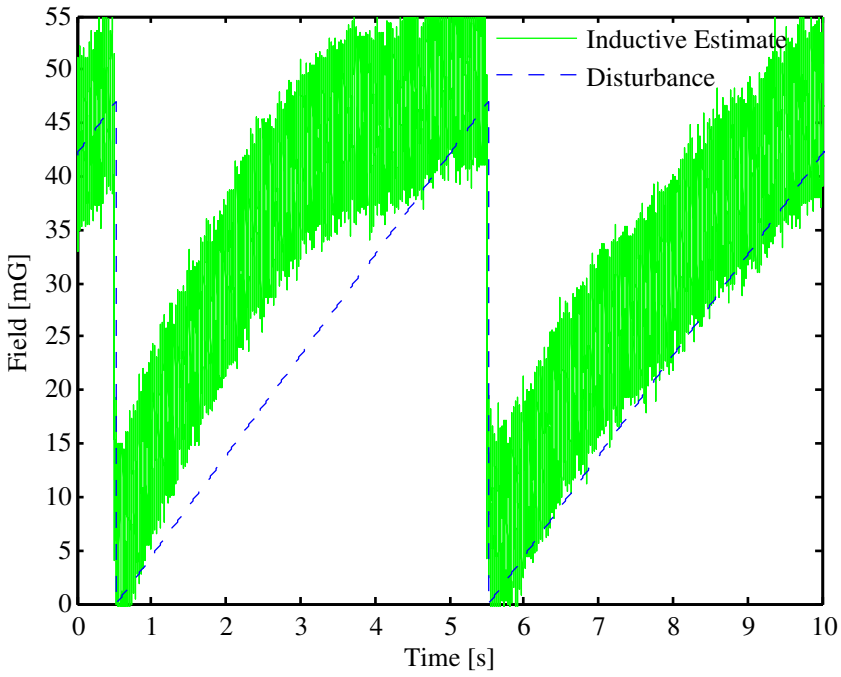

Figure 5.8. Inductive measurement for a low frequency field fluctuation superimposed on the field of a 7.1 T superconducting magnet.

While the results of Figure 5.7 indicate that each estimation method can sense the ramp disturbance field, it is difficult to use these results to determine which method is performing the best. The methods can be quantitatively compared by considering the field estimation error. This error was computed as

$$B_e(n) = B_f(n) - \hat{B}_f(n), \tag{5.14}$$

where $B_f(n)$ is the disturbance field during acquisition of the n^{th} FID and $\hat{B}_f(n)$ is the estimated disturbance field from measurement of the n^{th} FID. Figure 5.9 shows the error in the estimation methods. The leftmost vertical axis is the error in field $B_e(n)$ and the rightmost axis is the error in frequency $f_e(n)$. As expected, the error is very small during the time interval 0 to 5 seconds and 5 to 10 seconds. At the time instants 5 and 10 seconds the error is very large because the estimation methods computed the average field change.

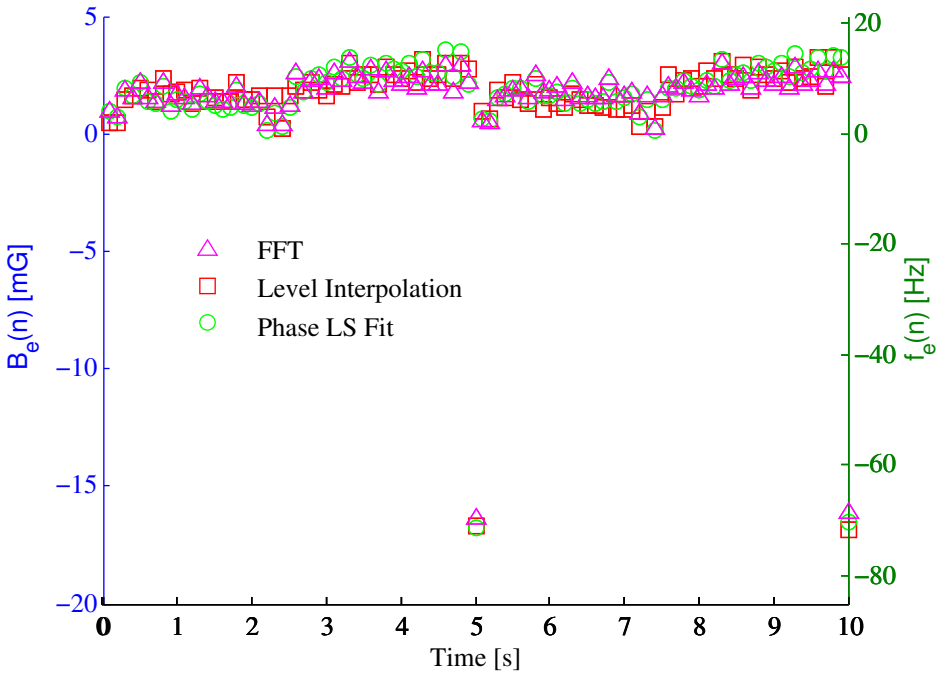

Figure 5.9. Error in disturbance field estimation for three direct estimation methods.

Even when displaying the error in the estimation methods, it is still difficult to determine which method is performing the best. The methods can be further compared by considering two error metrics derived from $B_e(n)$. The first metric is the sum of the squared error and the second is the maximum value of the error. Table 5.1 shows these error metrics for each estimation method. The second and third column show the sum of the squared error and maximum error metrics for each method. Both error metrics are computed for n from 1 to 100 because 100 FIDs where acquired, and thus 100 field estimates are obtained for each method.

Direct Estimation Method	$\sum_{n=1}^{100} B_e^2(n)$ [mG]	$\max_n B_e(n)$ [mG]
FFT	961	3.27
Level Interpolation	996	3.54
Phase LS Fit	907	3.07

Table 5.1. Error metrics for direct estimation methods using NMR measurements.

When comparing the error metrics from Table 5.1, it is evident that the phase LS fit method has the best performance when estimating this particular ramp disturbance field. The sum of the squared error and maximum error metrics are smallest when using this estimation method. The FFT method has the second smallest error metrics, and so this method performs better than level interpolation for this experiment. However, the FFT method takes the most computation time due to the necessary zero padding.

The results in Table 5.1 does not mean that the phase LS fit method is the best choice for all applications. For example, if the reference sample contains multiple Larmor frequencies that are close together, then the FFT method may be more useful. This method will choose the Larmor frequency with best SNR to use when estimating fluctuations. The level interpolation method may be more useful for FID signals with poor SNR in the acquisition window. In this case, the levels could be tuned so that estimation is performed using only the data with good SNR. The FFT method may also be more useful for applications where the field changes quickly during FID acquisition. In this case, the time varying field during FID acquisition will broaden the linewidth, but the FFT peak frequency may be approximately the same.

The phase LS fit method was chosen as the sensor for the direct FFL because it showed the smallest error metrics for the ramp disturbance field when compared to the FFT and level interpolation methods. In addition, this method requires less computation time than the FFT method, which makes it more attractive for implementation in a real–time feedback control system. The phase LS fit will now be referred to as the NMR estimator, which will be used as a sensor for the direct FFL design in Chapter 6. The following section provides an assessment of the NMR estimator, describing some of the considerations and known limitations when using the NMR estimator in real–time.

5.3 Assessment of the NMR Estimator

The previous section experimentally evaluated three different direct estimation methods. These results were used to choose phase LS fit method as a sensor for a direct FFL. Now that a phase LS fit method was chosen as the NMR estimator, it was necessary to assess this estimator for use in a real–time feedback control system. Three categories were considered in assessing the real–time implementation of the NMR estimator. These categories will be introduced here, and discussed in more detail in subsections 5.3.1 through 5.3.3.

The first category considered is the pulse sequence for real–time estimation. For the experiment shown in Section 5.2, the disturbance voltage, pulse sequence, and FID data collection were implemented in real–time using the dSPACE controller board. The NMR estimator, however, was not implemented in real–time, rather it was applied to the data off-line.

When considering real–time feedback control, it is desirable to implement the pulse sequence, NMR estimation, and feedback compensation all on the same dSPACE controller board. This is so the timing of all these operations will be synchronized. Performing all these operations on a single dSPACE controller board limits available computation time for pulse sequence. Therefore it is necessary to develop a pulse sequence that can be implemented using dSPACE while leaving enough computation time for NMR estimation and control. This pulse sequence design and considerations for the transmit signal pulse width, FID acquisition, and pulse period will be described in subsection 5.3.1.

The second category considered is FID signal measurement using the dSPACE and NMRkitII. The NMRkitII was discussed in detail in subsection 3.4.2, and must be calibrated to give quality analog FID signals for measurement by the dSPACE. The dSPACE samples the analog FID signals and performs NMR estimation using these sampled-data FIDs. The NMRkitII calibration and effects of using sampled-data FID signals to estimate field fluctuations are discussed in subsection 5.3.2. Additionally, this discussion will be used to predict the smallest field fluctuation

the NMR estimator can sense when measuring the FID signal with the NMRkitII and dSPACE.

The third category considered is aliasing of field fluctuation estimates when using the NMR estimator. The NMR estimator provides one estimate of the field fluctuations for every FID acquired, which occurs once per pulse period. This implies that the effective sampling period of the NMR estimator is equivalent to the pulse period. In other words, the NMR estimator can be viewed as sampling the field fluctuations once per pulse period. Therefore field fluctuations with frequencies above the Nyquist frequency will alias, causing the NMR estimator to predict field fluctuations that are not actually present. The effects of aliasing on the NMR estimator and how it can be removed will be discussed in subsection 5.3.3.

5.3.1 Pulse Sequence for Real–Time Estimation

The purpose of this subsection is to illustrate the challenges when implementing a pulse sequence for real–time NMR estimation using the available instrumentation, and provide information necessary for duplicating this pulse sequence. Many of the limiting factors in this pulse sequence are imposed by antiquated instrumentation and are not of theoretic interest. These limiting factors will be removed when the instrumentation is upgraded.

The NMRkitII in conjunction with the dSPACE was the instrumentation used for providing real–time estimates of B_f from analog measurements of $M_u(t)$ and $M_v(t)$. The NMRkitII console provides real–time analog $M_u(t)$ and $M_v(t)$ required by the NMR estimator. Recall from subsection 3.4.2 that the gate signals *TX Gate* , *RX Gate* , and *Blank Gate* control the pulse sequence timing for the NMRkitII. As in the experiment from Section 5.2, the dSPACE digital input/output lines will be used to generate these gate signals.

The real–time pulse sequence used to acquire FID signals for the NMR estimator is shown in Figure 5.10. The vertical axis shows the digital gate signals *TX Gate* , *RX Gate* , and *Blank Gate* generated by dSPACE, and the horizontal axis shows time. This figure shows the timing between the gate signals that are provided to NMRkitII, which is used in conjunction with the

power amplifier, duplexer, and NMR probe to generate FID signals. The details of the NMRkitII and its interface with these devices was discussed in Section 3.4.

After T_{ps_dly} seconds, the *Blank Gate* goes high, enabling the RF power amplifier from subsection 3.4.2. While *Blank Gate* is high, the *TX Gate* signal goes high for T_{pw} seconds, and the NMRkitII transmits an RF signal to power amplifier. Because *Blank Gate* is high at the same time as *TX Gate* , an RF signal is delivered to the NMR probe.

If the RF transmit signal frequency is close to the Larmor frequency, then the it will invoke the NMR response, and a signal representing M_{uv} can be measured with the RF coil in the NMR probe. The *RX Gate* signal enables the NMRkitII to receive the NMR signal when it is set to a high state. The NMRkitII then resolves the NMR signal into the signals $S_u(t)$ and $S_v(t)$ using quadrature phase detection as discussed in subsection 3.4.2. These signals are sampled during the acquisition time duration T_{acq} using the ADCs of the dSPACE. The ring down time delay T_{rd} and acquisition delay T_{acq_dly} are used to ignore transients induced in the RF coil from gates switching on or off. The pulse sequence shown in Figure 5.10 is repeated every T_S seconds, and so the pulse period is T_S. Note that the pulse period was denoted as T in the previous section. For reasons to be discussed in Chapter 6, the notation T_S is used for this pulse sequence.

The time T_{ps_dly} is a pulse sequence time delay which ensures the pulse sequence occurs periodically. Ideally, the time intervals T_{blank}, T_{rd}, T_{acq_dly}, and T_{acq} would be chosen so that their sum is an integer multiple of T_S. This ensures that the pulses occur at the same time from the start of each pulse sequence. However, using the dSPACE to generate these pulses, each pulse time interval must be an integer multiple the base sample period T_b, which is determined by the sample period of the dSPACE. This restriction means that it may not be possible to choose these time intervals such that they are an integer multiple of T_b and their sum is an integer multiple of T_S. Therefore, it is necessary to introduce the pulse sequence delay time T_{ps_dly}.

The base sample period T_b and acquisition time T_{acq} were chosen first. The NMR estimator is most effective when field fluctuations B_f are approximately constant during acquisition of the

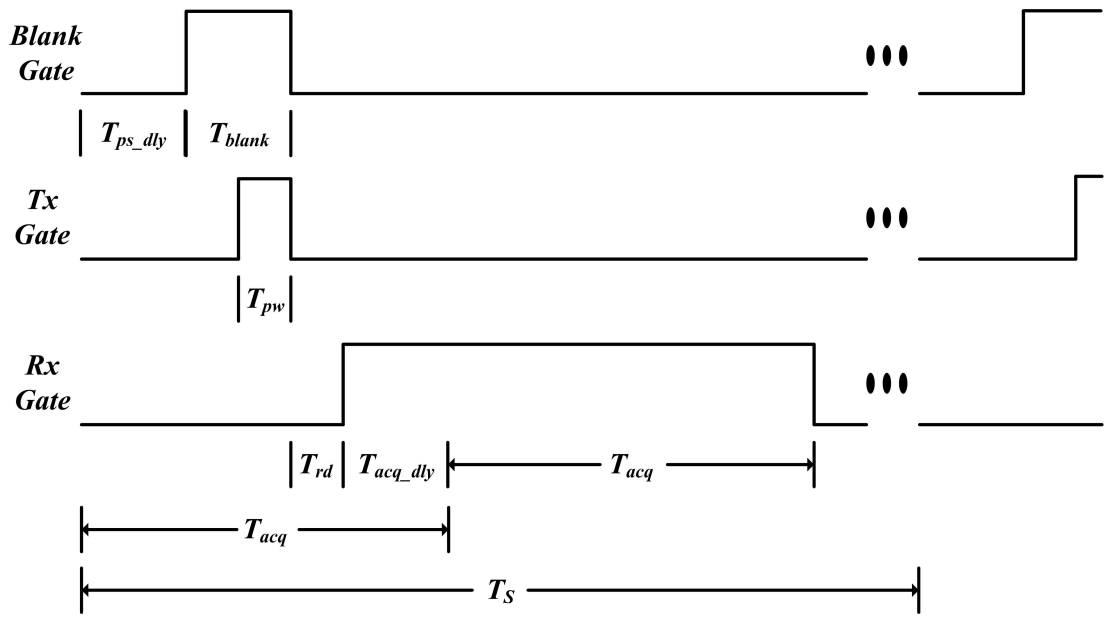

Figure 5.10. Pulse sequence used for real–time estimation of field fluctuations using NMR estimator.

FID. Recall from Section 5.2 that the variance of the phase LS fit method estimate is reduced as the number of FID points acquired, N, gets large. Thus the choice of the time intervals T_{acq} and T_b must be chosen so that the constant B_f assumption is valid and N is large enough for accurate estimation. Additionally, the dSPACE must have enough computation time available to implement the NMR estimator. The numerical values chosen for T_{acq} and T_b were 1 ms and 40 μs respectively, which provide good compromise between these tradeoffs.

The transmit pulse time interval, T_{pw} must be chosen as an integer multiple of T_b. Given that the sample time of the dSPACE was fixed at T_b, or 40 μs, the time interval T_{pw} was chosen as the minimum possible value of 40 μs. With the time interval T_{pw} fixed at 40 μs, the tip angle can only be adjusted by changing the RF transmit pulse amplitude which is controlled by an external frequency synthesizer connected to the NMRkitII. Considerations for the RF pulse amplitude adjustment will be discussed in Section 5.3.2.

The choice of the pulse period T_S presents a tradeoff between the FID SNR and NMR estimator sampling time. Recall from Section 3.1 that the NMR time constant T_1 governs how quickly the magnetization vector relaxes to thermal equilibrium. If T_S is chosen large with respect to T_1,

then the magnetization relaxes to thermal equilibrium in between pulses and the SNR of the FID is maximized. However, because the NMR estimator can be viewed as effectively sampling the fluctuations every T_S seconds, a larger T_S will increase the sampling time of the NMR estimator. This will reduce the Nyquist bandwidth of the NMR estimator. Increasing T_S improves FID signal SNR but limits the NMR estimator sampling time of the fluctuations. The pulse period T_S was chosen as 25 ms to give good compromise between FID SNR and NMR estimator sampling time.

The time interval T_{blank} was chosen as twice T_b, which is 80 μs, so that it is one pulse period longer than T_{pw}. The ring down time T_{rd} was chosen as the minimum possible time of T_b, or 40 μs. Using these values, T_{ps_dly} must be chosen as 760 μs so that the sum of T_{ps_dly}, T_{blank}, T_{rd}, and T_{acq_dly} is equivalent to T_{acq}. The numerical values of time intervals for this pulse sequence are summarized in Table 5.2.

Parameter	**Value**
T_{ps_dly}	760 [μs]
T_{blank}	80 [μs]
T_{pw}	40 [μs]
T_{rd}	40 [μs]
T_{acq_dly}	120 [μs]
T_{acq}	1 [ms]
T_S	25 [ms]

Table 5.2. Numerical values of time intervals for pulse sequence used real–time estimation.

Now that the pulse sequence for real–time estimation has been discussed, it is necessary to discuss the considerations when measuring the FID signals with the NMRkitII and dSPACE. The following subsection discusses experimental settings of these devices and the effects of using these devices to measure FID signals.

5.3.2 FID Signal Measurement

There are several factors to consider when measuring FID signals with the NMRkitII and dSPACE. The NMRkitII must be calibrated to generate quality analog FID signals, and the

dSPACE provides sampled-data FID signals to the NMR estimator. The performance of the NMR estimator is affected when using sampled-data FID signals to determine field fluctuations. For example, the amplitude of the analog FID signals must be large enough so that amplitude quantization does not limit the estimator performance. This section addresses calibration of the NMRkitII for quality analog FID signals, and the effects of using sampled-data FID signals to estimate field fluctuations. A series of simulations are executed to investigate these effects.

It was mentioned in subsection 3.4.2 that for the NMRkitII the RF signal frequency ω_r is set by an external frequency synthesizer, and difference of ω_r and the Larmor frequency ω_0 is the baseband frequency ω_b. Therefore the baseband frequency of the analog signals $M_u(t)$ and $M_v(t)$ can be tuned using the external frequency synthesizer connected to the NMRkitII. Also the pulse sequence from the previous subsection fixes the acquisition time of the FID signals at 1 ms. For this acquisition time, the baseband frequency was typically chosen between 1 and 5 kHz. This guarantees measurement of at least one cycle of the FID signal in a 1 ms time interval. For example, the results to be shown in Section 6.3 used a 2 kHz baseband frequency.

It was also mentioned in subsection 3.4.2 that the receiver of the NMRkitII has a 4 pole Butterworth low pass filter with an adjustable cutoff frequency. This cutoff frequency defines the range of frequency shifts, and hence field changes, that the NMR estimator can sense. Recall from Section 2.2 that the correction field is limited to 7 G, which is equivalent to a 4.6 kHz shift in frequency of the reference deuterium nuclei. If the baseband frequency is the maximum recommended value of 5 kHz, then a 7 G change in field can be sensed, and thus corrected as long as the cutoff frequency is greater than 9.6 kHz. In order to allow for a 1 to 5 kHz baseband frequency and the ability to correct a 7 Gauss change in field, the cutoff frequency of this filter was chosen as 10 kHz.

In addition to setting the FID baseband frequency and receiver filter cutoff frequency, the RF pulse amplitude transmitted by the NMRkitII must be adjusted to give satisfactory SNR of the analog FID signals. Recall from Section 3.2 that the tip angle θ of the magnetization vector

is proportional to the external field generated by the RF coil. If the tip angle is $\pi/2$, then the magnetization is fully tipped onto the transverse plane and the FID signals can be observed with maximum SNR. Thus by modifying the RF pulse amplitude, the tip angle can be modified, and the SNR of the analog FID signal can be improved.

The analog FID signals were tuned for maximum SNR by adjusting the RF transmit power until the largest amplitude of the FID signals were observed. The HR-MAS probe from subsection 3.4.1 installed in the Keck powered magnet was used for this measurement. The initial tip angle was observed to be greater than $\pi/2$, which implies the transmit power had to be reduced. In order to adjust the transmit power without damaging the probe RF coil, the RF transmit power was reduced by increasing the attenuation of the RF transmit signal. The attenuators were incremented until the largest amplitude of the FID signal was observed.

In addition to calibrating the NMRkitII for quality analog FID signals, there were several factors to consider when using sampled-data FID signals for NMR estimation. In the experiment from Section 5.2, the analog FID signals $M_u(t)$ and $M_v(t)$ were sampled using 12 bit ADCs of the dSPACE. These ADCs were chosen over the 16 bit ADCs because they have synchronous sampling, which is preferred when using sampled-data FID measurements for the NMR estimator. The same ADCs must be used when implementing the NMR estimator in real–time. Sampling the NMR signals implies the amplitude must be above the minimum amplitude quantization level, which is determined by the 12 bit ADCs and the 20 Volt range of the dSPACE. The minimum quantization level of these ADCs is computed as $2^{12}/20$ V which is 4.9 mV. This means if the FID signal amplitude is below 4.9 mV, then it cannot be detected using these ADCs. In practice, the NMR signal amplitude must be significantly larger than the minimum amplitude quantization level.

Because the NMR estimator is implemented with dSPACE, it uses sampled-data FIDs to estimate field fluctuations. The NMR estimator performance will be affected by changes in T_2^*, FID SNR, and DC offset. Additionally, there is a limit on the smallest field change, or

frequency shift the NMR estimator can determine using sampled-data FIDs. Simulations of the NMR estimator were used to investigate these effects. For this simulation, the complex signal representation of the FID signal in equation 5.4 was used to generate sampled-data FIDs and the NMR estimator was applied to the simulated signal.

The amplitude, A, was chosen as 1 Volt, which is a typical value measured in experiment, and the initial phase ϕ_0 was assumed to be zero for convenience. The FID signals were quantized in amplitude using a 12 bit converter. The baseband frequency $\omega_b/2\pi$ was chosen as 2 kHz because this is the value that will be used in Chapter 6. The acquisition time and sampling frequency of the FID were chosen as 1 ms and 25 kHz, which are the values that will be used for the pulse sequence for real–time estimation. The constant field fluctuation B_f was chosen as 153 mG. This corresponds to a 100 Hz shift in FID frequency of deuterium nuclei, which is a fraction of the baseband frequency. The FID frequency shift is denoted as $\omega_f/2\pi$ or Δf. The goal of these simulations is to observe how well the NMR estimator determines B_f or Δf from sampled-data FIDs. Using these fixed parameters, three simulation studies were executed to observe NMR estimator performance as function of T_2^*, SNR, and DC offset. A fourth simulation study considers the effect of changing B_f for each FID.

For the first simulation study, the NMR time constant T_2^* was varied and the NMR estimator was used to estimate the constant B_f. The sample used for this work contains 90 % deuterium and 10 % water with 50 mM copper sulfate doping, and at 7.1 T the value of T_2^* for the deuterium in this sample was measured as 22.4 ms. Given this measurement, the value of T_2^* was varied from 0.3 ms to 25 ms in this simulation to observe the effects of T_2^* that are much smaller than this. The field error B_e defined in equation 5.14 and corresponding frequency error f_e was computed for each FID.

Figure 5.11 shows the results of this simulation. The horizontal axis shows T_2^* and the vertical axes show estimation error in field (left axis) and frequency (right axis). When T_2^* is below 2.5 ms, the estimation error is slightly more than 0.77 mG or 0.5 Hz. However, as T_2^* increases

the estimation error is less than 0.77 mG or 0.5 Hz. This shows that if T_2^* is very small, the estimator performance will degrade. This is not surprising because a smaller T_2^* means the signals $M_u(t)$ and $M_v(t)$ decay faster to zero, which limits the NMR estimator performance. It is worth mentioning that as T_2^* goes below 0.3 ms, the error becomes much larger than that observed in this figure.

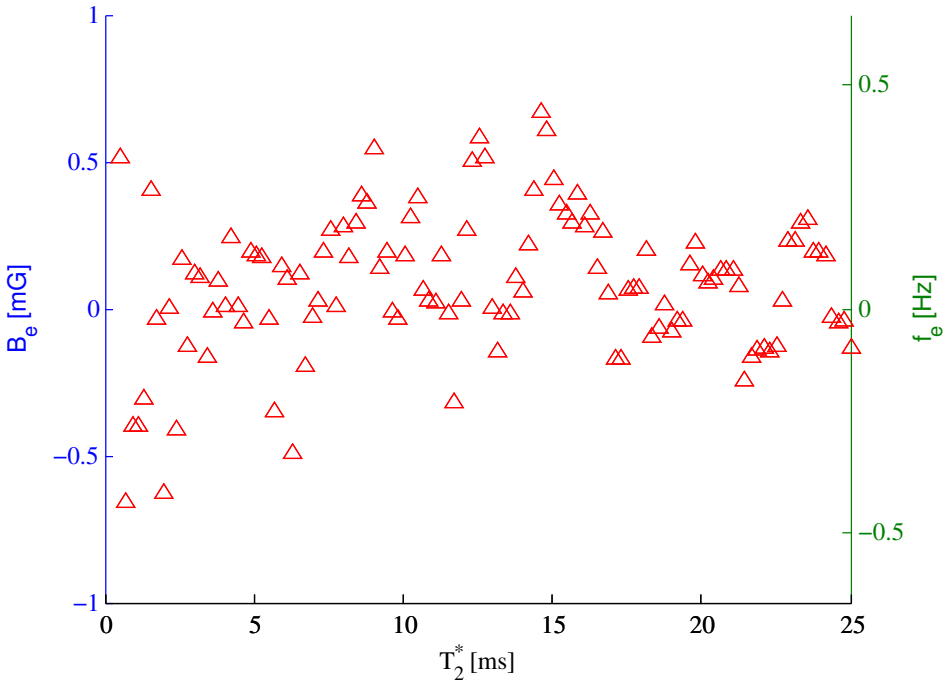

Figure 5.11. Simulated estimation error for varying T_2^*.

The second simulation study shows the effect of FID signal SNR on the NMR estimator. For this simulation, white Gaussian noise with zero mean and variance λ_0 was added to the FID signals. The noise was filtered by a 4 pole Butterworth filter with cutoff frequency 10 kHz to simulate the receiver filter in the NMRkitII. The SNR of the FID signal is defined here as the ratio of FID signal amplitude to noise variance λ_0. With an amplitude of one Volt, the FID signal SNR was varied from 3 to 100 V/V to observe the effects of FID signals with poor SNR and good SNR. These values of SNR correspond to noise variances from 0.33 to 0.01.

Figure 5.12 shows the NMR estimator error as a function of FID signal SNR. The vertical axes are again estimation error in field and frequency, and the horizontal axis is SNR in V/V. When the SNR is below 10 V/V, the error can be more than 107 mG or 70 Hz, but as the SNR increases the error decreases. When the SNR is above 70 V/V, the error remains within 31 mG or 20 Hz and increasing SNR does not improve error anymore. These results indicate that it is preferred to have an FID signal amplitude that is at least 70 times larger than the noise variance.

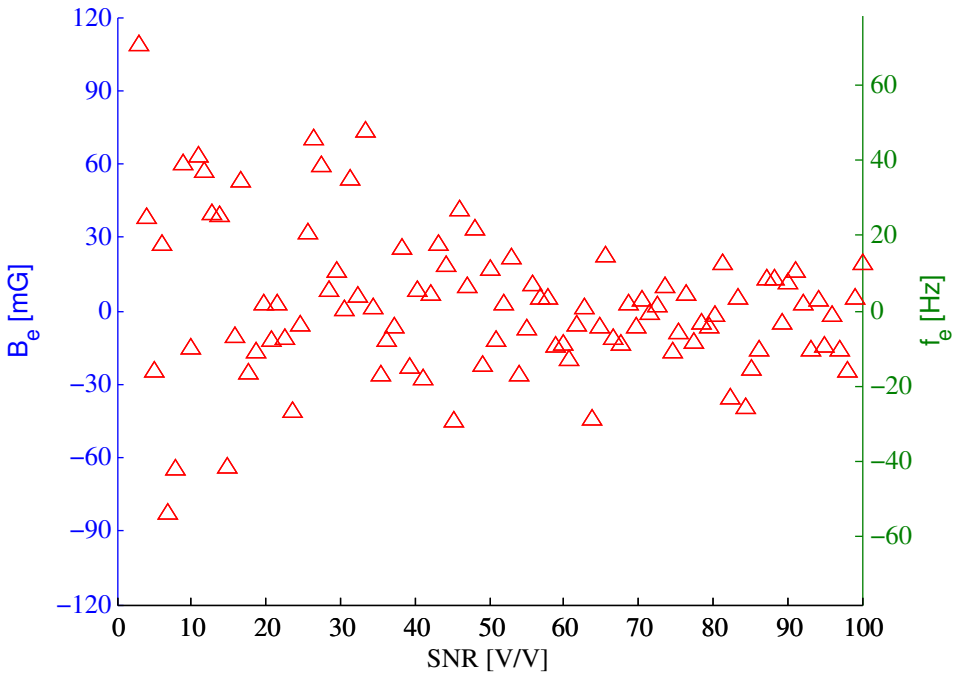

Figure 5.12. Simulated estimation error for varying FID signal SNR.

The third simulation study shows the effect of DC offset in FID signal measurements. The DC offset was added to $M_u(t)$ and $M_v(t)$ before amplitude quantization. There was no noise added to the FID signals, and the DC offset was varied between zero and half the FID amplitude, which is 0.5 Volts.

Figure 5.13 shows the results of simulated estimation error as a function of DC offset. The vertical axes show estimation error as in the previous two simulation studies. The horizontal axis is the DC offset added to both $M_u(t)$ and $M_v(t)$. These results show that the error is proportional to DC offset, and when the DC offset is 0.5 Volts the estimation error is more than 92 mG or 60 Hz. Due to this result, it was necessary to remove DC offset in the measured FID signals by subtracting the measured DC offset from $M_u(t)$ and $M_v(t)$.

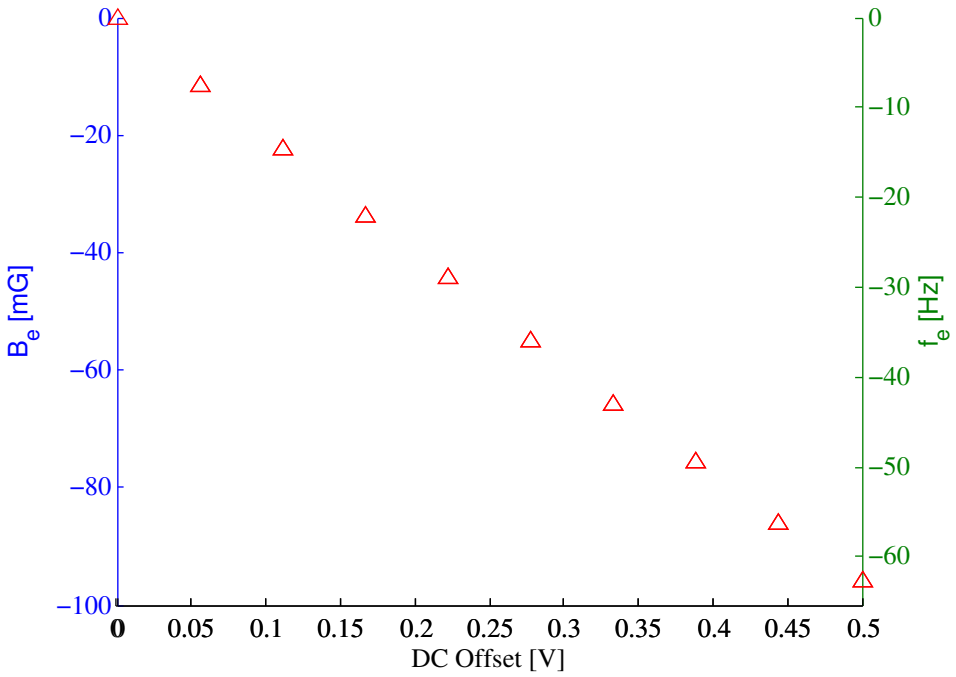

Figure 5.13. Simulated estimation error for varying DC offset of the FID signal.

The fourth and final simulation study in this subsection was meant to determine the smallest field change the NMR estimator can sense in a noiseless environment. A set of 101 FID signals where sampled and quantized, each with a different value of Δf or B_f. The values of Δf were

varied from 0 to 100 Hz in steps of 1 Hz, which corresponds to a B_f between 0 and 153 mG in steps of 1.53 mG. The first FID was applied to the NMR estimator with a 0 Hz frequency shift while the 101^{st} FID was applied to the estimator with a 100 Hz shift.

Figure 5.14 shows the results of this simulation. The vertical axis represents is the same estimation error as the previous simulation studies. The horizontal axis shows the actual, or true value of B_f applied to the FIDs. These results indicate that the error is within 0.77 mG or 0.5 Hz for all B_f. Even when there is no noise present, the quantization of the FID signals is causing error in the estimation. If the 12 bit ADCs are changed to 16 or 24 bits, then the effect of quantization is reduced and the estimation error approaches zero. This figure shows that when using the 12 bit ADCs of dSPACE, the frequency shifts that can be determined by the NMR estimator is limited to 0.77 mG or 0.5 Hz in a noiseless environment.

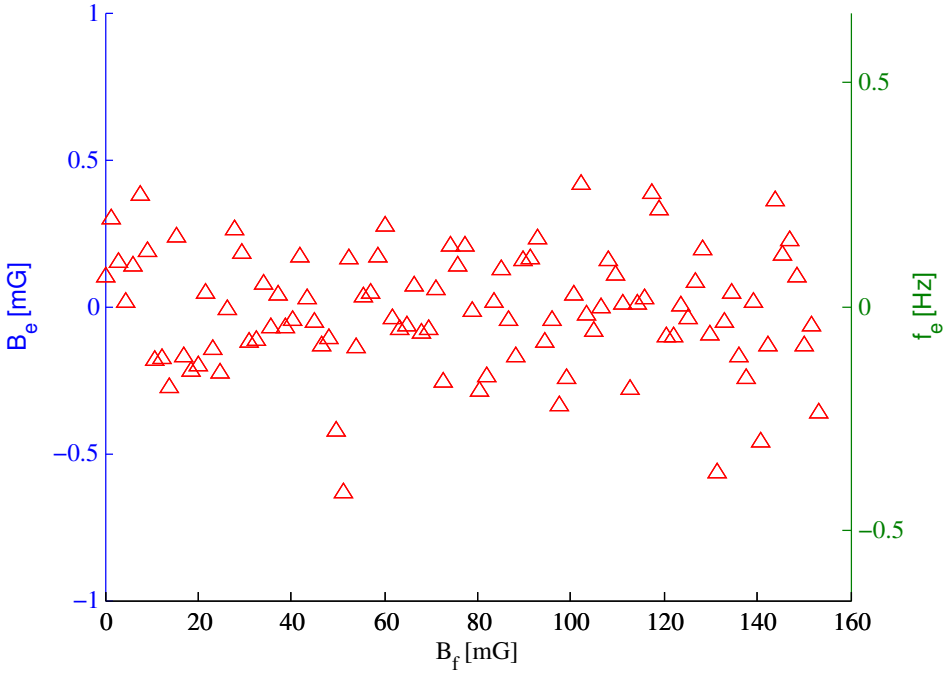

Figure 5.14. Simulated estimation error for varying frequency shift Δf of FID signal.

The results of the four simulation studies presented indicate that T_2^*, FID SNR, DC offset, and quantization all affect the performance of the NMR estimator. The most significant factor observed was the SNR of the FIDs. Even when the SNR was above 70 V/V, there was still close to a 31 mG or 20 Hz error in estimation using deuterium FIDs. When implementing the NMR estimator in a feedback control loop, the NMR estimator will be using deuterium FIDs similar to these. Thus the smallest field that the NMR estimator can sense for a direct FFL is limited to about 31 mG.

Recall from Section 5.2 that the NMR estimator was able to accurately estimate a ramp field changing slowly by 47 mG. These results may seem counter intuitive given the suggested estimation limit of 31 mG. However, the 47 mG ramp field experiment was performed for a different sample nuclei and FID sample period, both of which change the performance of the estimator. The NMR estimator limitation of 31 mG is determined using the FID sample period 40 μs and deuterium sample nuclei, both of which will be used to obtain experimental results in Chapter 6.

This subsection discussed the factors considered when measuring FID signals. The procedure for tuning the NMRkitII to achieve quality analog $M_u(t)$ and $M_v(t)$ signals was discussed first. This was followed by a study of how using dSPACE to measure, sample, and quantize the analog FID signals affects performance of the NMR estimator. Three simulation studies were presented that showed the effect of T_2^*, SNR of FID, and DC offset of the FID on the NMR estimator. An additional study showed the smallest field the NMR estimator can sense in a noiseless environment. The following subsection discusses aliasing in the NMR estimator and how it occurs.

5.3.3 Aliasing

Recall that the NMR estimator can be viewed as effectively sampling the field fluctuations once every pulse period of the pulse sequence. For the pulse sequence used for real–time estimation in subsection 5.3.1, the pulse period is denoted T_S. Therefore in this case the NMR estimator effectively samples the field fluctuations at a period T_S, or sampling frequency $1/T_S$, denoted as F_S. Any field fluctuations with frequencies above the Nyquist frequency $Fs/2$ will alias.

The following experiment was designed to demonstrate aliasing of field fluctuations with frequencies above the Nyquist frequency in the NMR estimator. A 2 Gauss, 39 Hz sinusoidal disturbance field was superimposed on the Keck powered magnet operating at 25 Tesla. The pulse sequence described in subsection 5.3.1 was used to generate FIDs from deuterium nuclei, and the NMR estimator was applied in real–time to these FIDs. The estimate of field fluctuations provided by the NMR estimator output was simultaneously observed.

Figure 5.15 shows the results of this experiment. For both subplots, the vertical axis is field change in Gauss and the horizontal axis is time in seconds. The disturbance field and NMR estimator output are shown in the upper and lower subplots respectively. The disturbance field and NMR estimator output do not match for this experiment because of aliasing. The numerical value of the NMR estimator sampling period T_S is 25 ms, or alternatively the sampling frequency F_s is 40 Hz. Any field fluctuation with a frequency greater than $F_s/2$ or 20 Hz will alias. The disturbance frequency was chosen to be 39 Hz, which will alias to a 1 Hz sinusoid when the sampling frequency is 40 Hz. This 1 Hz aliased component in the NMR estimator output is shown in the bottom subplot of Figure 5.15.

The aliasing demonstrated in Figure 5.15 is an issue when considering field fluctuations present in the Keck powered magnet. Recall from the magnitude spectra in Figure 1.5 that these fluctuations are significant at 60 Hz harmonics. When Fs is 40 Hz, the 60 Hz component aliases to 20 Hz and the 120 Hz component aliases to 0 Hz. This means the components at 60 and 120 Hz

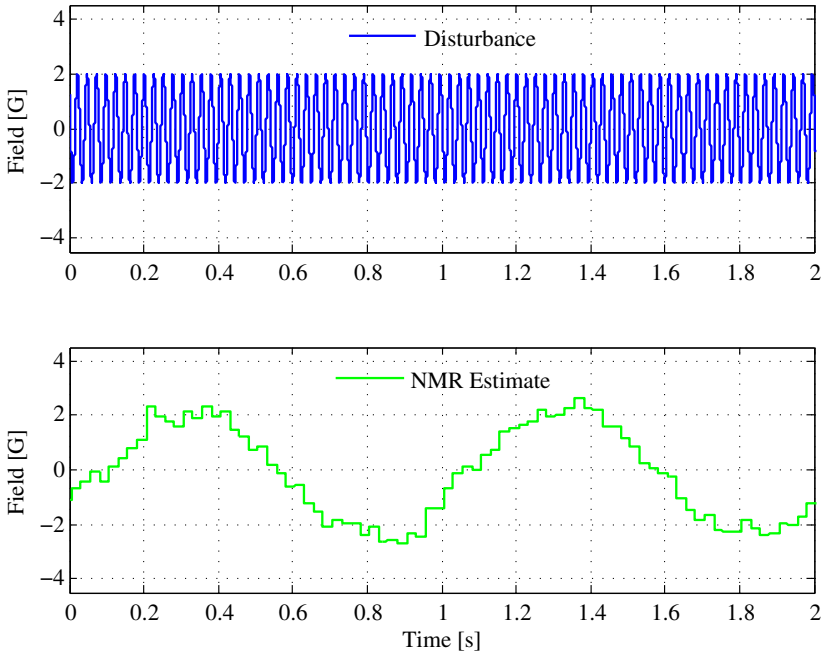

Figure 5.15. Aliasing demonstration on Keck powered magnet operating at 25 Tesla.

will appear to the NMR estimator as 20 and 0 Hz field fluctuations. Any compensator design will try to reject these frequency components, which are not a true representation of the field fluctuations at these frequencies.

The solution to aliasing in most cases is to use a low pass filter with a cutoff frequency equivalent to the Nyquist frequency, which attenuates frequency components of the analog signal above the Nyquist frequency. Then when the signal is sampled, there are no high frequency components that can alias. However, in the case of the NMR estimator, the goal is to estimate magnitude of the field fluctuations that are proportional to frequency shifts of the analog signals $M_u(t)$ and $M_v(t)$. If these signals were low pass filtered at the Nyquist frequency 20 Hz of the NMR estimator, then at most a 20 Hz shift in FID frequency can be estimated. For deuterium nuclei, 20 Hz frequency shift is equivalent to a 31 mG field change, which is very small compared to the 9 G peak to peak field changes observed experimentally.

A different approach was necessary to provide anti-aliasing for the NMR estimator. In Chapter 6, an inductive feedback control design will be shown which significantly reduces higher frequency field fluctuations. Thus the inductive feedback control loop provides anti-aliasing for the NMR estimator. To demonstrate this, Figure 5.16 compares the NMR estimator output with and without inductive feedback control for the same 2 Gauss, 39 Hz disturbance field in the upper subplot of Figure 5.15. The solid line is the same 1 Hz aliased component shown in the bottom subplot of Figure 5.15. The dashed line shows the NMR estimator output when inductive feedback control is engaged. In this case, inductive feedback control provides anti-aliasing as the aliased component is removed.

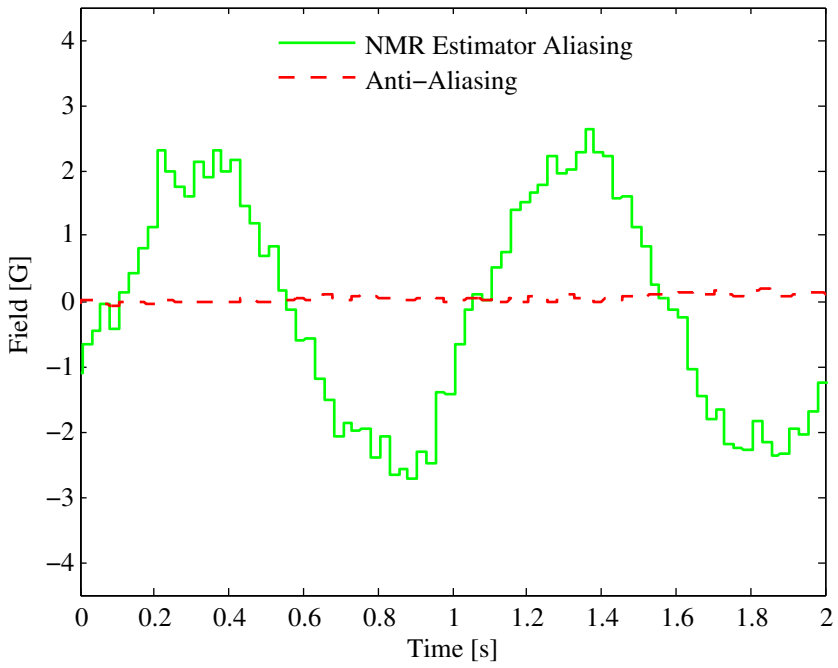

Figure 5.16. Anti-aliasing using inductive feedback control, Keck powered magnet operating at 25 Tesla.

In the following Chapter, the cascade feedback control design is presented which implements the pulse sequence and NMR estimator discussed in this Chapter. A feedback control design using inductive measurements to estimate higher frequency fluctuations is presented first. The inductive feedback control design is then combined with a direct FFL using NMR measurements to estimate lower frequency fluctuations. The pulse sequence and NMR estimator are used to estimate the lower frequency fluctuations for this direct FFL design. The feedback control design will be verified experimentally using the Keck powered magnet operating at 25 T.

Chapter 6

Feedback Control Design and Results

In Chapter 5, a NMR estimator was developed to provide direct estimates of lower frequency fluctuations from measurements representing the FID signals $M_u(t)$ and $M_v(t)$. When the SNR of these FID signals is above 70 V/V, and the field fluctuations have frequency components below 20 Hz, then the NMR estimator can determine field fluctuations as small as 31 mG without aliasing. This NMR estimator is explicitly independent of NMR time constants, and was developed because dispersion lock systems, which are widely used in superconducting magnets and discussed in Chapter 4, have limited fluctuation suppression capability in powered magnets where $B_f(t)$ changes quickly with respect to T_1.

In addition to lower frequency estimates provided by the NMR estimator, higher frequency field fluctuations can be estimated from inductive measurements as discussed in Chapter 1. This Chapter presents the design, synthesis, and verification of a sampled-data feedback control system using lower frequency fluctuation estimates from the NMR estimator and higher frequency fluctuation estimates from inductive measurements. The design presented herein is the cascade

feedback control system introduced in Chapter 1, which is a multi-loop multi-rate feedback control system whose objective is to reduce both lower and higher frequency field fluctuations. This approach is experimentally verified using a 7.1 T superconducting magnet and the Keck powered magnet operating at 25 Tesla.

Section 6.1 describes the control strategy for reducing lower and higher frequency fluctuations in powered magnets. The objectives of the control design using the performance metrics introduced in Section 1.6 are presented. The cascade control strategy, which is the cascade combination of an inductive feedback control loop and a direct FFL control loop, is proposed as a method for achieving the desired control objectives. Section 6.2 describes the design procedure for the cascade feedback control system. Using mathematical models identified in Section 2.3, sampled-data feedback compensators are designed for the inductive and direct FFL control loops. Section 6.3 provides experimental results and compares them to the desired control objectives of the cascade control design. Experimental results using a 7.1 T superconducting magnet and the Keck powered magnet are presented separately. Although some results are presented for a 7.1 T superconducting magnet, the design and experimental results in this chapter focus on the Keck powered magnet operating at 25 T because the objective of this project was to reduce field fluctuations in a powered magnet.

6.1 Control Strategy

6.1.1 Control Objectives

The overall objective of this project was to design a feedback control system which reduces lower and higher frequency field fluctuations to facilitate NMR spectroscopy in powered magnets. This subsection specifies the control objectives for the feedback control design using the three performance metrics introduced in Chapter 1. The proposed cascade feedback control system for achieving these objectives will be discussed in the following subsection.

The first performance metric was the frequency response of the transfer function B/B_f, which is the transfer function from field fluctuations $B_f(t)$ to field output $B(t)$. Recall that the magnitude of the transfer function B/B_f gets small when field fluctuations are reduced. By comparing the open and closed-loop frequency response of B/B_f, the control designer can quantify the field fluctuation suppression provided by the compensators for the frequencies of interest.

The second and third performance metrics are the linewidth and peak frequency derived from the magnitude spectra of consecutive FID signals. Recall from the simulation in Section 3.3 that a 60 Hz sinusoidal field fluctuation is predicted to broaden the linewidth. When higher frequency fluctuations like this 60 Hz component are reduced, the linewidth of the FID spectra will be reduced. Also recall from Section 5.1 that the peak frequency of the FID magnitude spectra shifts in the presence of field fluctuation that changes slowly over a long period of time. Thus lower frequency fluctuations shift the peak frequency of the FID magnitude spectra, and when these fluctuations are reduced, the standard deviation of the peak frequencies will be reduced. The feedback control system's ability to reduce lower and higher frequency fluctuations can be evaluated by comparing open and closed-loop linewidth and peak frequencies of the FID magnitude spectra.

The control objectives for the feedback control system are specified using this these known effects of field fluctuations on the performance metrics. It has been mentioned throughout this dissertation that inductive feedback control is suitable for reducing higher frequency fluctuations while a direct FFL is suitable for reducing lower frequency fluctuations. As such, the control objectives for the inductive feedback control system are specified first for higher frequency fluctuations. This will be followed by control objectives for the direct FFL, which are specified for lower frequency fluctuations.

In order to specify the desired magnitude of B/B_f using inductive feedback control, it is necessary to quantify the frequencies at which this feedback control system will reduce fluctuations.

In Section 2.3, the bandwidth of the uncompensated loop transfer function for this feedback control system was identified as 3204 Hz with a lower cutoff frequency of 0.008 Hz. Ideally, the inductive feedback control system could reduce field fluctuations as low as 0.008 Hz and as high as 3204 Hz. However, as discussed in subsection 1.4.2 inductive measurements suffer from 1/f noise at lower frequencies. Additionally, recall from Section 3.3 that the effect of higher frequency field fluctuations above several kHz do not affect NMR spectroscopy. Therefore the frequencies at which inductive feedback control system reduces field fluctuations was defined between 1 Hz and 2500 Hz.

The magnitude spectra of field fluctuations in subsection 1.4.1 showed that the largest field fluctuation amplitude observed with inductive measurements was 0.16 Gauss rms at 60 Hz. Recall from Section 3.3 that this field fluctuation corresponds to a Bessel function argument $\gamma B_{fo}/\omega_f$ of 1.81, and broadens the linewidth from 100 Hz to 190 Hz. If this field fluctuation is reduced by a factor of 100, or 40 dB, then $\gamma B_{fo}/\omega_f$ is approximately 0.02 and the linewidth will return to 100 Hz, which is desired for NMR. Ideally, a 40 dB reduction in field fluctuation over for the 1 Hz to 2500 Hz frequency range could be maintained to give a 100 Hz linewidth. However, this may not be possible when considering that the system must remain stable. Thus it was desirable for inductive feedback control to have as much as a 40 dB reduction in field fluctuation over for 1 Hz to 2500 Hz frequency range while maintaining stability. Additionally, it was desirable to have more reduction in B_f at the 60 Hz, 120 Hz, 180 Hz, and 720 Hz because these were the 60 Hz harmonics with the largest amplitude measurements. The reduction in B_f at these frequencies was specified to be as much as 60 dB while maintaining stability.

The frequencies at which the direct FFL can reduce field fluctuations is defined by the NMR estimator discussed in Section 5.3. The effective sampling rate of the NMR estimator was defined as 40 Hz, which gives a Nyquist frequency of 20 Hz. Additionally, the NMR estimator can sense fluctuations down to DC as it determines fluctuations from NMR measurements and not inductive measurements. Therefore the direct FFL can reduce fluctuations from 0 Hz to 20 Hz.

Field fluctuations between 0 and 20 Hz are considered lower frequency fluctuations, and thus shift the peak frequency of the FID magnitude spectra. It will be shown that with inductive feedback control, where lower frequency fluctuations are still present, the standard deviation of these frequency shifts is 6969 Hz. If lower frequency fluctuations are reduced by a factor of 100, or 40 dB then this standard deviation is expected to be reduced by the same amount. This 40 dB reduction would result in a standard deviation near 70 Hz, which is less than 100 Hz desired for NMR. Thus it was desirable to have the direct FFL reduce lower frequency fluctuations by 40 dB.

The inductive feedback control system is not specified to reduce fluctuations below 1 Hz. Therefore the direct FFL alone should maintain this 40 dB reduction until 1 Hz. Between the frequencies 1 Hz and 20 Hz, the direct FFL and inductive feedback control system will both have the ability to reduce field fluctuations. Over this frequency range, the direct FFL compensator must be merged with the inductive feedback control system to maintain 40 dB reduction of B_f. As in the inductive feedback control system, the NMR feedback control system must also maintain closed loop stability.

The control objectives of this feedback control system design are summarized in the following list.

1. Reduce field fluctuations between 1 Hz and 2500 Hz by as much as 40 dB using inductive feedback control.

2. Reduce field fluctuations at 60 Hz, 120 Hz, 180 Hz, and 720 Hz by as much as 60 dB using inductive feedback control.

3. Reduce field fluctuations between 0 Hz and 1 Hz by as much as 40 dB using a direct FFL.

4. Show reduction of lower and higher frequency fluctuations by simultaneously achieving the first three control objectives.

5. Show reduction of higher frequency fluctuations by comparing open and closed-loop linewidth of FID magnitude spectra.

6. Show reduction of lower frequency fluctuations by comparing open and closed-loop peak frequency shift of FID magnitude spectra.

The following subsection discusses the proposed cascade feedback control system for achieving these control objectives in a experimental system.

6.1.2 Cascade Control

The proposed feedback control system for achieving the control objectives is the cascade feedback control system last shown in Section 2.3. The block diagram of this system is shown Figure 6.1 where the inductive and direct FFL compensators have been replaced with $G_{Ci}(z)$ and $G_{Co}(z)$ respectively. As mentioned previously, this is a multi-loop multi-rate feedback control system [71] as it is the cascade combination of two feedback control loops, each with different sampling rates. The cascade approach was chosen to merge the separate bandwidths of inductive feedback control and a direct FFL.

The inductive feedback control loop is defined as the fast, inner loop of the cascade feedback system. This loop is comprised of a the current amplifier and correction coil, pickup coil and integrating preamplifier, and a sampled-data feedback compensator $G_{Ci}(z)$. The inner loop sensor is the pickup coil and integrating preamplifier, which provides inductive measurements for estimating higher frequency fluctuations B_{High}. The analog signal at the integrating preamplifier output is sampled at a fast sampling period T_F in order to observe these fluctuations. The inner loop sampled-data compensator $G_{Ci}(z)$ is designed to reduce B_{High}. The sample period T_F was chosen as the maximum 20 μs sampling period of the dSPACE controller board used to implement $G_{Ci}(z)$.

The direct FFL control loop is defined as the slow, outer loop of the cascade feedback system.

This loop is defined as an amplifier and correction coil, NMR console and field estimator, and a sampled-data feedback compensator $G_{Co}(z)$. The outer loop sensor is the NMR console and field estimator, which estimates field fluctuations from FID signal measurements. The NMR console used is the NMRkitII describe in subsection 3.4.2 and the field estimator is the NMR estimator from Section 5.3. For this sensor, the NMR console in conjunction with dPSACE generates the pulse sequence with pulse period T_S as described in subsection 5.3.1. The resulting analog signals representing $M_u(t)$ and $M_v(t)$ are sampled at 40 μs by the dPSACE. The NMR estimator uses these sampled-data measurements to directly estimate lower frequency fluctuations B_{Low}. The estimate B_{Low} is updated every at a slow sampled period T_S, and the outer loop sampled-data compensator $G_{Co}(z)$ is designed to reduce B_{Low}. The compensator sample period is equivalent to the pulse period T_S, which was chosen in subsection 5.3.1 as 25 ms and is an integer multiple of the 20 μs chosen for T_F.

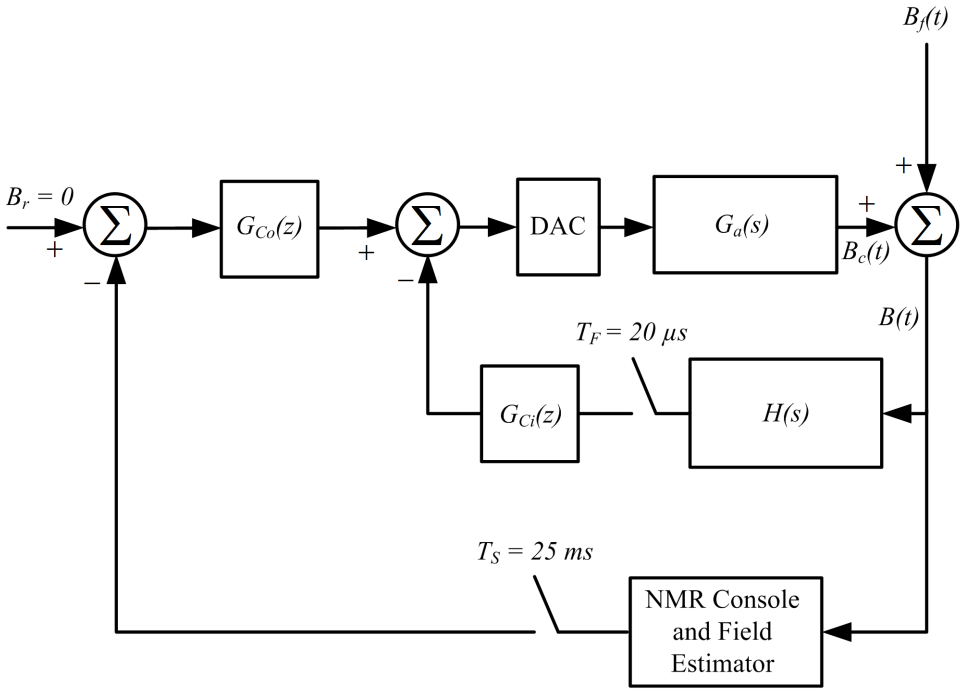

Figure 6.1. Cascade feedback control strategy for reducing lower and higher frequency field fluctuations.

For the cascade feedback control system design, given that $T_F \ll T_S$ one approach could be to model the inner loop as a static gain when designing the outer loop compensator. This approach did not work, however, because the lower cutoff frequency of the inner loop is below the higher cutoff frequency of the outer loop. The inner loop introduces dynamics to the outer loop in its bandwidth, and therefore the inner loop cannot be modeled as a static gain when designing the outer loop. Instead the cascade feedback control system was designed using computer simulations to account for the inner loop dynamics in the outer loop design.

The following section describes the modeling and design procedure for the cascade feedback control system in Figure 6.1. Mathematical models of the pickup coil and integrating preamplifier identified in Section 2.3 as well as model of the NMR console and estimator will be used to design the inner and outer loop compensators $G_{Ci}(z)$ and $G_{Co}(z)$.

6.2 Cascade Control Design

This section shows the modeling and design procedure for the cascade feedback control system. Subsection 6.2.1 shows the design of the inner loop compensator $G_{Ci}(z)$ using the identified models $H(s)$ and $G_a(s)$ from Section 2.3. The transfer function $H(s)$ models the pickup coil and integrating preamplifier and the transfer function $G_a(s)$ models the amplifier and correction coil. Subsection 6.2.2 shows the derivation of analytical model of the NMR console and estimator. The design of the outer loop compensator $G_{Co}(z)$ is shown using this model and the inner loop models determined in the previous subsection.

6.2.1 Inner Loop Design

Recall from subsection 1.4.1 that the PLL-IMP inductive compensator design showed substantial reduction of higher frequency fluctuations [27, 28]. Given these results, the inner loop compensator of the cascade feedback control system adopts the PLL-IMP design with some modifications.

The modifications to the PLL-IMP design was necessary for two reasons. First, changes in the instrumentation hardware gave a loop transfer function with a larger bandwidth than the original design. The improvement in loop transfer function bandwidth means the inner loop compensator can be modified from the original design to provide a greater reduction of higher frequency fluctuations. Second, the inner loop must be combined with the outer loop, which is designed for reducing fluctuations below 1 Hz. The original design had appreciable gain at frequencies below 1 Hz, which may cause an undesirable interaction between the inner and outer loops.

This subsection shows an inner loop compensator design which is a modification to the PLL-IMP design to meet control objectives (1) and (2). In addition to these control objectives, closed-loop stability must also be considered in the inner loop compensator design. If the system is dynamically unstable, then parasitic oscillations will add to the undesirable effects of the field fluctuations. Therefore this section also describes the degree of closed-loop stability for the inner loop compensator design.

While the compensator $G_{Ci}(z)$ will be realized as a discrete-time transfer function using the dSPACE controller board, the design procedure begins by approximating the inner loop compensator as a continuous-time transfer function $G_{Ci}(s)$. This simplifies the design of the inner loop compensator because all inner loop models will be continuous-time transfer functions. Once the compensator $G_{Ci}(s)$ is designed, the discrete-time compensator $G_{Ci}(z)$ is determined as the zero order hold equivalent of $G_{Ci}(s)$. The compensators $G_{Ci}(s)$ and $G_{Ci}(z)$ will be compared to observe how well $G_{Ci}(s)$ approximates $G_{Ci}(z)$.

Consider the continuous-time block diagram of the inner loop in Figure 6.2. This is similar to the inner loop of the cascade feedback control system in Figure 6.1 but with the compensator $G_{Ci}(z)$ replaced by the continuous-time compensator $G_{Ci}(s)$. The closed loop transfer function from field fluctuations $B_f(t)$ to $B(t)$ is

$$\frac{B(s)}{B_f(s)} = \frac{1}{1 + G_{Ci}(s)H(s)G_a(s)}, \tag{6.1}$$

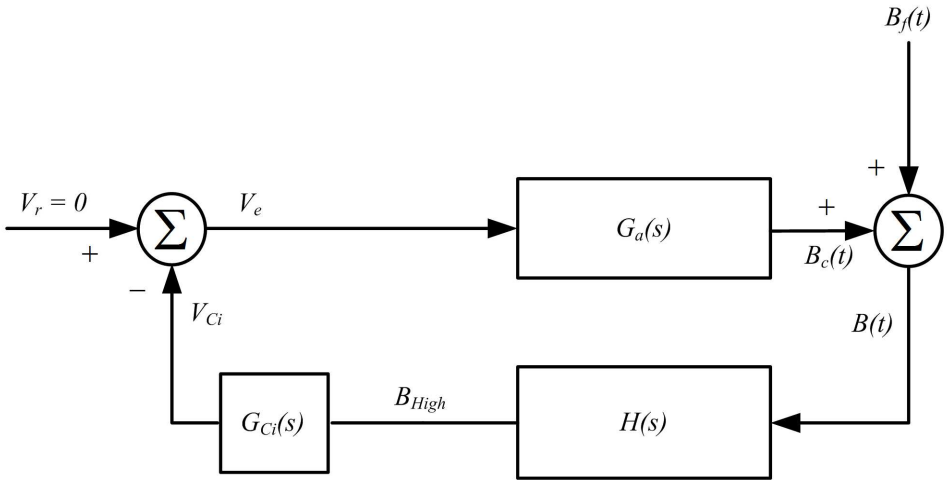

Figure 6.2. Continuous-time inner loop block diagram.

where the compensated loop transfer function is defined as

$$L_c(s) = G_{Ci}(s)H(s)G_a(s). \tag{6.2}$$

The magnitude or gain of equation 6.1 is

$$\left|\frac{B(s)}{B_f(s)}\right| = \frac{1}{|\ 1 + L_c(s)\ |}. \tag{6.3}$$

Equation 6.3 shows that $|B(s)/B_f(s)|$ is inversely related to the gain of the compensated loop transfer function. When the gain of $L_c(s)$ is much greater than one, $|B(s)/B_f(s)|$ is approximately the inverse of this gain. The compensator $G_{Ci}(s)$ can be designed to increase the gain of $L_c(s)$, thus reducing $|B(s)/B_f(s)|$.

In addition to $|B(s)/B_f(s)|$, the compensated loop transfer function $L_c(s)$ can be used to evaluate closed-loop stability of the inner loop design. The degree of stability for this design can be shown from the gain and phase margin of $L_c(s)$. The gain margin describes how much the controller gain K can be increased before the system is unstable, and the phase margin describes how much phase change the compensator can introduce to the loop before the system is unstable.

Thus the procedure for the inner loop compensator design was to propose a $G_{Ci}(s)$ to give the desired $L_c(s)$ gain over the frequency range 1 Hz to 2500 Hz, then use $L_c(s)$ to evaluate closed-loop stability. The closed-loop frequency response $|B(s)/B_f(s)|$ is then computed to verify the reduction of B_f predicted from the gain of $L_c(s)$.

The PLL-IMP design for $G_{Ci}(s)$ is the cascade combination of a phase-lead-lag (PLL) and internal-model-principle (IMP) components. The IMP components are designed to selectively suppress fluctuations from 60 Hz harmonics of the power supply ripple by applying high gain at these frequencies. The PLL component shapes the frequency response to make the closed loop system stable and has small gain at low frequencies so that a DC offset will not saturate the equipment. An explanation of the proposed phase-lead-lag (PLL) component and internal-model-principle (IMP) component, designed to meet the control objectives (1) and (2) follows.

The PLL-IMP design was determined by placing its poles and zeros at particular frequencies to shape the frequency response of the compensator. The PLL component was designed to have a 40 dB gain by 1 Hz and 0 dB gain by 2500 Hz. For the phase-lead component, if there are two poles and zeros placed at 0.1 Hz and 1 Hz respectively, then the compensator gain changes from 0 dB to 40 dB between 0.1 Hz and 1 Hz. The phase-lag component was designed to reduce the compensator gain from 40 dB to 0 dB by 2500 Hz to maintain closed-loop stability. This was achieved by placing two poles and zeros at 250 Hz and 2500 Hz respectively. This causes the compensator gain to change from 40 dB at 250 Hz to 0 dB at 2500 Hz. The resulting PLL component of this compensator is

$$G_{PLL}(s) = G_{Lead}(s)G_{Lag}(s) \tag{6.4}$$

$$= \left(\frac{\frac{s}{2\pi 0.1}+1}{\frac{s}{2\pi 1}+1}\right)^2 \left(\frac{\frac{s}{2\pi 2500}+1}{\frac{s}{2\pi 250}+1}\right)^2, \tag{6.5}$$

which is a second order phase-lead component in cascade with a second order phase-lag component.

The internal-model-principle (IMP) component for this design provides large gain at selected 60 Hz harmonics while keeping the same gain at other frequencies. As in the original design, the selected 60 Hz harmonics were the 60, 120, 180 and 720 Hz frequency components because these have the largest field fluctuation magnitudes observed in experiment. The general form of the IMP component is

$$G_{IMP}(s) = \prod_{n=1,2,3,12} \frac{\beta_n^2 + (n\omega_0)^2}{\alpha_n^2 + (n\omega_0)^2} \frac{(s+\alpha_n)^2 + (n\omega_0)^2}{(s+\beta_n)^2 + (n\omega_0)^2}, \tag{6.6}$$

where $\omega_0 = 2\pi 60$ rad/s. The IMP component has complex poles at $-\beta_n \pm jn\omega_n$ and zeroes at $-\alpha_n \pm jn\omega_n$.

The choice of the parameters α_n and β_n involves several tradeoffs. In order to provide a large gain at $n\omega_0$, it is desirable to have β_n small so that the compensator pole pairs are located near the imaginary axis. The parameter α_n is typically chosen much further from the imaginary axis than β_n. As the distance $\alpha_n - \beta_n$ increases, the gain and bandwidth of the IMP component at $n\omega_0$ increases. However, increasing this distance also reduces the gain margin, or relative stability of the IMP component, resulting in a transient response to a step field change with a large overshoot

The original choices for α_n and β_n were 100 and 0.1 respectively. While these showed significant reduction of field fluctuations at $n\omega_0$, the transient response to a step field change showed a large overshoot. This is undesirable for the cascade feedback control system as the outer loop is expected to introduce step changes in correction field to the inner loop. Therefore the parameter the distance $\alpha_n - \beta_n$ was reduced to provide an adequate transient response. The resulting choices for α_n and β_n were 10 and 0.5 respectively.

The overall inner loop compensator $G_{Ci}(s)$ is the cascade combination of the PLL and IMP components

$$G_{Ci}(s) = KG_{PLL}(s)G_{IMP}(s), \tag{6.7}$$

where K is the controller gain, which is chosen to give the desired gain of $L_c(s)$. The discrete-time inner loop compensator $G_{Ci}(z)$ is the zero-order hold equivalent of the continuous-time compensator

$$G_{Ci}(z) = \frac{z-1}{z}\mathcal{Z}\left[\frac{G_c(s)}{s}\right]_{e^{sT_S}=z}. \tag{6.8}$$

The frequency response of the continuous-time and discrete-time compensator designs are compared in Figure 6.3. The frequency response of these compensators are close to each other because the sampling frequency of $G_{Ci}(z)$ is large enough that it can be approximated as a continuous-time compensator. Because $G_{Ci}(s)$ is very close to $G_{Ci}(z)$, the compensated loop transfer function can be approximated using $G_{Ci}(s)$ to investigate stability and reduction of B_f.

Figure 6.4 shows the frequency response of the uncompensated and compensated loop transfer functions. The uncompensated loop transfer function has the same frequency response as the transfer function $L(s)$ shown in Section 2.3. For the compensated loop transfer function, the compensator gain K was chosen as 6 to achieve a gain of 40 dB at 1 Hz as specified by the control objective (1). This figure illustrates how the PLL-IMP compensator shapes the frequency response of the loop transfer function.

The PLL component of the compensator provides additional gain starting at 0.1 Hz due to the zero of the phase-lead component. By 1 Hz, the gain of the compensated loop transfer function is 40 dB which is desired. The PLL component of the compensator maintains at least a 40 dB compensated loop transfer function gain until 250 Hz, where the gain reduces due to the pole of the phase-lag component. Additionally, there are sharp peaks at the 60 Hz harmonics due to the IMP component of the compensator. The gain margin (Gm) and phase margin (Pm) were found

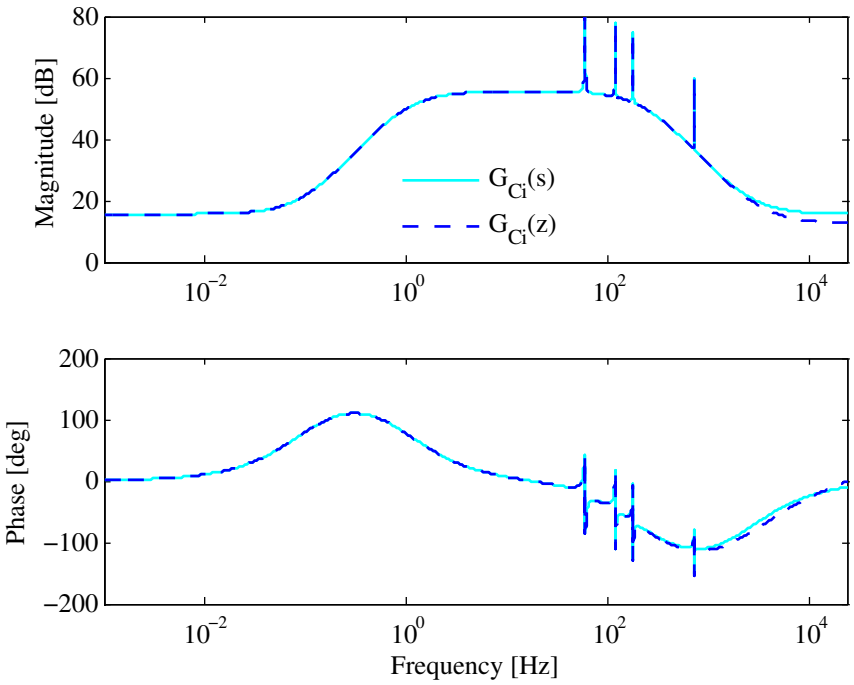

Figure 6.3. Continuous-time and discrete-time equivalent compensators for inner loop of cascade feedback system.

to be 17 dB and 36° respectively. This implies the compensator gain K could be increased by 17 dB and the phase of the loop can be increased by 36° before the system will be unstable.

As mentioned previously, when the gain of the compensated loop transfer function is much greater than one, then it provides an approximation of $|B(s)/B_f(s)|$. This assumption was used in guiding the compensator design. The true level of field fluctuation reduction can be characterized by computing $|B(s)/B_f(s)|$ using a computer simulations. Figure 6.5 shows the $|B(s)/B_f(s)|$ for the uncompensated and compensated cases. When there is no compensation, the field fluctuations pass directly to the output, and $|B(s)/B_f(s)|$ has a constant gain of 0 dB. When there is compensation, the field fluctuations are reduced implying the $|B(s)/B_f(s)|$ is between 0 and 1, which is a negative number in dB. Between 1 Hz and 250 Hz, the $|B(s)/B_f(s)|$ is less than -40 dB due to PLL component. The IMP component of the compensator yields a $|B(s)/B_f(s)|$ less than -60 dB at 60 Hz, 120 Hz, and 180 Hz, and -34 dB at 720 Hz.

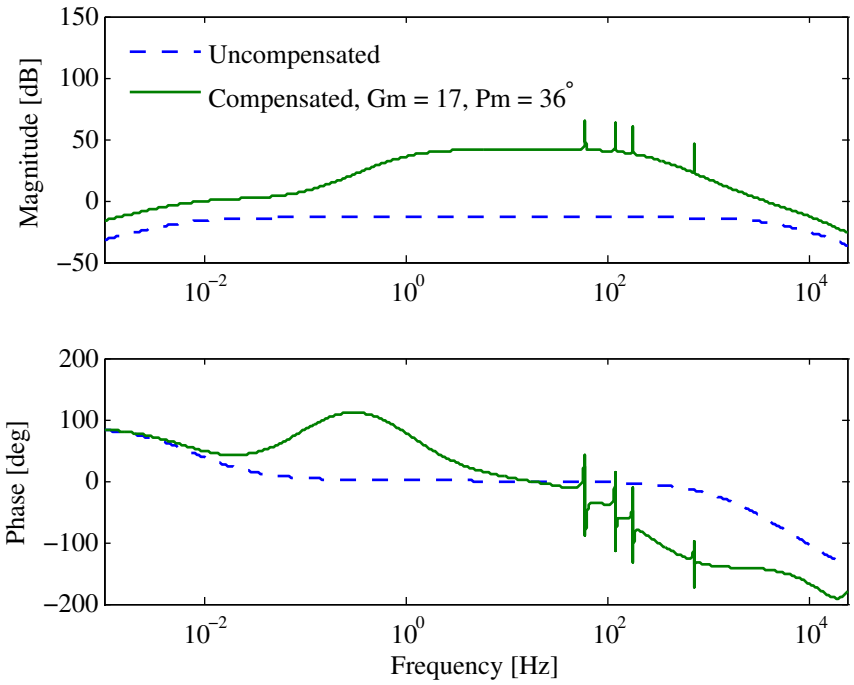

Figure 6.4. Compensated loop transfer function for inner loop of cascade feedback system.

The inner loop compensator presented in this subsection shows a reasonable degree of stability and reduction of field fluctuations that meets control objectives (1) and (2). A 40 dB reduction in fluctuations is maintained over the frequencies 1 Hz to 250 Hz, and a 60 dB reduction of fluctuations is achieved at 60 Hz, 120 Hz, and 180 Hz. Using this compensator design, the outer loop compensator $G_{Co}(z)$ will now be designed. The following subsection presents the outer loop compensator design using the inner loop compensator design from this subsection.

6.2.2 Outer Loop Design

This subsection shows the outer loop compensator designed to meet control objective (3) of reducing field fluctuations by 40 dB from 0 to 1 Hz. An analytical model of the NMR console and field estimator is determined first followed by the outer loop compensator $G_{Co}(z)$ design. The compensators $G_{Ci}(z)$ and $G_{Co}(z)$ are placed in the cascade feedback control system and its performance is evaluated using computer simulations.

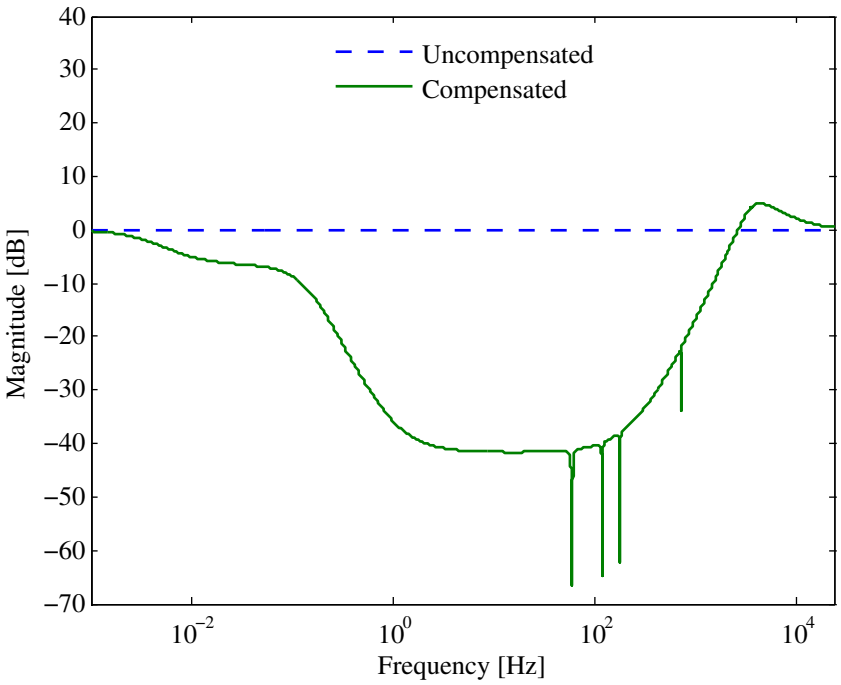

Figure 6.5. Magnitude of the transfer function B/B_f with and without inner loop compensation for Keck powered magnet.

The timing diagram in Figure 6.6 can be used to determine a model of the NMR console and field estimator. This diagram shows the operation of the NMR console and field estimator over the time duration of a single pulse period T_S. Suppose a lower frequency fluctuation, denoted as $B_{Low}(nT_S)$ in Figure 6.6, is present just before the RF pulse at time nT_S where n is an integer. The NMR estimator samples the NMR signal in response to the RF pulse and estimates field fluctuations from these sampled-data measurements. At the time instant $nT_S+\Delta t$, $B_{est}(nT_S + \Delta t)$ represents the estimate of $B_{Low}(nT_S)$ provided by the NMR estimator. The estimate $B_{est}(nT_S + \Delta t)$ is held until just before the next RF pulse, and so $B_{est}(nT_S + \Delta t)$ is equivalent to $B_{est}((n + 1)T_S)$.

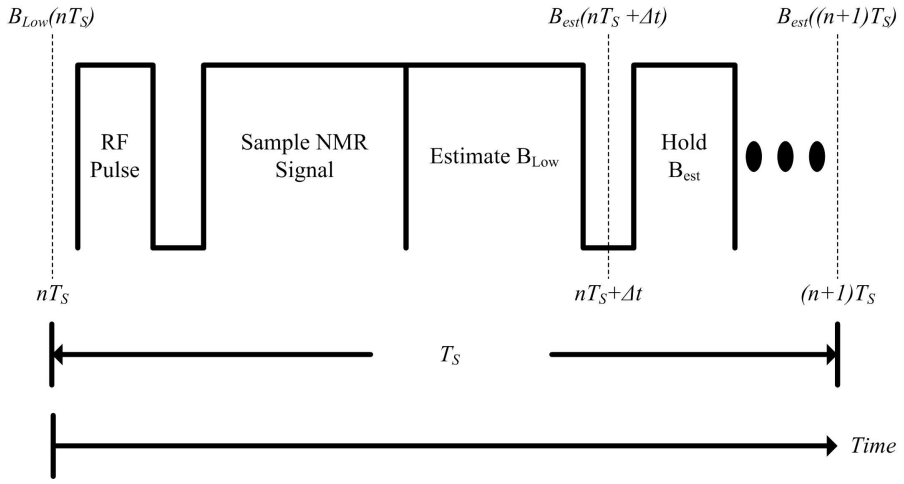

Figure 6.6. Timing diagram of the NMR estimator.

If the NMR estimator appropriately senses the lower frequency fluctuations, then the estimate $B_{est}((n+1)T_S)$ is equivalent to the fluctuation $B_{Low}(nT_S)$. Thus the NMR console and estimator can be modeled with the discrete-time expression

$$B_{est}((n+1)T_S) = B_{est}(nT_S + \Delta t) = B_{Low}(nT_S). \tag{6.9}$$

By taking the z-transform of both sides of equation 6.9, the discrete-time transfer function of the NMR estimator is

$$B_{est}(z)z = B_{Low}(z) \tag{6.10}$$

$$B_{est}(z) = B_{Low}(z)z^{-1}. \tag{6.11}$$

Equation 6.11 implies that the NMR console and field estimator can be modeled by a sampler with period T_S followed by a unit delay.

The block diagram of cascade feedback control system, revised to show this model of the NMR console and estimator, is illustrated in Figure 6.7. The NMR console and estimator has been replaced with a sampler at period T_S and a unit delay, which is modeled by the discrete-time

transfer function $1/z$. The DAC has also been replaced by a zero-order hold digital to analog converter (ZOH DAC) because the dSPACE controller boards use zero-order hold DACs.

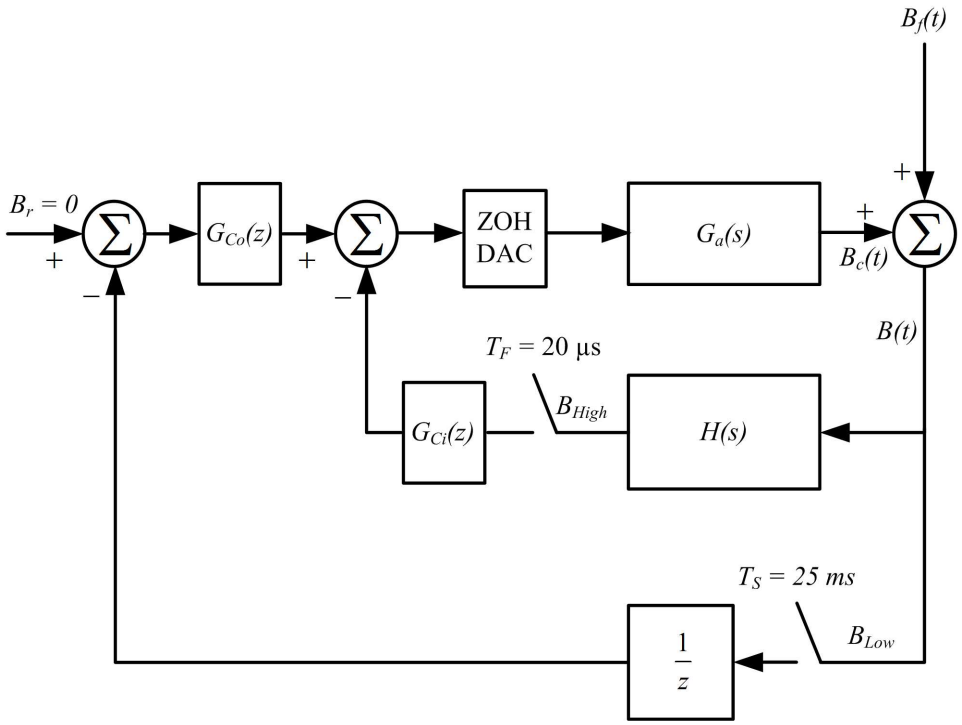

Figure 6.7. Cascade feedback control block diagram with analytical models for Keck powered magnet.

The cascade feedback control system non-trivial to analyze because it is a multi-rate multi-loop system. A review of analytical approaches for multi-rate control systems is provided by Glasson [71]. An analytical approach for this system was found to be difficult and time consuming. As an alternative, it was found that the outer loop compensator for the cascade feedback control system could be designed using a computer simulation in the Matlab Simulink environment. For the cascade feedback control system, T_F is 20 μs and T_S is 25 ms, which is an integer multiple of T_F. In this case, the discrete-time solver in Simulink can simulate the time domain response of the cascade feedback control system. Thus the procedure for the outer loop compensator design was to propose a design with gain at the desired frequency components, then use a Simulink model of the cascade feedback control system in Figure 6.7 to evaluate closed-loop stability and the magnitude response of B/B_f.

As with the inner loop compensator design, the design for the outer loop compensator began with a continuous-time approximation $G_{Co}(s)$ where it was assumed that the gain of the compensator was inversely proportional to the magnitude of B/B_f. Control objective (3) specified a 40 dB reduction in fluctuations in the frequency range 0 Hz to 1 Hz. Therefore the outer loop compensator was designed to provide 40 dB gain in the frequency range 0 Hz to 1 Hz, and reduce the gain for frequencies above 1 Hz. This can be achieved by a the following phase-lag compensator

$$G_{Co}(s) = 100\frac{\frac{s}{2\pi 10}+1}{\frac{s}{2\pi 1}+1}, \tag{6.12}$$

which has a DC gain of 40 dB, a pole at 1 Hz, and a zero at 10 Hz. A compensator with this structure will have 40 dB gain from 0 Hz until the pole at 1 Hz, then the gain will decrease by 20 dB per decade until the zero at 10 Hz. The discrete-time compensator is determined as the zero-order hold discrete-time equivalent of equation 6.12

$$G_{Co}(z) = \frac{10z + 4.536}{z - 0.8546}. \tag{6.13}$$

The gain margin of the cascade control system was determined from the time domain simulation of the Simulink model representing cascade feedback control system in Figure 6.7. A gain was appended to $G_{Co}(z)$, and the simulation generated the field output $B(t)$ in response to a unit step change in $B_f(t)$. By incrementing the appended compensator gain, the closed-loop step response becomes more under damped, and the system eventually becomes unstable when the output $B(t)$ increases without bound. The minimum appended gain at which this occurs is the gain margin. For the outer loop compensator in equation 6.13, this method was used to determine that the gain margin was 15 dB.

As a comparison, the same computation was done for a proportional outer loop compensator with P gain set to 1. The gain margin for the proportional outer loop compensator was computed as 40 dB. It may seem convenient to simply use a proportional compensator and increase the

gain as there is a 40 dB gain margin. However, if the proportional gain was increased by a large amount, then the outer loop compensator gain is also increased for frequencies above 1 Hz where there is appreciable inner loop gain. The large gain for frequencies above 1 Hz results in an under damped transient response of the inner loop to step changes from the outer loop, which is undesirable for the cascade feedback system. The phase-lag compensator does not have this issues as it reduces gain for frequencies above 1 Hz.

The magnitude response of B/B_f for the cascade control system was determined using the Simulink time domain simulation to generate the field output $B(t)$ in response to a sinusoidal $B_f(t)$ for a series of frequencies. The magnitude of B/B_f at a given frequency was determined by simulating the field output $B(t)$ in response to sinusoidal $B_f(t)$ with fixed frequency. The rms value of $B_f(t)$ and $B(t)$ was computed, and the ratio of these rms values represent an estimate of B/B_f at the sinusoidal frequency. This was repeated for multiple sinusoidal frequencies to obtain the magnitude response of B/B_f.

Figure 6.8 shows the magnitude response of B/B_f for three cases of compensation. The vertical axis shows the magnitude of B/B_f in dB and the horizontal axis shows frequency in Hz. It is desirable for the B/B_f magnitude to be as close to zero as possible, or equivalently have a more negative number in dB. The case with inner loop compensation only is indicated by the dotted line, and is identical to that shown in Figure 6.5. The case with inner and outer loop proportional compensation is indicated by the dashed line. The case inner and outer loop phase-lag compensation is indicated by the solid line.

In comparison to the inner loop only case, the proportional outer loop reduces field fluctuations by approximately 6 dB for frequencies below 0.1 Hz. For frequencies above 0.1 Hz, the proportional outer loop has no affect on the inner loop, allowing for the same field fluctuation reduction from the inner loop. The phase-lag compensator provides as much as 40 dB field fluctuation reduction for frequencies below 1 Hz. This is expected because the gain of the phase-lag compensator is large from 0 Hz to 1 Hz. This compensator achieves as much as 40 dB reduction

of fluctuations between 0 and 1 Hz, which meets control objective (3). In this case, the field fluctuation reduction below 1 Hz accomplished by the outer loop compensator does not affect the ability of the inner loop to reduce field fluctuations above 1 Hz. Therefore this design meets control objective (4) as lower and higher frequency fluctuations are simultaneously reduced per control objectives (1) thru (3). Also, the transient response of the inner loop to step changes from the outer loop was significantly better for the phase-lag compensator than the proportional compensator.

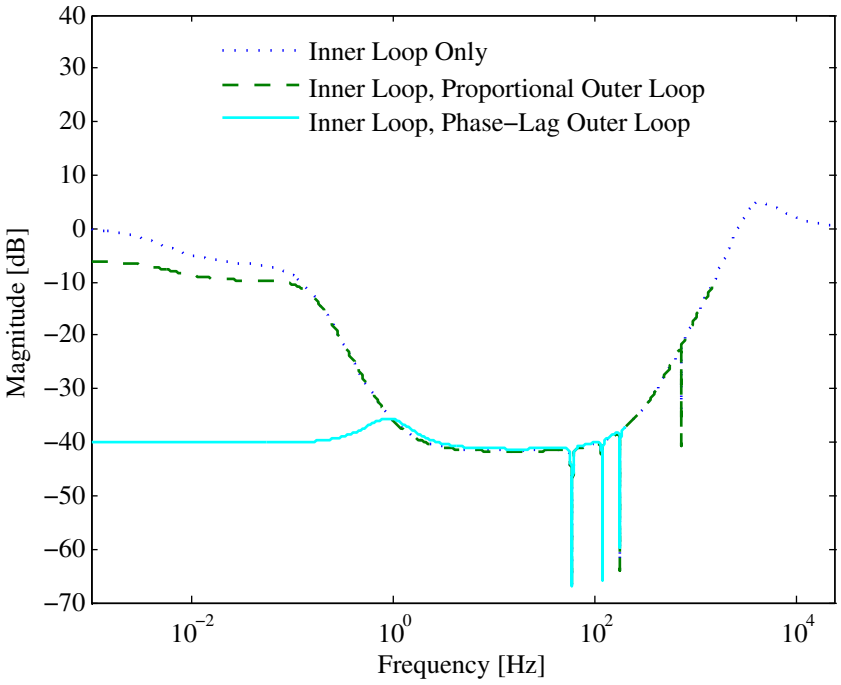

Figure 6.8. Magnitude of the transfer function B/B_f for the cases of inner loop compensation only, inner loop and proportional outer loop compensation, inner loop and phase-lag outer loop compensation for Keck powered magnet.

This subsection presented a outer loop compensator design $G_{Co}(z)$ which is inserted in the cascade feedback control system with the inner loop compensator design $G_{Co}(z)$. Simulation results of the cascade feedback control system in this subsection predict that control objectives (3) and (4) are met. The inner loop and outer loop designs predict that the first four control objectives have been met. Given these predicted results, the cascade feedback control system

was ready to be evaluated experimentally. In the following section, experimental data will be used to derive the performance metrics discussed in subsection 6.1.1. The performance metrics will be used to determine if the control objectives (5) and (6) are achieved experimentally.

6.3 Cascade Control Experimental Results

This section shows experimental results to determine if the control objectives (5) thru (6) are achieved using cascade feedback control. Experimental results are shown using the 7.1 T superconducting magnet and the Keck powered magnet operating at 25 T. Subsection 6.3.1 shows the first performance metric, frequency response of B/B_f, derived from experimental data using cascade feedback control on the 7.1 T superconducting magnet. These preliminary results indicate that the cascade feedback control system can meet control objectives (5) and (6) on the Keck powered magnet. Subsection 6.3.2 shows the two NMR performance metrics derived from experimental data using cascade feedback control on the Keck powered magnet to demonstrate control objectives (5) and (6) in a powered magnet.

The experimental realization of the cascade feedback control system requires several instrumentation devices mentioned in this dissertation. The purpose of the following discussion is to illustrate the challenges when implementing the cascade feedback control system using the available instrumentation, and provide information necessary for duplicating these experiments. Many of the limiting factors in this experimental system are imposed by this antiquated instrumentation. These limiting factors will be removed when the instrumentation is upgraded. Therefore only a brief discussion of the instrumentation is provided here.

The configuration of the devices for the cascade feedback system is different for the 7.1 T superconducting magnet and the Keck powered magnet. However, there are many common devices and parameters used for both magnets. The sample used was 90 % deuterium and 10 % water with 50 mM copper sulfate doping. The instrumentation for the inner loop, or inductive

feedback system, was described in Chapter 2. The correction and disturbance coils were mounted from the top of both magnets. The instrumentation used to acquire NMR signals was described in Section 3.4. These devices are used for the NMR estimator as well as derivation of the linewidth and peak frequency shift metrics. These configurations will be described in subsections 6.3.1 and 6.3.2. The PLL-IMP inner loop compensator $G_{Ci}(z)$ from subsection 6.2.1 was implemented using a dSPACE controller board. A second dSPACE implements the pulse sequence, NMR estimator, and phase-lag outer loop compensator $G_{Co}(z)$ from subsection 6.2.2.

6.3.1 Superconducting Magnet

This subsection shows closed-loop experimental measurements of the cascade feedback control system in the 7.1 T superconducting magnet. Experimental measurements of the magnitude of B/B_f for several frequency components are shown and compared to the predicted results from Section 6.2. If the experimental results of B/B_f match the predicted results well, then this justifies implementing the cascade feedback control system on the Keck powered magnet.

The following experiment was designed to obtain measurements of the magnitude of B/B_f for several frequency components. The Bruker probe was used in conjunction with the NMRkitII to acquire the FID signals from the reference deuterium nuclei dissolved in this liquid. The pickup coil from the HR-MAS probe was mounted from the top of the magnet for inductive measurements. The correction and disturbance coils were also mounted from the top of the magnet. Two dSPACE controller boards were used as described in the introduction to this section.

In order to evaluate the magnitude of B/B_f provided by the cascade feedback control system, sinusoidal disturbance field fluctuations were superimposed onto the magnetic field using a current amplifier and disturbance coil. The reduction in the disturbance field fluctuation at these frequency components was measured using the NMR estimator. The amplitude of the sinusoidal disturbance field was chosen as 2 Gauss meaning the peak to peak change of the disturbance was

4 Gauss. This was chosen to remain within the limit of a 7 Gauss change in field required by the current amplifier and disturbance coil. The sinusoidal disturbance field was superimposed on the magnetic field for the frequencies of 0.01, 0.1, 1, and 10 Hz. The frequencies were chosen within the 20 Hz bandwidth of the NMR estimator so reduction of fluctuations could be measured with this estimator. The resulting field fluctuation estimate from the NMR estimator was measured for open loop, inner loop compensation only, and inner and outer loop compensation. The magnitude of B/B_f at these disturbance frequencies was determined by finding the ratio of closed loop rms field to open loop rms field.

Figure 6.9 shows the results of this experiment and compares them to predicted field fluctuation reduction from Section 6.2. The predicted magnitude of B/B_f for inner loop compensation only, and inner and outer loop compensation is indicated by the dotted and solid curves respectively. The circles and x's indicate calculations of B/B_f using experimental measurements for each disturbance frequency.

The experimental NMR estimator noise floor is defined as the minimum possible magnitude of B/B_f that can be measured using the NMR estimator while implementing cascade feedback control. The NMR estimator noise floor was determined by measuring the inner and outer loop compensated field estimate with no disturbance field, and comparing this to the open loop measurements with a disturbance field. The ratio of the inner with outer loop compensated rms field estimate and the open loop rms field estimate with disturbance gives the NMR estimator noise floor. Using this computation, the NMR estimator noise floor, or minimum value the inner and outer loop compensators can reduce field fluctuations is measured as -32 dB for a 2 Gauss amplitude disturbance field. The inductive measurement noise floor was determined in the same way using inductive estimates of the field fluctuations. The NMR estimator noise floor and inductive estimate noise floor are indicated by the dashed and dash-dot lines in Figure 6.9.

There are several observations to make from the results in Figure 6.9. For the case with inner loop compensation only, the field fluctuation reduction for the disturbance frequencies 0.01 and

0.1 Hz are very close to the predicted B/B_f. At the disturbance frequencies 1 Hz and 10 Hz, the inner loop has reduced the field fluctuations to the NMR estimator noise floor. Adding the outer loop also reduces the field fluctuations at 0.1 Hz and 0.01 Hz to the NMR estimator noise floor. When using inner and outer loop compensation, the field fluctuations are reduced to the noise floor for all the disturbance frequencies. The inner and outer loop compensators reduce field fluctuations at these frequencies by as many as 32 dB.

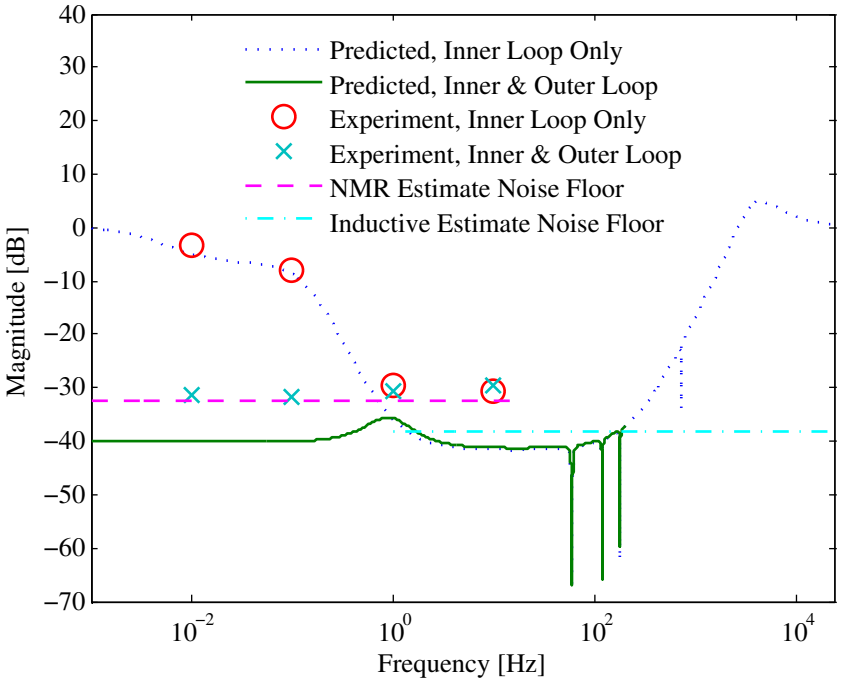

Figure 6.9. Predicted and experimental magnitude of B/B_f for inner loop compensation only, inner and phase-lag outer loop compensation on the 7.1 T superconducting magnet.

The experimental reduction of B_f provided by the cascade feedback control system on the 7.1 T superconducting magnet is promising. The disturbance field fluctuations were reduced to the NMR estimator noise floor. As operating costs of the Keck powered magnet are significant, this demonstration was necessary to justify attempting the cascade feedback control system on the Keck powered magnet. The following subsection shows experimental results of the cascade feedback control system using the Keck powered magnet operating at 25 T. The performance metrics are derived to determine if the control objectives (5) and (6) were achieved.

6.3.2 Keck Powered Magnet

The following set of experiments were designed to determine the performance metrics of the cascade feedback system on the Keck powered magnet. The HR-MAS probe in conjunction with the NMRkitII was used to acquire deuterium FID signals. The HR-MAS probe also spins the sample at a frequency greater than 1 kHz to reduce the effect of field inhomogeneities. The pickup coil from the HR-MAS probe was mounted from the bottom of the magnet for inductive measurements. As in the previous subsection, the correction and disturbance coils were mounted from the top of the magnet and two dSPACE controller boards were used as described in the introduction to this section. The Tecmag spectrometer, which was not used in the previous subsection, was used here to acquire FID signals from the main hydrogen nuclei of the sample. These FID signals are used to derive the linewidth and peak frequency shift performance metrics.

In order to assess the magnitude response of B/B_f, this performance metric was derived from experimental data measured while implementing cascade feedback control. These results where then compared to that predicted in simulations. For these experiments, a 4 Gauss peak to peak sinusoidal disturbance field fluctuation with frequencies 0.1, 1, and 10 Hz was superimposed on the field using the amplifier and disturbance coil. The NMR estimator output for each disturbance frequency was recorded using the dSPACE for the cases with inner loop compensation only and inner and outer loop compensation. The spectra of the NMR estimator output was then

determined off-line and the magnitude of B/B_f was calculated from the ratio of closed-loop and open-loop spectra magnitude at the disturbance frequencies.

Figure 6.10 shows the measured magnitude of B/B_f using the NMR estimator and compares this to that predicted. The predicted magnitude of B/B_f is shown for the cases with inner loop compensation only and inner and outer loop compensation, represented by the dashed and solid lines respectively. The open circles indicate the experimental magnitude of B/B_f when only the inner loop compensator is engaged, and the x's indicate this metric when both inner and outer loop compensators are engaged. The magnitude of B/B_f measured with the NMR estimator matches the predicted within a few dB for the disturbance frequencies 0.1, 1, and 10 Hz. The measured reduction in field fluctuation for these disturbance fields is close to 40 dB, which meets control objectives (1) and (3).

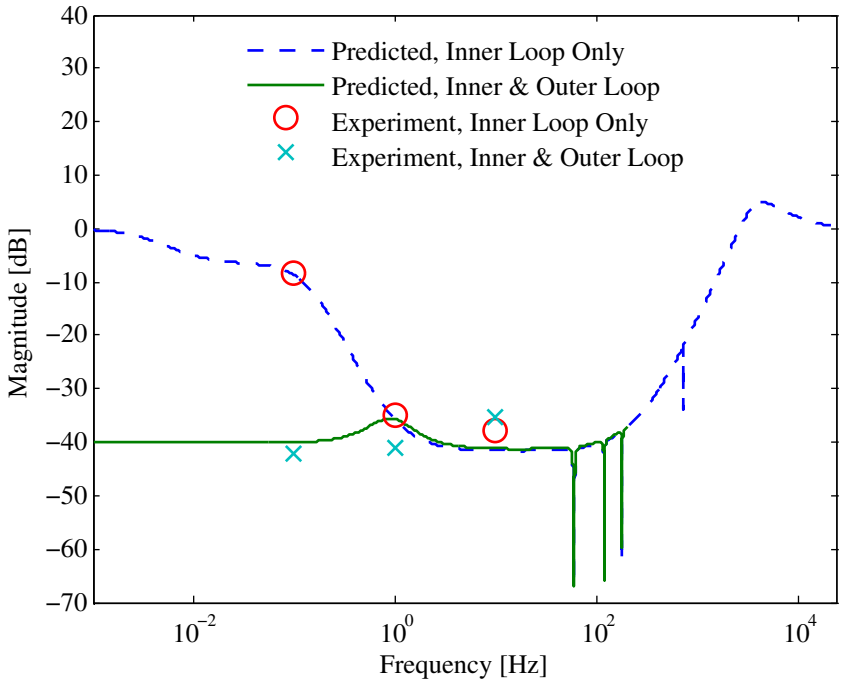

Figure 6.10. Predicted and experimental magnitude of B/B_f for inner loop compensation and inner and outer loop compensation, measured using the NMR estimator, Keck powered magnet operating at 25 Tesla.

The overall goal of this project was to reduce field fluctuations to improve NMR spectroscopy. This can be shown by linewidth and peak frequency shift performance metrics discussed in subsection 6.1.1. The following set of NMR spectroscopy experiments where performed using the Keck powered magnet operating at 25 T. The Tecmag spectrometer, separate from the NMRkitII, was used to acquire 128 consecutive hydrogen nuclei FID signals in response to RF pulses separated by 2 seconds. The 2 second delay allows for the magnetization vector to return to thermal equilibrium in between pulses. The low pass filter cutoff frequency of the receiver was set to 100 kHz and the sample was spun at a frequency greater than 1 kHz. The 128 FID signals were measured for the cases with no compensation, inner loop compensation, and inner and outer loop compensation. The spectra of the consecutive FID signals was computed off-line.

The following set of figures will show the 128 FID magnitude spectra of hydrogen nuclei for each case of control. These spectra should reveal three separate peaks with a central peak due to the Larmor frequency of the hydrogen nuclei. The other two peaks are sideband peaks located on both sides of the hydrogen spectra peak, and result from spinning the sample. These spectra will be used to derive the linewidth and peak frequency shift performance metrics. These metrics can then be evaluated to determine whether the control objectives (5) and (6) where achieved for the cascade feedback control system.

Figure 6.11 shows the consecutive FID spectra with no compensation. The first horizontal axis displays frequency in kHz, and the second horizontal axis displays the index of the 128 FID signals acquired. The vertical axis shows the magnitude of the FID spectra for the 128 FIDs. For the case with no compensation, the field fluctuations present in the Keck powered magnet broadens the linewidth of an individual spectra making it difficult to observe the three spectra peaks. In addition, the peak frequencies of the spectra change by more than 30 kHz over the duration of the experiment. These broad linewidths and peak frequency shifts are undesirable for NMR spectroscopy.

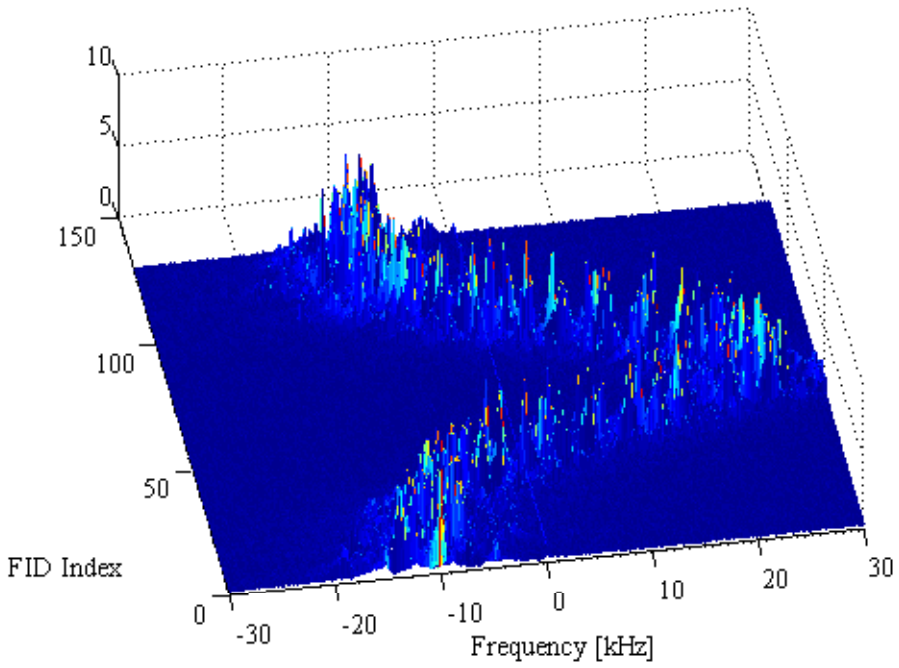

Figure 6.11. FID spectra acquired using Keck powered magnet operating at 25 Tesla with no compensation.

Figure 6.12 shows results for the same NMR experiment with inner loop only compensation. In comparison to Figure 6.11, the FID spectra have sharper peaks illustrating a reduced linewidth. The three spectra peaks are now observed because of the linewidth reduction. In addition, the peak frequencies of the spectra shift by about 25 kHz over the duration of the experiment, which is less than the open-loop case. The inner loop compensation has reduced the higher frequency field fluctuations appreciably, showing significant improvement in the linewidth and moderate improvement in the peak frequency shifts of the FID spectra.

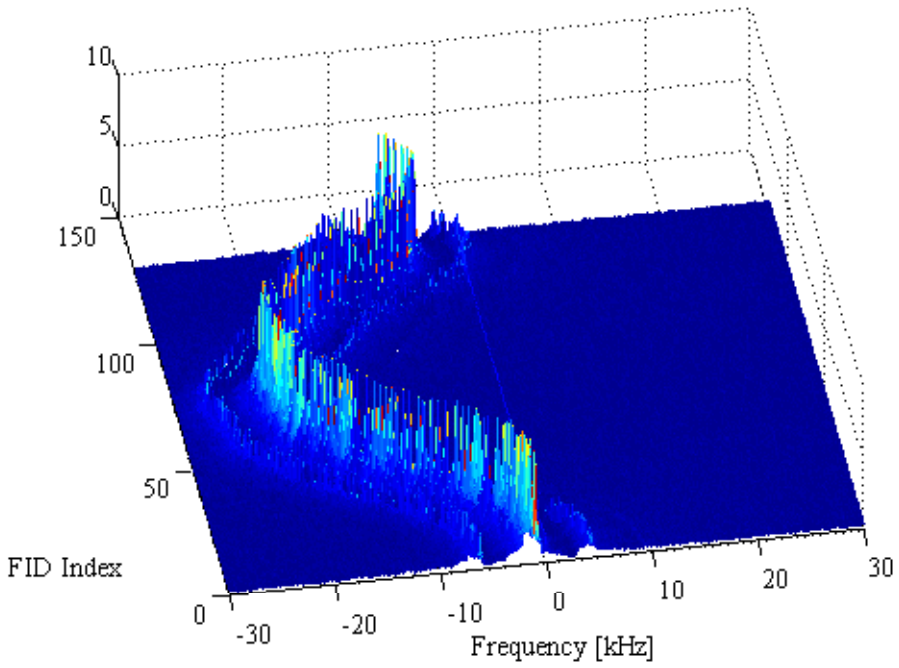

Figure 6.12. FID spectra acquired using Keck powered magnet operating at 25 Tesla with inner loop compensation.

Figure 6.13 shows results for the same NMR experiment with inner and outer loop compensation. In comparison to Figure 6.12, the sharpness of FID spectra peaks remains approximately the same and the three spectra peaks are still visible. This indicates that linewidth is the same when outer loop compensation is added to inner loop compensation. In stark contrast to the previous two cases, the FID spectra are aligned and have no visible shift in peak frequencies. The frequency shift This is two orders of magnitude less than the 25 kHz peak frequency shifts exhibited in Figure 6.12 with inner loop only compensation. The outer loop compensation has reduced the lower frequency fluctuations, providing significant improvement in the peak frequency shifts of the FID spectra.

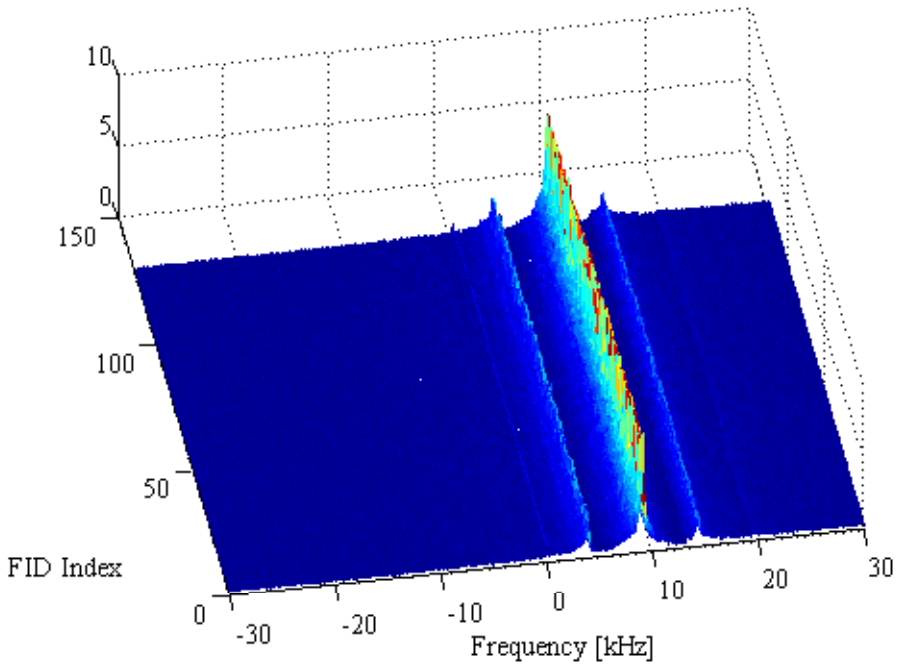

Figure 6.13. FID spectra acquired using Keck powered magnet operating at 25 Tesla with inner and outer loop compensation.

The results in Figures 6.11 thru 6.13 were used to derive the linewidth and peak frequency shift performance metrics of the cascade feedback control system. These performance metrics will be compared for the cases of open loop, inner loop compensation, and inner and outer loop compensation. The linewidth metric is discussed first followed by peak frequency shift.

The second performance metric is the linewidth of FID magnitude spectra discussed in Section 6.1.1. There are three sets of 128 FID magnitude spectra shown in Figures 6.11 thru 6.13. Each set of 128 FID magnitude spectra were aligned in frequency and coherently averaged. This results in three average magnitude spectra, one for each set of 128 FID magnitude spectra. The squared magnitude of each of these three average spectra was then determined. The linewidth was then computed as the frequency bandwidth occurring at the half the maximum peak of the squared average spectra.

Figure 6.14 shows these squared magnitude spectra for the cases on no compensation, inner loop compensation, and inner and outer loop compensation. These spectra are normalized in magnitude for convenience. The case with no compensation is indicated by the solid line while the dashed and dotted lines indicate the cases with inner loop compensation and inner and outer loop compensation.

When there is no compensation, the linewidth is 290 Hz. When inner loop compensation is applied, the linewidth is reduced to 185 Hz. When compared to the inner loop only case, the linewidth for the inner and outer loop compensation remains approximately the same. This is not surprising because higher frequency field fluctuations affect the linewidth. Thus the reduction in lower frequency fluctuations provided by the outer loop does not improve linewidth. The linewidth is reduced from 290 Hz to 185 Hz using the cascade feedback control system, which meets control objective (5). Recommendations for improvements to cascade feedback control system to further reduce linewidth will be discussed in Chapter 7.

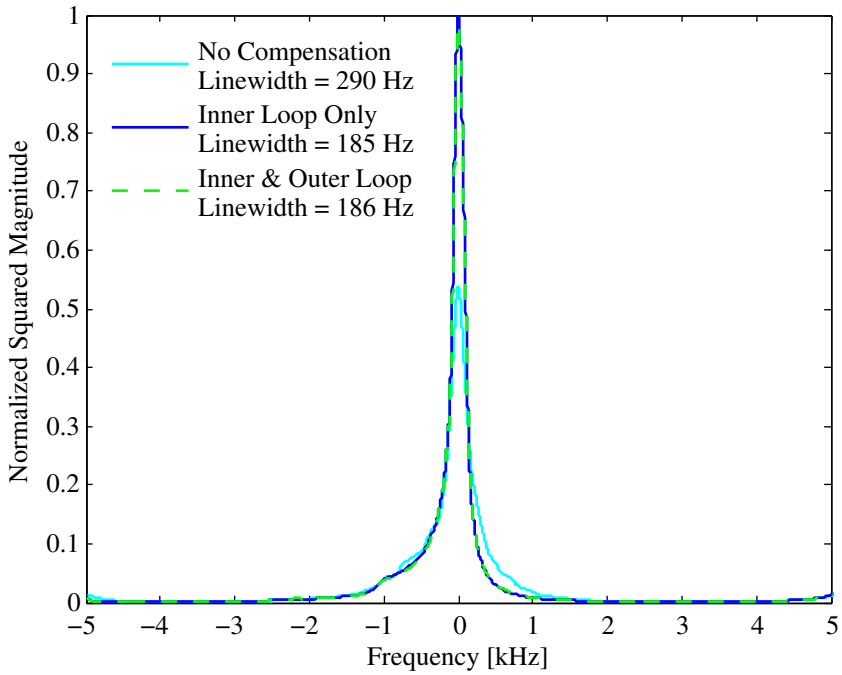

Figure 6.14. Squared magnitude spectra of FID using Keck powered magnet operating at 25 Tesla with no compensation, inner loop compensation, and both inner and outer loop compensation.

The third performance metric is the shift in peak frequencies of consecutive FID magnitude spectra discussed in Section 6.1.1. For a given set of 128 FID magnitude spectra, the frequency at which the peak of the magnitude spectra occurs was determined. This results in 128 peak frequencies for each set of FID magnitude spectra. These peak frequencies where compared for the each case of compensation.

Figure 6.15 shows the FID spectra peak frequencies computed from the FID magnitude spectra. The horizontal axis displays time in seconds, and the vertical axis displays the peak frequency of the FID magnitude spectra in Gauss for each FID. In addition, the legend shows the standard deviation, or rms value, of the peak frequencies for each case of compensation.

When there is no compensation, the peak frequencies change as much more than 9 G (36 ppm) with a standard deviation of 2.96 G. With inner loop compensation, the peak frequencies change by about 5 G (20 ppm) and the standard deviation is 1.64 G. The best performance is shown when the inner and outer loop compensators are engaged. In this case, the peak frequency shifts by less than 0.07 G (0.28 ppm) with a standard deviation of 0.02 G. These results show that control objective (6) is achieved, and are consistent with Figures 6.11 thru 6.13 showing reduction of peak spectra shifts when each control loop is added.

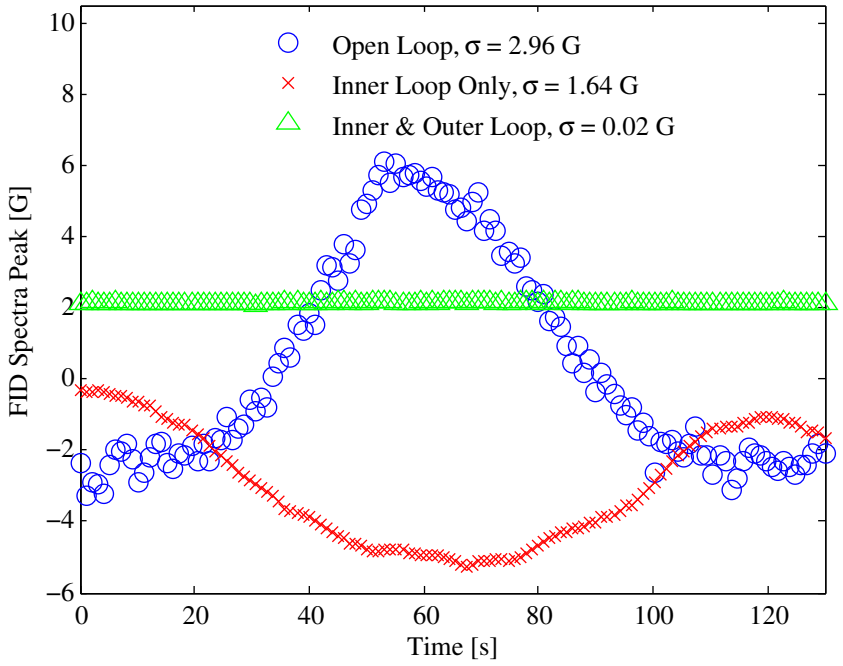

Figure 6.15. Peak frequency shifts of FID spectra acquired using Keck powered magnet operating at 25 Tesla with no compensation, inner loop compensation, and both inner and outer loop compensation.

The experimental results shown in this section demonstrate that the cascade feedback control design has met all the control objectives using the Keck powered magnet. The magnitude of B/B_f was shown to meet control objective (1) thru (4) in simulation in the previous section. Experimental results were consistent with these simulations. Additionally, NMR experimental results showed that the linewidth was reduced from 290 Hz to 185 Hz, which meets the control objective (5). Furthermore, the standard deviation of peak frequency shifts in FID magnitude spectra was shown to be reduced from 2.96 G to 0.02 G, which meets control objective (6).

The less than 0.07 G (0.28 ppm) peak frequency shift with standard deviation 0.02 G corresponds to approximately 298 Hz peak frequency shift with standard deviation 85 Hz. These peak frequency shifts may still be inadequate for some NMR spectroscopy experiments. Improvements can be made to the cascade feedback control system to provide better NMR spectroscopy results.

The results illustrated in this dissertation are discussed and summarized in Chapter 7. Additionally, some suggestions for future work is provided including recommendations for improving the reduction in linewidth and the peak frequency shifts of the FID spectra.

Chapter 7

Discussion and Future Work

7.1 Summary

Large magnetic fields provided by powered magnets can significantly improve NMR spectroscopy. These large fields have the potential to dramatically expand opportunities in the areas of material science, chemistry, and biology. However, powered magnets suffer from temporal field fluctuations of the magnetic field which is undesirable for NMR spectroscopy. Reducing temporal field fluctuations in powered magnets can allow for high field improvements in NMR spectroscopy without the undesirable effects of field fluctuations. The work in this dissertation focused on developing a method for significantly reducing temporal field fluctuations in powered magnets to improve NMR spectroscopy.

Recent studies have shown that field fluctuations resulting from power supple ripple in powered magnets can be significantly reduced with feedback control using inductive measurements. While this method shows improvement in NMR spectroscopy, 1/f noise and lower cutoff frequency limitations of the inductive measurement makes this approach unsuitable for reducing lower frequency fluctuations in powered magnets. Further improvements in NMR spectroscopy using powered magnets can be obtained by using NMR measurements to estimate and reduce

lower frequency fluctuations resulting from variations in cooling water temperature and flow rate. Previous attempts to reduce lower frequency field fluctuations in powered magnets with feedback control using NMR measurements, often referred to as Field-Frequency Locks (FFLs), have not yielded significant reductions in lower frequency fluctuations.

Chapter 4 presented a literature survey of FFLs along with analysis of a dispersion lock design widely used in superconducting magnets. Although dispersion locks are adequate for superconducting magnets, it was shown through experimental results and analysis that dispersion locks have limited ability to reduce lower frequency fluctuations in powered magnets. This is because dispersion locks cannot regulate field fluctuations that change quickly with respect to the NMR time constant T_1. These results will be included in a publication by Samra *et al* [57].

Chapter 5 presented alternative methods for estimating lower frequency fluctuations using NMR measurements. Here the lower frequency fluctuations are directly estimated from NMR measurements, which is better suited for powered magnets than using indirect estimates. Three direct estimation methods were proposed, and their performance was evaluated using experimental data. When comparing these methods, the phase least-squares (LS) fit method provided the smallest error metrics. For this reason, the phase LS fit method was chosen as the NMR estimator for feedback control. An assessment of the NMR estimator in terms of the pulse sequence, FID signal measurement, and aliasing was then provided in this chapter. It was shown that higher frequency fluctuations alias into the NMR estimator bandwidth, and that an inductive feedback control design provides anti-aliasing as it reduces higher frequency fluctuations.

Chapter 6 presents a cascade feedback control system which simultaneously reduces lower and higher frequency field fluctuations. The higher frequency fluctuations are estimated from inductive measurements and reduced using an inner loop compensator. The lower frequency fluctuations are estimated from NMR measurements using the NMR estimator from Chapter 5. These estimates of lower frequency fluctuations are then reduced using an outer loop compensator. The cascade combination of the inner and outer loops form a cascade feedback control system.

The reduction of field fluctuations in the Keck powered magnet provided by the cascade feedback control system is shown experimentally using the performance metrics introduced in Chapter 1. The linewidth of the FID magnitude spectra was reduced from 290 Hz to 185 Hz and the standard deviation of peak frequency shifts was reduced from 2.96 G to 0.02 G, or equivalently from 12.6 kHz to 85 Hz.

In summary, the work shown in this dissertation:

- Demonstrated that dispersion locks are limited in powered magnets because they use indirect measurements of fluctuations [57].
- Developed a NMR estimator using a direct estimation method to overcome the limitations of dispersion locks in powered magnets [62].
- Demonstrated NMR estimator aliasing of higher frequency fluctuations and anti-aliasing provided by inductive feedback control [62].
- Designed, synthesized, and verified a cascade feedback control system to simultaneously reduce lower and higher frequency fluctuations in powered magnets [62].

7.2 Recommendations for Future Work

While the work presented in this dissertation shows significant improvement in NMR spectroscopy, the 185 Hz linewidth and 85 Hz standard deviation of FID spectra peak shifts are still inadequate for some NMR spectroscopy experiments. It is desirable to reduce the 185 Hz linewidth to less than 100 Hz and the 85 Hz standard deviation by another order of magnitude so that it is less than 10 Hz. In this section, the limitations of the cascade feedback control system are discussed along with some recommendations for future work to overcome these limitations. These improvements in the cascade feedback control system may provide the less than 10 Hz peak shifts in FID spectra desirable for some NMR experiments.

The first limitation of the cascade feedback control system arises from using dSPACE digital signal processors to provide real–time implementation of the NMR estimator, inner loop compensator, and outer loop compensator. A single dSPACE controller board lacks the computational capacity to perform all these functions, which made it necessary to use two dSPACE boards. An effort is currently underway to replace the multiple dSPACE controller boards with a stand-alone embedded micro-controller system equipped with a field programmable gate array (FPGA), which have significantly more computational capability than the dSPACE boards. Using this system, the NMR estimator and both loops of the cascade feedback control system can be implemented with a single FPGA, providing time coherence of all real–time operations of the cascade feedback control system.

Another limitation of the cascade feedback control system is the high frequency gain of the transfer function $H(s)$ representing the integrating preamplifier in series with the pickup coil. For frequencies much greater than the time constant, the gain of $H(s)$ is constant. This gain is approximately -27 dB, implying that the voltage at the integrating preamplifier output is 27 dB less than the field fluctuation at the pickup coil. The minimum voltage that can be sensed by the inner loop compensator is determined by the 16 bit ADC of the dSPACE, and is fixed at 0.3 mV. Attenuating the pickup coil field by 27 dB reduces the dynamic range of field fluctuations that can be sensed by the inner loop. It is preferable to have a larger high frequency gain of $H(s)$ to provide large dynamic range for the inner loop compensator. Research work is currently underway to modify the integrating preamplifier electrical components to provide more high frequency gain of this transfer function.

An additional limitation to the cascade feedback control system is the that the correction field is limited to 7 Gauss as mentioned in Section 2.2. This implies that the cascade feedback control system cannot regulate field fluctuations close to zero if the field fluctuations change by much more than 7 Gauss. It is recommended to use a current amplifier that can drive larger currents to the correction coil in order to achieve a larger correction field for the compensators.

Research is currently underway to replace the current amplifier with another current amplifier that has more current driving capability.

The limitations discussed up to this point arise from hardware used to implement the cascade feedback control system. In addition to improving the hardware of the cascade feedback control system, there are design modifications that may significantly improve the performance and applications of the cascade feedback control system.

The first design modification is to implement the cascade feedback control system in the presence of field gradients. Certain NMR experiments such as gradient enhanced spectroscopy and two-dimensional NMR are improved in the presence of field gradients. Additionally, magnetic resonance imaging (MRI) experiments require field gradients. Up to this point, these experiments have been limited on powered magnets due to field fluctuations. If the cascade feedback control system was designed to reduce field fluctuations in the presence of field gradients, then these experiments can take advantage of the high field strengths afforded by powered magnets without being limited by field fluctuations.

The second design modification is to improve the NMR estimator. Recall from Section 5.3 that the most significant factor limiting the NMR estimator was signal-to-noise (SNR) ratio of the measured FID signals, and if the SNR was close to 70 V/V then NMR estimator was accurate within 20 Hz or 31 mG. Modifications to the NMR estimator, for example increasing the acquisition time of the FID signals, could improve the 20 Hz performance limit of the NMR estimator. Also recall from Section 5.3 that the FID sample frequency was set to 25 kHz due to computational limitations. If this sample frequency was increased, then the bandwidth and hence baseband frequency of the FID signal can be increased. This allows estimation of larger shifts in FID frequency and consequently larger changes in field. The net result is larger changes in field can be estimated and reduced when the FID sample frequency is increased. The improvements in hardware will allow for a much larger FID sample frequency than 25 kHz.

The third design modification is to implement cascade feedback control with field shimming. The results shown in this dissertation were obtained with no field shimming. Recall from Section 1.1 that field shimming significantly improves spatial field homogeneity, which will improve NMR spectroscopy. Thus it is expected that linewidth of the FID magnitude spectra and standard deviation of the peak frequency shifts will be improved if cascade feedback control is implemented with field shimming. The results obtained from implementing the cascade feedback control system with field shimming will be published [62].

Lastly, the temporal field fluctuations can also be mitigated by improving the feedback control systems that regulate power supply ripple and cooling water temperature variations. Recall from Section 1.2 that 60 Hz harmonics of the power supply ripple are likely introduced by the feedback loop consisting of an active filter, holec current transformer, and digital controller. It may be possible to redesign this feedback loop so that 60 Hz harmonics are reduced in the power supply ripple. Additionally, it may be possible to improve the feedback control system which regulates cooling water temperature variations. By improving these designs the temporal field fluctuations can be eliminated at the source, which may be preferable to the active feedback control system presented in this dissertation.

Bibliography

[1] Committee to assess the current status and future direction of high magnetic field science in the United States, High magnetic field science and its application in the United States: current status and future directions, National Academy of Sciences, 2013.

[2] B. Shapira, K. K. Shetty, W. W. Brey, Z. H. Gan, and L. Frydman. Single-scan 2D NMR spectroscopy on a 25 T Bitter magnet. *Chem. Phys. Lett.*, 446(4–6):478–482, July 2007.

[3] F. Bloch. Nuclear induction. *Physical Review*, 70(7–8):460–474, October 1946.

[4] E. M. Purcell, H. C. Torrey, and R. V. Pound. Resonance absorption by nuclear magnetic moments in a solid. *Physical Review*, 69(1–2):37, January 1946.

[5] R. Gruetter, S. A. Weisdorf, V. Rajanayagan, M. Terpstra, H. Merkle, C. L. Truwit, M. Garwood, S. L. Nyberg, and K. Ugurbil. Resolution improvements in in vivo ^{1}H NMR spectra with increased magnetic field strength. *Journal of Magnetic Resonance*, 135(1):260–264, November 1998.

[6] D. I. Hoult and R. E. Richards. The signal-to-noise ratio of the nuclear magnetic resonance experiment. *Journal of Magnetic Resonance*, 24(1):71–85, October 1976.

[7] Z. Gan, P. L. Gorkov, T. A. Cross, A. Samoson, and D. Massiot. Seeking higher resolution and sensitivity for NMR of quadrupolar nuclei at ultrahigh magnetic fields. *J. Am. Chem. Soc.*, 124(20):5634–5635, February 2002.

[8] K. Pervushin, R. Riek, G. Wider, and K. Wthrich. Attenuated T2 relaxation by mutual cancellation of dipole-dipole coupling and chemical shift anisotropy indicates an avenue to NMR structures of very large biological macromolecules in solution. *Proc Natl Acad Sci U S A.*, 94(23):12366–12371, November 1997.

[9] Y. Y. Lin, S. Ahn, N. Murali, W. W. Brey, C. R. Bowers, and W. S. Warren. High-resolution, $>$ 1 GHz NMR in unstable magnetic fields. *Phys. Rev. Lett.*, 85(17):3732–3735, October 2000.

[10] L. Peng, Z. Y. Zheng, Y. Q. Huang, Z. M. Zhang, S. H. Cai, and Z. Chen. High-resolution NMR spectra in inhomogeneous and unstable fields via the three-pulse method. *Mol. Phys.*, 108(14):1869–1875, July 2010.

[11] J. H. Cho, S. Ahn, C. Lee, K. S. Hong, K. C. Chung, S. K. Chang, C. Cheong, W. S. Warren Magnetic resonance microscopic imaging based on high-order intermolecular multiplequantum coherences. *Magn. Reson. Imag.*, 25(5):626–633, June 2007.

[12] J. Bascuñán, W. Kim, S. Hahn, E. S. Bobrov, H. Lee, and Y. Iwasa. An LTS/HTS magnet operated in the range of 600-700 MHz. *IEEE Trans. Appl. Supercond.*, 17(2):1446–1449, June 2007.

[13] Y. Yanagisawa, H. Nakagome, K. Tennmei, M. Hamada, M. Yoshikawa, A. Otsuka, M. Hosono, T. Kiyoshi, M. Takahashi, T. Yamazaki, and H. Maeda. Operation of a 500 MHz high temperature superconducting NMR, Towards an NMR spectrometer operating beyond 1 GHz. *Journal of Magnetic Resonance*, 203:274–282, January 2010.

[14] S. Matsumoto, T. Kiyoshi, A. Otsuka, M. Hamada, H. Maeda, Y. Yanagisawa, H. Nakagome, and H. Suematsu. Generation of 24 T at 4.2 K using a layer-wound GdBCO insert coil with Nb_3Sn and Nb-Ti external magnetic field coils. *Superconductor Science Technology*, 25(2):1–5, January 2012.

[15] J. R. Miller. The NHMFL 45-T hybrid magnet system: Past, present, and future. *IEEE Trans. Appl. Supercond.*, 13(2):1385–1390, June 2003.

[16] M. D. Bird and Z. Gan. Low resolution NMR magnets in the 23 to 35 T range at the NHMFL. *IEEE Trans. Appl. Supercond.*, 12(1):447–451, March 2002.

[17] H. D. W Hill, R. E. Richards. Limits of measurement in magnetic resonance. *J. Phys. E: Sci. Instrum.*, 2(1) 977–983, February 1968

[18] E. E. Sigmund, E. S. Calder, G. W. Thomas, V. F. Mitrovic, H. N. Bachman, W. P. Halperin, P.L. Kuhns, and A. P. Reyes. NMR phase noise in bitter magnets. *Journal of Magnetic Resonance*, 148(2):309–313, February 2001.

[19] M. J. E. Golay. Field homogenizing coils for nuclear spin resonance instrumentation. *Rev. Sci. Instrum.*, 29(4):313–315, April 1958.

[20] G. N. Chmurny and D. I. Hoult. The ancient and honourable art of shimming. *Consepts in Magnetic Resonance*, 2(3): 131-149, July 1990.

[21] P. J. M. van Bentum, J. C. Maan, J. W. M. van Os, and A. P. M. Kentgens. Strategies for solid-state NMR in high-field bitter and hybrid magnets. *Chem. Phys. Lett.*, 376(3–4):338-345, July 2003.

[22] M. D. Bird, S. Bole, Y. M. Eyssa, and Z. H. Gan. Progress towards 1 ppm at 25 T. *IEEE Trans. Appl. Supercon.*, 10(1):443-446, March 2000.

[23] F. Bloch. Line-Narrowing by Macroscopic Motion. *Physical Review*, 94(2): 496-497, April 1954.

[24] J. T. Arnold. Magnetic resonances of protons in ethyl alcohol. *Physical Review*, 102(1): 136-152, April 1956.

[25] H. J. Boenig, F. Bogdan, G. C. Morris, J. A. Ferner, H. J. Schneider-Muntau, R. H. Rumrill, and R. S. Rumrill. Design and preliminary test results of the 40-MW power supply at the national high magnetic field laboratory. *IEEE Transactions on Magnetics*, 30(4):1774-1777, July 1994.

[26] H. J. Boenig, J. A. Ferner, F. Bogdan, R. S. Rumrill, and G. C. Morris. Design and operation of a 40-MW, highly stabilized power supply. *IEEE Transactions on Industry Applications*, 32(5):1146-1157, September 1996.

[27] M. Li. Reduction of temporal magnetic field fluctuations in high field resistive magnets using digital feedback control. Master's thesis, The Pennsylvania State University, August 2007.

[28] M. Li, J. L. Schiano, J. E. Samra, K. K. Shetty, and W. W. Brey. Reduction of magnetic field fluctuations in powered magnets for NMR using inductive measurements and sampled-data feedback control. *Journal of Magnetic Resonance*, 212(2):254–264, October 2011.

[29] J. Samra. A field-frequency lock implemented with a sampled-data feedback control algorithm derived from a small-signal NMR model. Master's thesis, The Pennsylvania State University, December 2008.

[30] H. J. Schneider-Muntau, J. Toth, and H. W.Weijers. Generation of the highest continuous magnetic fields. *IEEE Transactions on Applied Superconductivity*, 14(2):1245-1252, June 2004.

[31] V. Soghomonian, M. Sabo, A. Powell, P. Murphy, R. Rosanske, T. A. Cross, and H. J. Schneider-Muntau. Identification and minimization of sources of temporal instabilities in high field (>23 T) resistive magnets. *Review of Scientific Instruments*, 71(7):2882–2889, July 2000.

[32] E. S. Meyer, I. F. Silvera, and B. L. Brandt. Eddy current shielding and heating: reduction of dissipation for very low-temperature experiments in the presence of magnetic field ripple. *Review of Scientific Instruments*, 60(9):2964–2968, September 1989.

[33] E. E. Sigmund, V. F. Mitrovic, E. S. Calder, G. W. Thomas, H. N. Bachman, W. P. Halperin, P. L. Kuhns, and A. P. Reyes. Inductive shielding of NMR phase noise. *Journal of Magnetic Resonance*, 159(2):190–194, December 2002.

[34] A. Otsuka, T. Kiyoshi, and S. Matsumoto. HTS magnetic field damper for short-term fluctuations in the driven-mode. *IEEE Transactions on Applied Superconductivity*, 18(2):848–851, June 2008.

[35] G. A. Morris, H. Barjat, and T. J. Horne. Reference deconvolution methods. *Prog. Nucl. Magn. Reson. Spectrosc.*, 31:197–257 September 1997.

[36] T. Iijima, K. Takegoshi, K. Hashi, T. Fujito, and T. Shimizu. High-resolution NMR with resistive and hybrid magnets: Deconvolution using a field-fluctuation signal. *Journal of Magnetic Resonance*, 184(1):258-262, January 2007.

[37] T. Iijima and K. Takegoshi. Compensation of effect of field instability by reference deconvolution with phase reconstruction. *Journal of Magnetic Resonance*, 191(1):128-134, January 2008.

[38] Z. Gan, H. T. Kwak, M. D. Bird, T. A. Cross, P. L. Gorkov, W. W. Brey, and K. K. Shetty. High-field NMR using resistive and hybrid magnets. *Journal of Magnetic Resonance*, 191(1):135–140, January 2008.

[39] P. Pelupessy, E. Rennella, G. Bodenhausen. High-resolution NMR in magnetic fields with unknown spatiotemporal variations. *Science*, 324(5935):1693–1697, June 2009.

[40] O. Pauvert, F. Fayon, A. Rakhmatullin, S. Kramer, M. Horvati, D. Avignant, C. Berthier, M. Deschamps, D. Massiot, and C. Bessada. ^{91}Zr Nuclear magnetic resonance spectroscopy of solid zirconium halides at high magnetic field. *Inorganic Chemistry*, 48(18):8709-8717, August 2009.

[41] D. Laurencin, C. Gervais, H. Stork, S. Kramer, D. Massiot, and F. Fayon. ^{25}Mg solid-state NMR of magnesium phosphates: high magnetic field experiments and density functional theory calculations. *Journal of Physical Chemistry*, 116:19984–19995, August 2012.

[42] H. Primas and H. H. Gunthard. Field stabilizer for high-resolution nuclear magnetic resonance. *Review of Scientific Instruments*, 28(7):510–514, July 1957.

[43] H. H. Gunthard. and J. J. Primas. Magnetic field stabilizer. *U.S. Patent 2,979,641*, April 11, 1961.

[44] A. M. Gottlieb, V. C. Srivastava, P. Heller, and L. G. Rubin. A tunable NMR spectrometer for the vhf-uhf range. *Review of Scientific Instruments*, 43(4):676–680, April 1972.

[45] M. E. Packard. A proton controlled magnetic field regulator. *The Review of Scientific Instruments*, 19(7):435–439, July 1948.

[46] E. B. Baker and L. W. Burd. High stability nuclear magnetic resonance spectrograph. *The Review of Scientific Instruments*, 28(5):313–321, May 1957.

[47] E. Grunwald, C. F. Jumper, and A. Meiboom. Kinetics of proton transfer in methanol and the mechanism of the abnormal conductance of the hydrogen ion. *J. Am. Chem. Soc.*, 84(24):4664–4671, December 1962.

[48] W. A. Anderson. Applications of modulation techniques to high resolution nuclear magnetic resonance spectrometers. *The Review of Scientific Instruments*, 33(11):1160–1166, November 1962.

[49] J. T. Arnold. *Private Communication*, 1955.

[50] K. J. Packer and A. J. Strike. A simple method for maintaining the resonance condition in a spin echo nuclear magnetic resonance spectrometer. *Journal of Magnetic Resonance*, 2(1):79–87, January 1970.

[51] D. I. Hoult, R. E. Richards, and P. Styles. A novel field-frequency lock for a superconducting spectrometer. *Journal of Magnetic Resonance*, 30(2):351–365, May 1978.

[52] S. Kan, P. Gonord, M. Fan, M. Sauzade, and J. Courtieu. Automatic NMR field-frequency lock - pulsed phase locked loop approach. *The Review of Scientific Instruments*, 49(6):785–789, June 1978.

[53] H. D. W. Hill. Automatic field-frequency lock in an NMR spectrometer. *U.S. Patent 4,171,511*, October 16, 1979.

[54] R. M. Hawk, R. R. Sharp, and J. W. Tolan. A broadband NMR spectrometer for field stabilization in the range 4-23 kG. *Review of Sciientific Instruments*, 45(2):96–99, August 1974.

[55] E. K. Paulson and K. W. Zilma. External field-frequency lock probe for high resolution solid state. *Review of Sciientific Instruments*, 76(2):026104-1–026104-3, January 2005.

[56] M. Schenkel, R. Hensel, W. Tschopp. Device and method for compensation of magnetic field disruptions in highly homogeneous magnetic fields. *US Patent 7,474,976*, January 6, 2009.

[57] J. E. Samra, J. L. Schiano, B. F. Thomson, K. K. Shetty, and W. W. Brey. A field-frequency lock implemented with a sampled-data control algorithm derived from a small-signal NMR model. *Journal of Magnetic Resonance*, to be submitted Fall 2013.

[58] D. C. Hofer, V. N. Kahwaty, and C. R. Valentino. NMR field frequency lock system. *U.S. Patent 4,110,681*, August 29, 1978.

[59] M. Takahashi, Y. Ebisawa, K. Tennmei, Y. Yanagisawa, M. Hosono, K. Takasugi, T. Hase, T. Miyazaki, T. Fujito, H. Nakagome, T. Kiyoshi, T. Yamazaki, and H. Maeda. Towards a beyond 1 GHz solid-state nuclear magnetic resonance: External lock operation in an external current mode for a 500 MHz nuclear magnetic resonance. *The Review of Scientific Instruments*, 83(105110):1–6, October 2012.

[60] O. Schett and A. Schwilch. Method and device for compensating of field disturbances in magnetic fields. *US Patent 5,302,899*, April 12, 1994.

[61] M. Park and H. Habara. Stabilizer for stabilizing NMR magnetic field and method of the same. *US Patent 7,167,002*, January 23, 2007.

[62] B. F. Thomson, J. L. Schiano, B. D. McPheron, K. K. Shetty, and W. W. Brey. Estimation and reduction of temporal field fluctuations in powered magnets using inductive and NMR feedback control. *Journal of Magnetic Resonance*, to be submitted Fall 2013.

[63] B. D. McPheron, J. L. Schiano, B. F. Thomson, K. K. Shetty, W. W. Brey, I. Hung, and Z. Gan. Demonstration of 2D NMR spectroscopy in a powered magnet at 25T. *Journal of Magnetic Resonance*, to be submitted Fall 2013.

[64] E. C. Levy. Complex-curve fitting. *IRE Transactions on Automatic Control*, 4(1):37-44, May 1959.

[65] C. P. Slichter. Principles of magnetic resonance. Springer, 1996.

[66] A. Abragam. *The Principles of Nuclear Magnetism.* Oxford University Press, Inc., 1961.

[67] J. L. Schiano, R. L. Magin, and S. M. Wright. Feedback control of the nuclear magnetization state: Modeling and control design. *IEEE Transactions on Medical Imaging*, 10(2):138–147, June 1991.

[68] J. G. Proakis and M. Salehi. *Fundamentals of Communication Systems.* Prentice Hall, Saddle River, NJ, 2005.

[69] *Understanding Frequency Counter Specifications.* Agilent Technologies, Application Note 200-4, May 1997.

[70] L. Ljung. *System Identification.* Prentice Hall, Saddle River, NJ, Second edition, 1999.

[71] D. P. Glasson. Development and applications of multirate digital control. *IEEE Control Systems Magazine*, 28(5):13–15, November 1983.

Vita

Brian F. Thomson

Brian Thomson was born in Pittsburgh, Pennsylvania on September 24, 1982 and grew up in West Deptford, New Jersey. He received a B.S. degree with honors in Electrical Engineering from Rochester Institute of Technology in May 2006. He was employed with Lockheed Martin from 2006 to 2007 as an associate member of the engineering staff. In 2007, Brian enrolled in the M.S. program in Electrical Engineering at the Pennsylvania State University in University Park, Pennsylvania. Under advisement from Dr. Benjamin Thompson, Brian received his M.S. degree in July 2009. Upon completion of his M.S. degree, he enrolled in the Ph.D. program in Electrical Engineering at the Pennsylvania State University in August 2009. With the advisement of Dr. Jeffrey Schiano, Brian completed his Ph.D. degree in November 2013. His research interests include feedback control, signal processing, autonomous vehicles, and magnetic resonance.